Field Disruption Energy Harvester Design and Modeling: A Novel Approach in Electromagnetic Vibration Energy Harvesting

by

Karim El-Rayes

A thesis
presented to the University of Waterloo
in fulfillment of the
thesis requirement for the degree of
Doctor of Philosophy
in
Mechanical and Mechatronics Engineering

Waterloo, Ontario, Canada, 2023

Author's Declaration

I hereby declare that I am the sole author of this thesis. This is a true copy of the thesis, including any required final revisions, as accepted by my examiners.

I understand that my thesis may be made electronically available to the public.

ABSTRACT

The demand for sustainable and non-traditional sources of energy increases every day to power up different electronic equipment whether it's portable low-power devices, non-accessible sensors, wearable electronics, implantable medical devices, and even for big scale applications that can contribute to the energy demand on a public level [1]. Energy harvesting from vibrations offers an ideal source of energy, since it's renewable and prevailing, where kinetic energy that can be harvested is abundant in nature.

In this proposal, a novel electromagnetic transduction mechanism is introduced that can be used in harvesting low-frequency vibrations below $10Hz$, which makes it suitable to harvest motion from human locomotion, moving vehicles, and structures like buildings, bridges and streets. The transduction mechanism developed induces a current in a coil by disrupting the electromagnetic field in the vicinity of a stationary coil wound around a hollow track (tube) made of non-conducting or conducting (copper) material, where a ball made of ferromagnetic material is moving freely along the track cutting the field lines and induces current in the coil.

Prototypes embodying the harvesting mechanism were fabricated and tested to identify the different system parameters, frequency-responses and characterize the harvester in order to derive a representative mathematical model. The performance of the energy harvester was measured and characterized in terms of output power, power density and tunability. Where the prototypes fabricated demonstrated a capability to harvest energy at low-frequencies in the range of 6.54-12.72Hz, with a $3dB$ harvesting bandwidth ranging between $1.32Hz$ to $5.8Hz$, and generated output power up to $154\mu W$.

The proposed transduction mechanism demonstrated a strong flexibility that allows tuning the center frequency magnetically, without the need to modify the mechanical design, in order to take advantage of this feature, an intelligent fuzzy tuner design is proposed, supported with simulation results that show the potential of adaptive control of center frequency to increase the generated output power.

This abstract proposes a future plan for the development of the intelligent fuzzy tuner hardware and it's validation to increase the generated output power and power density at low frequencies while reducing the need for any external interference in the harvester's operation, leading the way for a new generation of adaptive vibrations-based energy harvesters.

Acknowledgements

I would like to express my heartfelt gratitude to my graduate supervisor, Professor William Melek, for his unwavering support, invaluable guidance, and mentorship throughout my Ph.D. journey. His expertise and encouragement have been instrumental in shaping my research and academic growth.

I am also deeply thankful to my collaborator, Dr. Salam Gabran, for his valuable insights, collaboration, and contributions to my research. Our partnership has enriched my work and expanded my horizons in the field.

I extend my sincere appreciation to my colleagues and supervisors at the University of Washington for their support, camaraderie, and the stimulating academic environment they provided. Their input and encouragement have been pivotal in my academic success.

Lastly, I am grateful to my family and friends for their unwavering support and understanding throughout this challenging but rewarding journey.

Dedication

To my lovely small family Dad....It would not have been possible without you.
To my mentors, thank you for the best gift you can give to a mentee: Hope.

Table of Contents

List of Figures

ix

List of Tables

Chapter 1

Introduction

1.1 Motivation

In the age of digital revolution, electronics play a major role in improving people's lives everyday, wearables, wireless sensors, medical implants, bionics and many other inventions have shaped the world we live in, the increasing spread of these modern technologies built the strong demand for sustainable, uninterpretable and environmental friendly source of power to maintain a continuous operation of any electronic device, especially the ones used in safety-critical applications. Vibrations energy harvesting, shortly VEH, provides the means of sustainability for a power source from the scavenging waste kinetic energy in mechanical vibrations and motion from the surrounding environment and converting it to usable electric power.

Modern electronic systems that require mobility or installed in remote locations rely heavily on energy storage elements like batteries or super capacitors as a source of power, which limits the operational life-time of the equipment to the life time of the energy storage element capacity, which in many cases is extremely limited to few hours of operation. In this dissertation different approaches are proposed to extend electronic systems operational lifetime by recharging the energy storage element by harvesting kinetic energy from vibrations. Example of systems that can benefit from vibrations energy harvesting are, but not limited to, cellphones, wireless sensors, medical pacemakers, emergency lights, visual & wireless beacons, wearables, smart watches and many other technologies that can benefit from the proposed concepts. Next section will highlight in details the technical shortcomings in the current technology and address the main challenges.
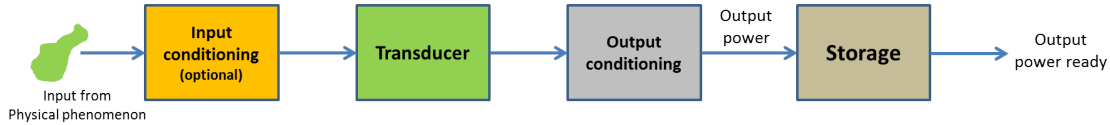
Figure 1.1: Phases of energy harvesting

1.2   Problem Statement

Vibrations energy harvesting goal is to extend the operational life-time of any electronic system by providing a sustainable source of electric power to charge the energy storage element in use, however VEH faces few challenges that reduces the efficiency and the amount of generated power: harvesting at very low frequencies (below 20 Hz), where it requires a mechanical oscillator with relatively large proof-mass and a bulky form-factor in order to harvest efficiently, inflexible tunability of the center frequency, which requires modifying the mechanical design, and intermittent vibrations in the operating environment.

In this dissertation a novel electromagnetic transduction mechanism associated with a simple mechanical oscillator design and an intelligent center frequency tuner are proposed. The new mechanism is capable of harvesting kinetic energy at low frequency, low amplitude vibrations below 10 Hz and 1g, respectively, which resolves all of the mentioned challenges in VEH, while maintaining a small form-factor and provides a non-mechanical flexible tuning mechanism to adjust the VEH center frequency to the frequencies existing in the operating environment.

1.2.1   Energy Harvesting

Energy Harvesting is the process of scavenging energy from a physical phenomenon in nature such as kinetic, solar, thermal...etc, and converting it to usable electrical energy. Surprisingly, energy harvesting is as old as the discovery of electricity, early discoveries of thermal and solar energy harvesting go back to the early 1800's, figure 1.2 shows a historical timeline of discoveries in the field of energy conversion, and energy harvesting in specific.

Since energy is neither created nor destroyed, captured energy is either transformed to electrical energy or lost to various energy loss mechanisms, depending on the harvester design and the harvesting mechanism. The level of complexity of energy harvesting varies depends on five factors:

- The form of energy to be harvested and the amount of energy available in the environment.

- The technology used in harvesting and conversion as far as its reliability and suitability to the amount of energy being harvested, and efficiency.

- The type and design of the transducer.
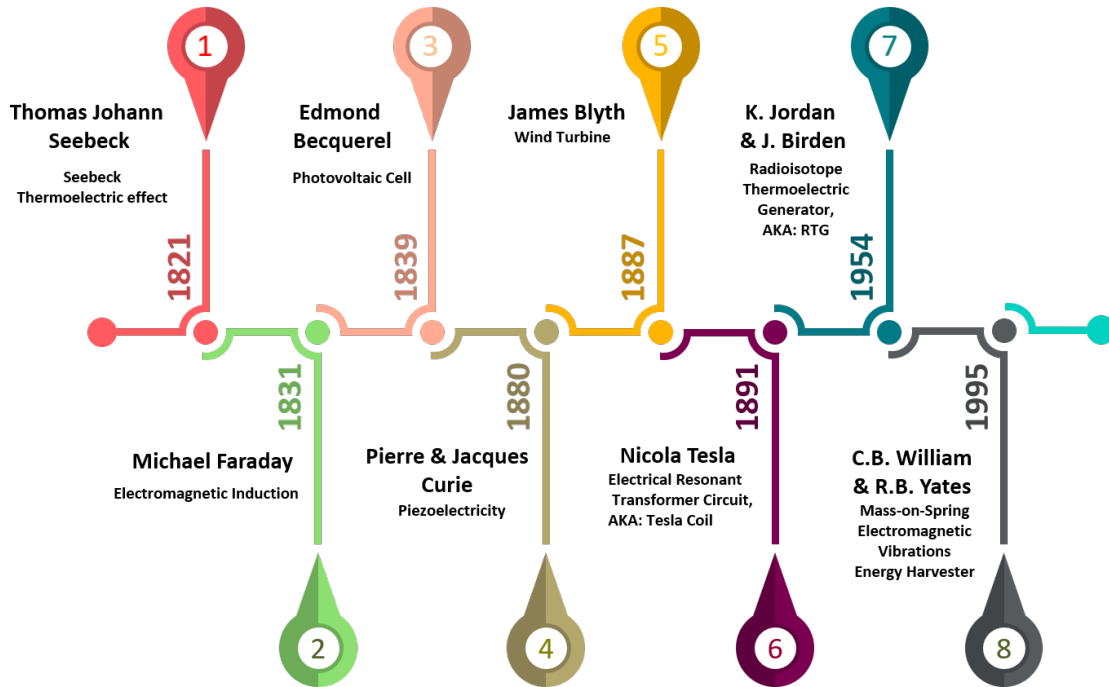
Figure 1.2: Historical timeline of energy harvesting

- The need for input or output conditioning blocks, such as filters, rectifiers, boosting circuits, and regulators.

- The type of energy storage element, since the output energy is not consumed in tandem with the conversion process.

Figure 1.1 summarizes the energy harvesting process phases and the importance of each phase.

1.2.2 Scales of energy harvesting

It is common to find energy harvesters used in daily life applications, some can convert and output relatively large amounts of electric power that supports the power grid like solar panels and wind farms, which they output up to hundreds of kilowatts to few gigawatts of electric power. On the other hand, small electronic devices require lower amounts of energy to operate, and some of these applications require a perpetual or sustainable source of energy depending on the operating conditions and tasks criticality, early examples of these devices are kinetic wrest watches and solar panel-powered calculators. Therefore, two categories of energy harvesters can be identified in terms of the level of output power:

- Macro energy harvesting: generates high levels of electrical power on the order of a few hundreds of watts or more, that can feed the electrical grid like solar power stations or wind farms. At this scale, energy harvesting units require mechanical and electrical component design, maintenance, and transmission lines and occupy large space.

- Micro energy harvesting: generates low levels of power (microwatts up to few watts). This category of harvesters is suitable to drive low power portable electronic devices, and applications that require a perpetual source of energy like RFID modules or wireless sensor networks, and sensors in hard to access places, where it is not feasible or practical to change batteries on a regular basis or to extend a power cable to them. This scale of energy harvesters has many advantages in terms of mechanical and electrical components' design simplicity, setup, maintenance, footprint, and size, integration with other systems and cost. On the other hand, the disadvantages of this category of energy harvesters are:

  - Intermittent output: since it harvests energy from the environment, the availability of output power depends on how frequent is the physical phenomenon being harvested.

  - Unregulated output: due to unpredictability of the output energy magnitude and frequency.

  - Very low output power: output power is low not just because the amount of energy being harvested is small, like that in human body motion or variation in air temperature, but also because of power losses in mechanical components and signal conditioning circuits.

Since micro-energy harvesters are used to scavenge micro-energy from a physical phenomenon, such as thermal, light, motion...etc, they should be highly sensitive and highly efficient by reducing losses.

Low-frequency vibrations, which occur below 10 Hz, are plentiful in nature and serve as a significant source of kinetic energy, as illustrated by the examples listed in the table 1.1. However, extracting kinetic energy from these low-frequency vibrations necessitates a considerably large proof-mass. Additionally, as the frequency approaches zero, the harvesting bandwidth diminishes. These factors pose challenges to the process of harvesting energy from low-frequency vibrations. The transduction mechanism proposed in this dissertation introduces a technique that enables efficient energy harvesting from low-frequency vibrations, utilizing a straightforward, robust, and scalable design.

Table 1.1: Frequency range for different sources of vibration

Source of vibration	Frequency (Hz)
Walking [42]	0.6-2.5
Ground vibration (man-made) [39]	1-200
Human motion [41]	0.6-5
Vehicles bouncing [40]	1-10

1.3 Contributions

In this thesis, a novel energy harvesting technique from environmental vibrations using a mechanical oscillator coupled with electromagnetic transduction mechanism is presented. Towards this goal, different methods and prototypical designs that enable the realization of energy harvesters capable of harvesting low-frequency vibrations prevalent in human & vehicles motion and built environments are developed and analyzed. The energy harvester design presented in this dissertation demonstrated encouraging outcomes in capturing low-frequency vibrations below 10 Hz. It achieved this by utilizing a small moving proof-mass, enabling it to harness vibrations from both artificial and natural sources as mentioned in table 1.1. Additionally, the design can be adjusted to harvest energy at multiple resonance frequencies through mechanical, electronic, and magnetic methods. This expands the range of vibrations that can be captured and provides greater flexibility for the user. The presented energy harvester design introduces a unique architecture that deviates from the conventional approach of using either a moving permanent magnet with a stationary coil or vice versa. Instead, it employs a stationary coil and magnet in conjunction with a moving proof-mass composed of a ferromagnetic material, which serves as the transduction mechanism. This innovative architecture minimizes the reliance on moving mechanical components, particularly permanent magnets that are prone to brittleness. As a result, it reduces potential points of failure and enhances the durability of the harvester, ensuring consistent operation across a wide range of environments.

The presented electromagnetic energy harvester is dubbed the "field disruption energy harvester", or shortly FDH. The electromagnetic transduction method presented here disrupts the magnetic field by crossing a stationary structure of a coil and magnets with a ferromagnetic object. Further through the dissertation, the following contributions are introduced:

- The electromechanical design of the field disruption energy harvester and novel electromagnetic transduction mechanism.

- Derivation of the Mathematical model of magneto-mechanical oscillator configuration.

- The development of two approaches for center frequency selection using two machine learning algorithms to maximize power generation and provide real-time tuning.

1.3.1 Thesis Outline

Chapter 1 introduces the technical background and challenges of energy harvesting. It covers the common transduction mechanisms and circuit elements required to provide a stable reliable source of energy.

In chapter 2, a literature review is conducted on the recent research and trends in energy harvesting. It covers the more common designs used to implement electromagnetic energy harvesters and discuss the advantages and constraints of these designs.

Chapter 3 introduces new electromagnetic transduction mechanism for energy harvesting from vibrations, explaining the phenomenon behind the mechanism with detailed analysis, model and the mechanical design of a new energy harvester based on this transduction mechanism associated with experimental results and its analysis.

In chapter 3.5, an overview of the experimental results and tests conducted to characterize and model the FDH are introduced. This chapter also covers different prototypes and aspects of the FDH design parameters like the magnetic field configuration, coil structures, power generation and load analysis.

In chapter 4, two center frequency estimation methods using machine learing are presented. The methods are developed using Fuzzy C-means Clustering (FCM) and Artificianl Neural Network (ANN) machine learning algorithms, respectively, to estimate any desired center frequency based on experimental data. Estimating a desired center frequency allows for maximum power transfer at any excitation frequency without the need for the FDH to be pre-tuned. Along with simulations, a comparison on performance between the two algorithms is presented.

Chapter 5 reviews the research findings and contributions to the field of vibration energy harvesting.

Chapter 2

Literature Review

2.1 Introduction

In this chapter, we review mechanical vibrations, different transduction mechanisms used in vibration-based energy harvesting, signal conditioning circuitry, and survey state of the art energy harvesting from mechanical vibrations research, with a particular emphasis to electromagnetic energy harvesters.

2.1.1 Micro Energy Harvesting

In this section, techniques commonly deployed in micro-energy harvesting will be discussed. Three forms of energy are the most commonly harvested forms of energy due to the availability of legacy technology or to their high efficiency and abundance:

- Thermal energy.

- Solar energy.

- Kinetic energy.

- Thermal energy is one of the most available sources of energy on the planet found in air, human body, geothermal, and waste heat from fossil fuel based engines. The harvesting mechanism here is based on the "Seebeck effect" using a thermocouple, it is a device that consists of two dissimilar conductors, in-contact at one end, when heated a potential difference proportional to the temperature will develop across the non-contact ends. A basic illustration of a thermocouple is shown in figure 2.1. Due to developments in semiconductors technology and material science, thermo-electric energy harvesters have seen significant improvement in form-factor and efficiency.
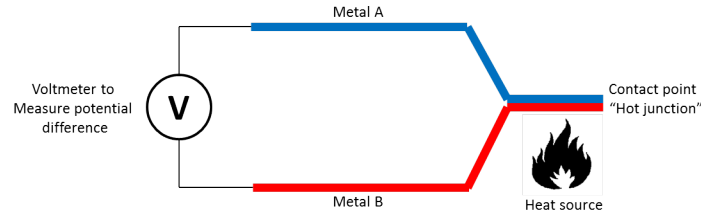
Figure 2.1: Basic thermocouple design

- Solar energy is the most commonly harvested form of energy. Photovoltaic cells are used to convert light photons to electrical energy.

- Kinetic energy can be harvested from nature, man-made structures, human motion, mechanical vibrations, and impact events. The next section will expand on the different technologies used to harvest kinetic energy.

2.2 Energy harvesting transduction mechanisms from vibrations

This section discusses the transduction mechanisms used to convert mechanical vibrations to electrical energy.

1. Piezoelectric: Piezoelectric materials develop potential difference along the surface of the material when exposed to strain, inversely; a piezoelectric material stimulated by an external potential difference undergoes strain. The structure of most energy harvester based on piezoelectric transduction involves a thin strip of piezoelectric material mounted on a simple cantilever beam exposed to vibrations, figure 2.2. When the beam oscillates a potential difference develops along the opposite surfaces of the piezoelectric material. The output voltage is proportional to vibration amplitude and the electromechanical coupling coefficients of the piezoelectric material. The output voltage for this transduction mechanism is relatively high which requires regulation using additional circuitry, however, the output current is relatively very low, in the orders of few micro or nano amperes, which affects the total generated power.

2. Electrostatic: This mechanism harvests accumulated charges between the two moving plates made of conducting materials and separated by an insulator material, similar to variable capacitors. Electrostatic harvesting exploits the proportional relationship between quantity of charges Q on the two plates and capacitance C when the potential difference V across the plates is held constant:

$$Q = CV_o \tag{2.1}$$
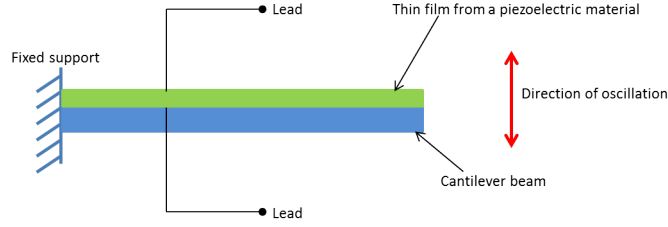
Figure 2.2: Basic design of a piezoelectric harvester
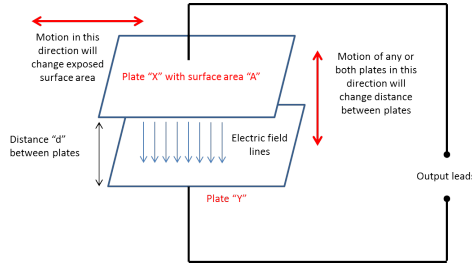
Figure 2.3: Basic idea of electrostatic energy harvesting

Where capacitance is function of the surface area of the plates A exposed to each other and the separation distance d between them:

$$C = \epsilon_r \epsilon_o \frac{A}{d} \tag{2.2}$$

where $\epsilon_o = 8.854 \times 10^{-12} F/m$ is space permittivity and ϵ_r is the relative permittivity of the dielectric material between the two plates.

Figure 2.3 illustrates the ways in which moving plate capacitor harvests electrical energy. Captured kinetic energy moves one of the two plates horizontally to change the exposed surface area and therefore capacitance. As a result, charges Q are collected and harvested as kinetic energy keeps varying the position of the capacitor plates. The same process can also be induced when kinetic energy is used to change the separation distance between the two plates. Electrostatic energy harvesters are designed to exploit either of these motion patterns.

3. Electromagnetic: Faraday's law of electromagnetic induction states that conductor moving across a magnetic field will develop potential difference across its terminals as it cuts the magnetic field lines. This transduction mechanism is based on using kinetic energy to create relative motion between a conducting wire and a magnetic field, Figure 2.4. The voltage generated across the conductor terminals V is proportional to the rate of change of the magnetic flux linkage ϕ.

$$V = -\frac{d\phi}{dt} \tag{2.3}$$
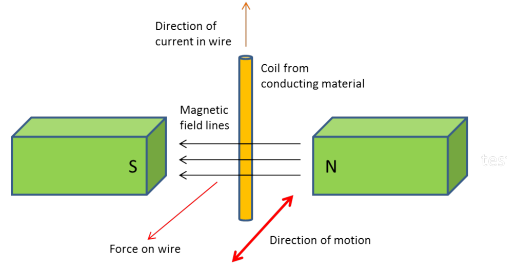
Figure 2.4: Basic principle of electromagnetic induction

When a coil with a number of turns N is used instead of a single turn conductor, the generated voltage is:

$$V = -N\frac{d\phi}{dt} \tag{2.4}$$

where ϕ in the average magnetic flux per coil turn. For electromagnetic harvesting, kinetic energy is used to change the relative position of the coil with respect to the magnetic field source, which varies magnetic flux as a function of displacement. Therefore, the output voltage can be expressed as:

$$V = -N\frac{d\phi}{dt}\frac{dx}{dt} \tag{2.5}$$

where dx/dt is the rate of change of relative displacement, velocity, in the x-direction.

2.3 Mass-Spring-Damper structures

Mass-spring-damper structure is very popular in building vibrations based harvesters because of their simplicity. The model representing this class of harvesters has been extensively researched and validated. The simplest design in this class is a mass mounted to a vertically aligned spring attached to a source of vibrations as shown in figure 2.5. When external vibrations are applied to the base support of the spring the mass will oscillate either vertically or horizontally. The harvester's behavior can be described by the equation of motion of the mass-on-spring mechanical oscillator [16].

The center frequency f_o of the harvester depends on the natural frequency of the oscillator:

$$f_o = \frac{1}{2\pi}\sqrt{\frac{k}{m}} \tag{2.6}$$

In figure 2.6, the energy harvester designed by Amirtharajah et al. [5] is shown. It uses a mass-on-spring and electromagnetic transduction to harvest vibrations from human body motion to power medical sensors implanted or placed on the surface of a human body. They achieved a center frequency of $f_o= 94\ Hz$ and an output power of 400 μW.
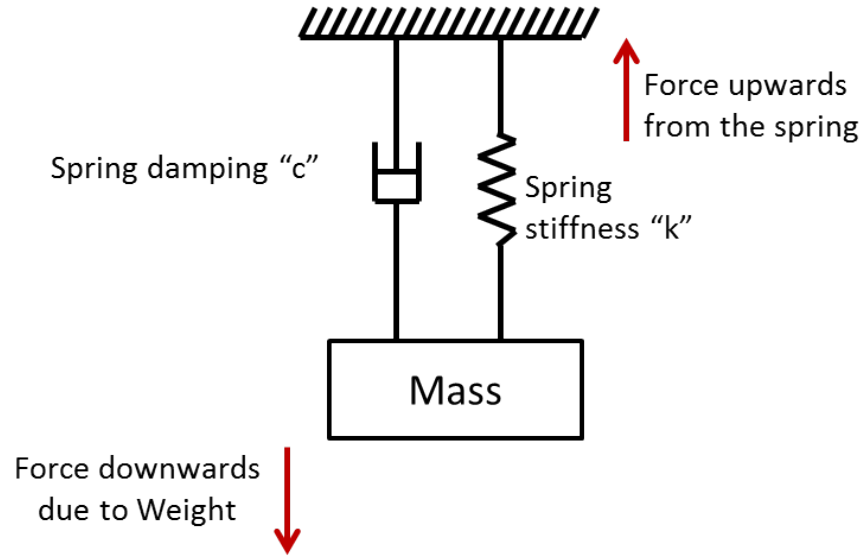
Figure 2.5: Basic mass-spring-damper structure
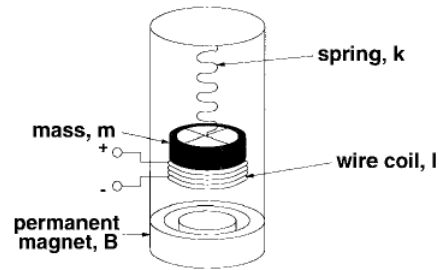
Figure 2.6: Amirtharajah et al. mass on spring based energy harvester design

Mann et. al. [4] design used a mass-on-spring harvester, shown in figure 3.20, uses a magnetic mass and magnets placed at both ends of a tube to serve as springs. Where each of the end magnets has a similar magnetic pole to that of the magnetic mass facing it. This harvester has center frequency f_o=5.12 Hz and generated output power up to 200 mW.

2.4   Beam-Support structures

Beam-support structures are the other common class of energy harvesters. Most of these harvesters use either cantilever or guided-end beams to support a seismic mass and/or a coil. The beams in this case behave as springs and add to the seismic mass. An illustration of the beam-support structure is shown figure 2.8. The stiffness of a cantilever beam spring is calculated using the formula

$$k = \frac{3EI}{L^3} \tag{2.7}$$
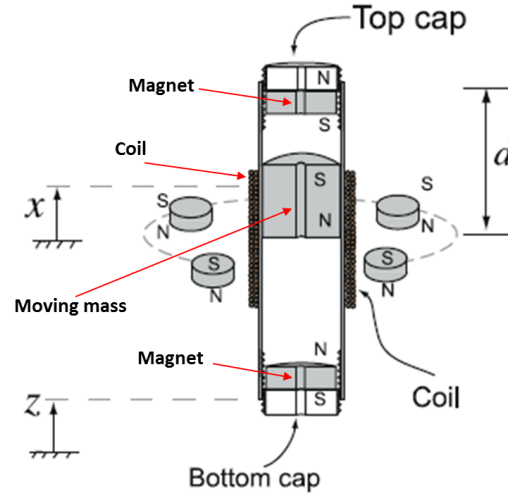
Figure 2.7: Mann et. al. design of mass-on-spring harvester
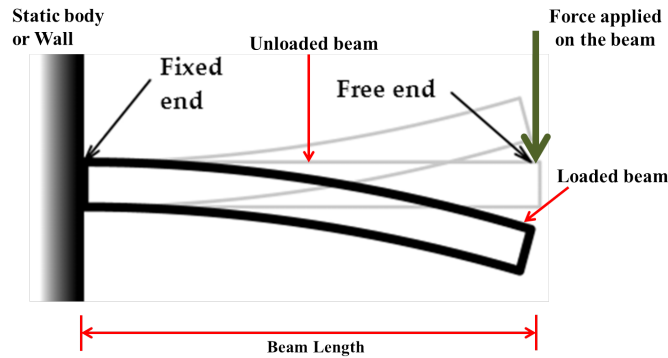
Figure 2.8: Basic Beam-Support structure

where E is Young's modulus describing the strength of the material, I is the second moment of area of the beam cross-section, and L is the beam length.

Sari et. al. [7] design used a coil mounted on top of a cantilever beam surface facing magnet poles, shown in figure 2.9, once the cantilever beam is under excitation voltage starts to induce in the coil, achieving center frequency between 3.5-4.5 KHz depending on beam length and maximum output power of $0.4\mu W$.

Beeby et. al. [6] design used a coil mounted to the beam free end facing two magnet poles, shown in figure 2.10, achieving center frequency between 52.1-53.2 KHz and maximum output power of $45.8\mu W$

2.5   MEMS in energy harvesting

Modern energy harvesters require a small profile for portability and integration into other systems, driving a trend to scale down the mechanical oscillator used in the harvesters. Micro Electro
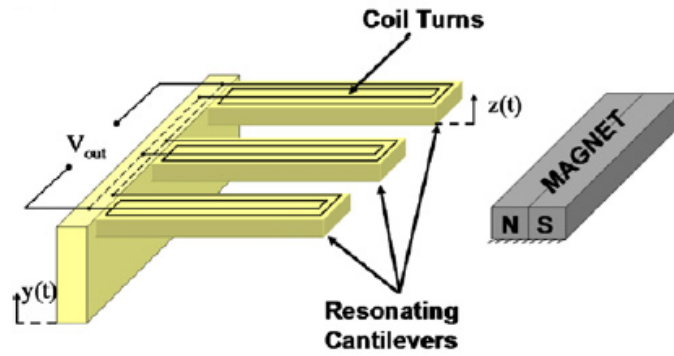
Figure 2.9: Sari et. al. electromagnetic harvester
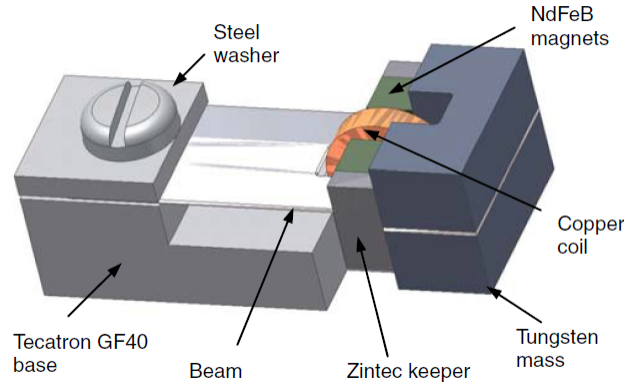
Figure 2.10: Beeby et. al. micro cantilever harvester

Mechanical Systems (MEMS) technology afforded the tools and mechanisms required to achieve smaller profiles. The past few years has seen intensified work on rebuilding the common structures and models used in vibrations based energy harvesters at micro-scale using MEMS technology.

While these types of energy harvesters are capable of generating electrical energy with output power on the order of milli-Watts, their natural frequency must be tuned to match the frequency of ambient vibrations. In environments where ambient vibrations are only available at low frequencies, this proves to be quite a challenge. In many built environments, ambient vibrations are only available at low frequencies. It is therefore impractical to use traditional VEHs that have relatively high center frequency ($\geq 10Hz$) to harvest low frequency ($\leq 10Hz$) vibrations. As a result, there has been an interest in realizing low center frequency VEHs.

Wang et. al. [8] used mass-on-spring structure to design an electromagnetic based harvester at MEMS scale, mounted an inertial magnet mass mounted on spiral net-like spring and below the mass-spring structure a stationary coil mounted on the device base, harvesting with the oscillation of the spring, shown in figure 2.11, achieving center frequencies around $48.58\ Hz$ and $146.72\ Hz$
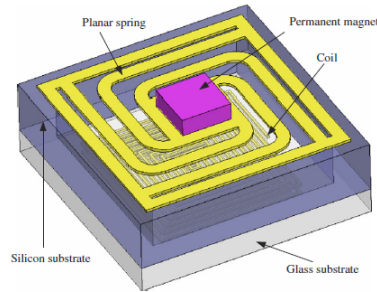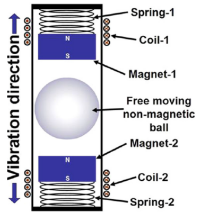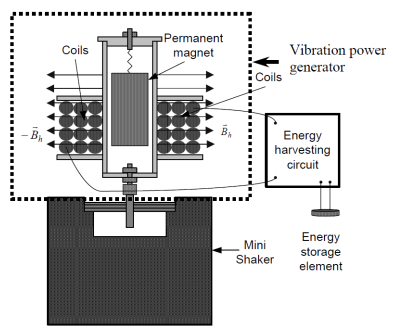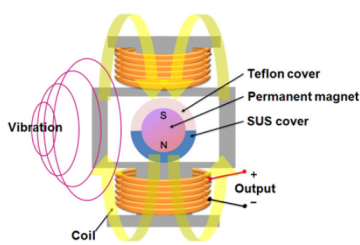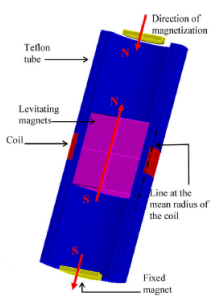
Figure 2.11: Mass mounted to wall with four springs fabricated using MEMS technology

and able to output up to 104 nW.

Table 2.1 shows different VEH designs varying between mass-on-spring and cantilever-beam structures, with their center frequency (f_c) and output power at resonance listed. Many of the current VEH designs aren't capable of harvesting at frequencies below $20Hz$ as Halim et. al. [45], Cao et. al. [56], Wang et. al. [8], Beeby et. al. [6] and many others, which limits the amount of kinetic energy harvested as discuss in previously, while designs that is able to harvest low-frequency vibrations struggled with issue of very low output power (below 100 μW) that isn't enough to operate or charge many electronic systems, like Fondevilla et. al. [60], Minami et. al. [55] and Moss et. al. [61] [62]. While designs like Dallago et. al. [54] and Haroun et. al. [49] were able harvesting at low frequencies and generate an amount of power that can utilized by a variety of system.

Table 2.1: Different VEH Designs & Architectures

Energy Harvester	Center frequency (Hz)	Output Power (W)	Harvester's Design
Electromagnetic energy harvester, Mass-spring based electromagnetic harvester [45]	51	$110\mu W$	
Electromagnetic energy harvester, Mass-spring based harvester [56]	42	Chip based harvester: $4mW$ PCB based harvester: $35mW$	
Vibration energy harvester using a spherical permanent magnet, Mass-spring based electromagnetic harvester [48]	20	$9.03\mu W$ at $3g$	
Vibration energy harvester, Mass-spring based electromagnetic harvester [54]	10.4	$0.013W$ at $1g$	

Micro electromagnetic vibration energy harvester mass-spring based electromagnetic harvester [49]	3.33	Design D9xL12: $113.3\mu W$ Design D7xL12: $82.9\mu W$ at $12.38\ m/s^2$	
up conversion Mass-spring based piezoelectric harvester [50]	15	$10\mu W$	
Piezoelectric energy harvester, cantilever-beam based harvester [55]	5	$1.2\mu W$ at $5mm$	
Electromagnetic energy harvester for scavenging abient energy, mass-spring based harvester[60]	N/A	$1.2\ \mu W/cm^3$ at $12°$ inclination	
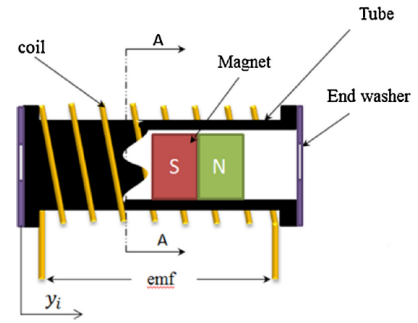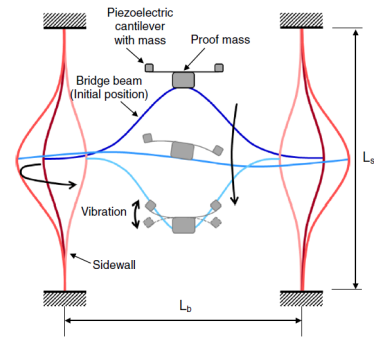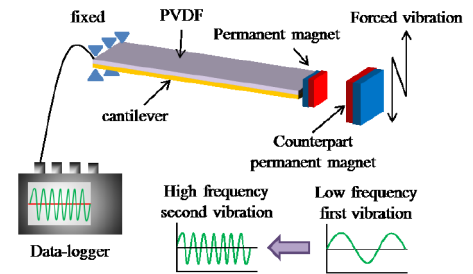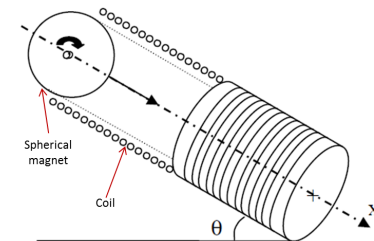
Vibration energy harvesting using a spherical permanent-magnet, mass-spring based harvester [61] [62]	$5.4Hz$	$33\mu W$ at $500mG$	
Bi-Axial magnetoelectric VEH, mass-spring based harvester [64]	$9.8\ Hz$	$121\ \mu W$ at $61\ mG$	
Multi-frequency hybrid VEH (Piezoelectric + Magnetic) [11]	$22.8Hz$ $25.8Hz$	$1.2mW$ $2.57mW$	
Magnetoelectric and electro-magnetic composite VEH [12]	$27.5Hz$	$16.57\mu W$	
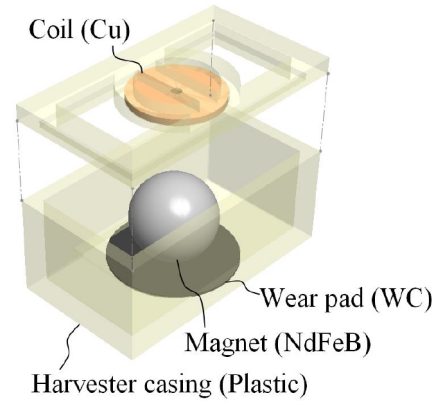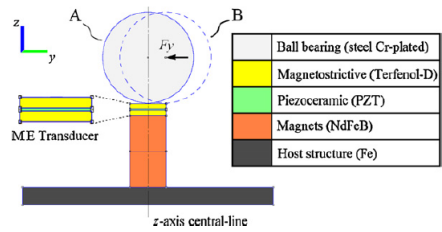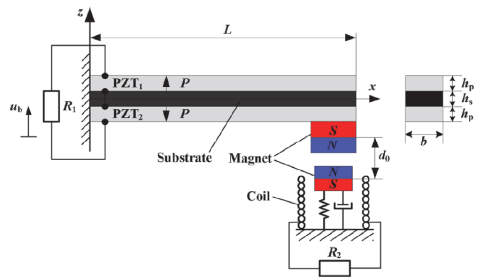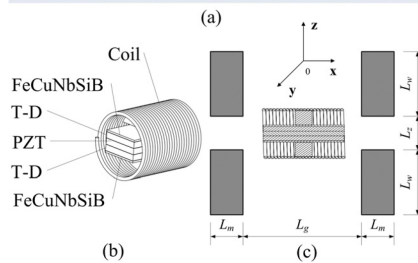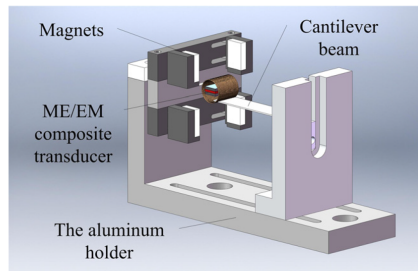
2.6   Signal Conditioning

The ability of energy harvesters to supply power on demand and in DC form is essential to their successful commercial deployment. On the other hand, the input power from the environment to micro-energy harvesters is intermittent and low. Therefore, an important challenge in the design of micro-energy harvesters is to rectify and store output power in order to guarantee stable, continuous and sufficient supply of power. Further, electromagnetic energy harvesting encounter additional challenge, its output voltage is on the order of a few to a few hundreds of mili-volts, which requires to be stepped up. The following solutions can be used to resolve such challenges:

- Using a charge-pump DC-DC converter, voltage multiplier, or a step-up transformer to boost the output voltage to meet the requirements of electronic power supply and increase the efficiency of rectification circuits.

- Using passive or active full-wave rectifier circuits to rectify the output of the harvester and stabilize it to a constant level.

- Using a rechargeable battery or a super capacitor to store the DC energy. The storage element will act as the supply to the target system while the harvester charges it instead of powering up the target system directly.

2.7   Electromagnetic Energy Harvesting

2.7.1   Electromagnetic Induction

According to Farady's law of induction, a potential difference is induced across a conductor terminals when exposed to a varying magnetic field, hence we must have either a moving conductor against a stationary magnet poles to create a time varying magnetic field that will be cut by the single turn or multiple turns conductor. Recalling equations 2.8 and 2.9, the governing relations are:

$$V = -\frac{d\phi}{dt} \tag{2.8}$$

in case of multiple coil turns:

$$V = -N\frac{d\phi}{dt} \tag{2.9}$$

where N is the number of coil turns, this relation applies to rotary motion generators, while electromagnetic VEH uses linear motion to displace the coil versus magnet motion in order to create a time varying magnetic field, hence voltage is induced across the coil terminals, from

equations 2.8 and 2.9 external forcing and damping (both electrical and mechanical) affect directly the velocity of the moving proof-mass carrying either the magnets or the coil, the governing relation must be re-written to consider the velocity term to be:

$$V = -N\frac{d\phi}{dt}\frac{dx}{dt} \tag{2.10}$$

where dx/dt is the rate of change of relative displacement, velocity, in the x-direction.

2.7.2 Magnetic Restoring Force

With the linear motion of the VEH, there is a force that affects the moving proof-mass due to the magnetic fields from permanent magnets and the coil's counter field resulted from the induced voltage called "magnetic restoring force", the magnetic restoring force affects the speed and damping of the VEH and hence the resulted output power, and the equation of motion will be:

$$m\ddot{x} + (c_e + c_m)\dot{x} + kx + F_{\mathrm{m}}(x) = -m\ddot{y} \tag{2.11}$$

where $F_{\mathrm{m}}(x)$ is the magnetic restoring forces, and it varies with the proof-mass position. And c_e and c_m are the electrical and mechanical damping, respectively. The magnetic restoring force relationship depends on the interaction between the mechanical oscillator and magnetic field configuration in the harvester structure. Mann et al.[4] defined the restoring magnetic force in terms of magnetization, magnetization vector, displacement and spacing between different magnets in the structure:

$$F_m(y) = \frac{\mu_o M_c v_c}{2\pi}\left(M_t v_t\left(\frac{3}{(d-y)^4} - \frac{3}{(d+y)^4}\right) - \frac{M_o V_o N}{2}\left(\frac{5y}{(y^2 + R_o^2)^{\frac{5}{2}}} - \frac{5y^3}{(y^2 + R_o^2)^{\frac{7}{2}}}\right)\right) \tag{2.12}$$

Sari et al.[7] defines the magnetic restoring force in terms of magnetic field density B, beam length L_P, load R_L and coil resistances R_c and proof-mass acceleration $\ddot{Z}$:

$$\bar{F}_m = \frac{(BL_P)^2}{R_L + R_C}\ddot{Z} \tag{2.13}$$

Patel et al.[20] defines the magnetic force in terms of velocity of the proof-mass and the electromagnetic coupling in the system:

$$F_{\mathrm{m}} = D_{\mathrm{em}}v = \frac{V_{\mathrm{ab}}^2}{(R_L + R_C)v^2} \tag{2.14}$$

where electromagnetic damping in this harvester D_{em} is defined in terms of induced voltage across the coil, load resistance, coil resistance and proof-mass velocity. Bendame et al. [15] defines the

magnetic force in terms of magnetic field density, speed and effective length of the coil:

$$F_\mathrm{m} = \frac{Bl^2}{R_L + R_C}\frac{dx}{dt} \tag{2.15}$$

The presented electromagnetic VEHs in this section, showed that magnetic restoring force is a function of mechanical design parameters (spacing, beam length, effective coil effective length), dynamic parameters (velocity and acceleration), and electrical characteristics (coil and load resistances) and magnetic field configuration.

2.7.3   Nonlinearity in Electromagnetic VEH

Mechanical oscillators forming energy harvesters behave linearly if operating at ideal conditions at free-undamped vibrations; however this is not the case for forced-damped vibration, the subject of interest for VEH, where most of the vibrations exist in the environment are due to natural occurrences or man-made are forced-damped vibrations kind. The causes of nonlinearity in electromagnetic VEH are mainly mechanical stiffness and electromagnetic hysteresis from electromagnetic structure. A simple mechanical mass-on-spring equation of motion is:

$$m\ddot{x} + kx = 0 \tag{2.16}$$

which applies for linear springs obeying Hooke's law, however a deviation from linear stiffness occurs when the spring is under large compression or tension, depending on the material of the spring, resulting in rapid increase in the restoring force more than displacement, hence the equation of motion becomes:

$$m\ddot{x} + k(x \pm \mu_o^2 x^3) = 0 \tag{2.17}$$

where the term $\mu_o^2 x^3$ represents the stiffness nonlinearity that appears with large compressions or tensions, the positive $\pm\mu_o^2 x^3$ term indicates hardening nonlinearity, while a negative $\pm\mu_o^2 x^3$ term indicates a softening nonlinearity, the same explanation applies to magnetic springs if they exhibit similar behavior.

2.7.4   Electromechanical Coupling in Electromagnetic VEH

Electromechanical coupling is the ratio between converted and total energy involved in transformation cycle [21], electromechanical coupling evaluates the VEH efficiency of energy conversion between the mechanical oscillator and the electromagnetic structure. With different VEH designs and structures, the electromechanical coupling coefficient is either derived analytically or measured experimentally, the method to obtain it varies upon the complexity of the VEH design and the clarity of the output responses versus frequency & acceleration profile.

Assuming the magnetic field density is uniform across the area of interest within the VEH, the electromechanical coupling coefficient α can be simplified to be [18][4][22]:

$$\alpha = Bl \tag{2.18}$$

where B is magnetic field density, and l is the coil length, for a coil with number of turns N:

$$\alpha = NBl \tag{2.19}$$

however the formula for electromechanical coupling coefficient α, shown in equations 2.16 and 4.1, cannot be standardized for all electromagnetic VEH due to complexities that might appear in magnetic field distribution or coil design.

2.8   Summary of Shortcomings in Vibrations-based Energy Harvesting

This chapter reviewed many VEH designs and the different design parameters that contribute to the performance of a VEH in the pursuit of increasing generated power, specially at low frequencies, below $20Hz$, where it is more abundant in kinetic energy, we can summarize the shortcomings in the current state-of-art in the following:

- Harvesting at low frequencies: many of the current designs aren't capable of harvesting low frequency vibrations where kinetic energy is most abundant, while harvesting at higher frequencies doesn't allow for enough power to be generated and makes the VEH less beneficial.

- Large physical profile: which makes the harvester less suitable for portable applications that require miniature profile.

- Very low output power: due to transduction mechanism limits.

- Very narrow harvesting bandwidth: which reduces the generated output power.

- Inflexible design, not allowing for smooth tuning of the VEH center frequency or harvesting bandwidth.

The next chapters introduce a VEH design that is able to harvest low frequencies below $10Hz$ while maintaining a small physical profile and lightweight proof-mass, at the same time, capable of generating enough power for many low-power electronic systems.

Chapter 3

Field Disruption Energy Harvester: Principle, Model & Experiments

3.1 Introduction

In this chapter, principle of operation and modeling of field disruption energy harvester (FDH) [32] are introduced, along with a thorough analysis to design a robust FDH. FDH deploys a novel electromagnetic transduction mechanism to generate electricity from harvested kinetic energy, dubbed "induction by field disruption", which is by disrupting a stationary magnetic field by a moving ferromagnetic object, thus inducing voltage in a stationary nearby coil structure, the presented model identifies the relation between the main components of the mechanical oscillator, electromechanical coupling in the system, the effect of mechanical and electrical damping, acceleration of the moving object, and the exerted magnetic restoring force on the voltage-frequency response and resulted nonlinearity.

An energy harvester employing this transduction mechanism is realized by placing a stationary coil winding inside a magnetic field created by stationary magnets, and allowing a ferromagnetic object to move along the coil. The assembly is attached to a host body, such that waste motions would cause the free moving object to travel. The high permeability of the ferromagnetic object increases the concentration of field lines in its vicinity, thereby disrupting the magnetic field cutting the coil and inducing potential difference V across the coil terminals. The ferromagnetic object and end-limiters placed at the ends of its track comprise a mechanical oscillator used to capture kinetic energy. Similar to other vibration-based energy harvesters, the oscillator can only
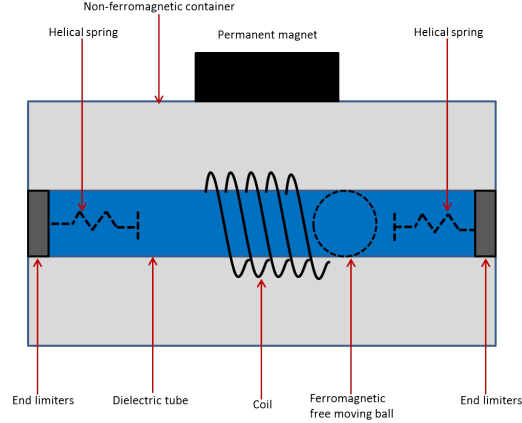
Figure 3.1: Side view of the FDH prototype [32]

capture kinetic energy efficiently in a limited interval of the frequency spectrum, the harvesting bandwidth, extending around its natural frequency, the center frequency of the energy harvester.

The harvester design realizes two critical challenges for VEH: harvesting low center frequency ($\geq 10Hz$) vibrations, and tunable to fit wider frequency bands without significant changes to the FDH oscillator design via different mechanisms such as coil inductance, magnetic field configuration by changing the orientation of the magnetic field that impacts the generated output power, system stiffness, center frequency and harvesting bandwidth. Furthermore, increasing number of coil turns increases the output voltage, however, imposes changes on the system nonlinearity.

3.2   Principle of Operation

The FDH consists of a copper coil wound around a dielectric tube, a single magnet on top of the coil-tube assembly, and an inertial ferromagnetic mass. The inertial mass, a steel ball, moves freely along a low-friction track inside the tube. Two springs are mounted to the end caps of the tube to terminate the ball motions. The tube and magnet are mounted to a dielectric container, such that the magnet is placed above the tube mid-section. The prototype of the FDH is shown in figure 3.1.

A top-view of the FDH, shown in figure 3.2, illustrates the placement of the steel ball and the end-limiters. The limiters are made of steel helical springs backed by rubber desks mounted directly to the walls of the container. The figure also illustrates the concentric placement of the coil, tube, and ball as well as the tube, rubber desks, and helical springs. The distance between the top magnet and the surface of the coil d, measured coil resistance R_c and the magnetic field density at the center of the tube $B_\circ$ in the absence of the ball in the fabricated FDH prototype are listed in table 3.1.
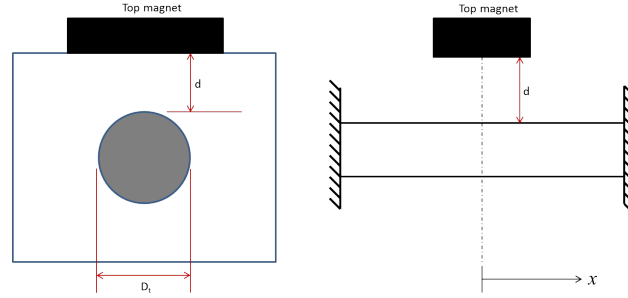
Figure 3.2: Rear and side view schematics of the FDH

Table 3.1: Harvester specifications

Parameter	Value
Top magnet to coil (Arrangement 1): d (mm)	16
Coil resistance: R_c (Ω)	10.6
Magnetic field intensity (Arrangement 2): $B_\circ$ (Gauss)	-790

3.2.1   Center frequency, Harvesting bandwidth and Nonlinearity

In addition to the impact of mechanical design parameters on FDH center frequency and band-width such as the mass of moving object, dielectric tube friction coefficient and end-springs stiffness, other important variables impact the electromechanical coupling, and hence, affect center frequency and harvesting bandwidth significantly, such as excitation amplitude, magnetic field strength of the permanent magnet(s), magnetic field orientation and coil inductance. Experiments showed that the center frequency can be anywhere between 6.27 Hz and 12.72 Hz, same applies to harvesting bandwidth that ranged between 0.86 Hz and 6 Hz depending on the parameters and variables mentioned. Nonlinearity in FDH V-F response is a result of the effect of both mechanical stiffness and magnetic field, creating "softening nonlinearity". However, the counter magnetic field created by the coil impacts the total magnetic field, and thus magnetic spring stiffness, which decreases the softening nonlinearity and possibly changing it to a "hardening nonlinearity" if it is significantly high.

3.3   FDH System Model

The FDH consists of two coupled mechanical oscillators, the first one is a mechanical impact oscillator comprised of a steel ball moving between two end-springs along the motion track, a Teflon tube, the second oscillator is a magnetic mass-on-spring, the top magnet acts as a tension spring, impacting the motion of the steel ball excited externally. An illustration of the two coupled oscillators is shown figure 3.3.

The steel ball moves freely along a coil-carrying tube in response to base excitations $y(t)$ of
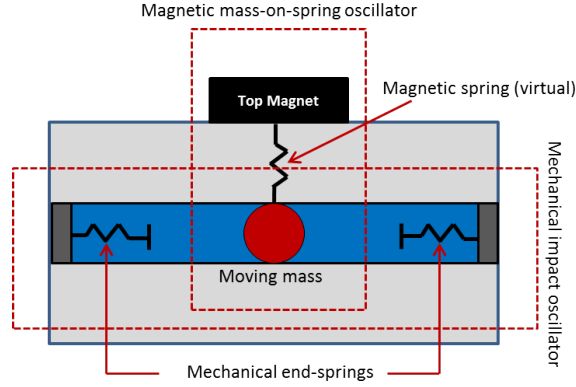
Figure 3.3: Magnetostatic-Mechnical Oscillator architecture used in the FDH
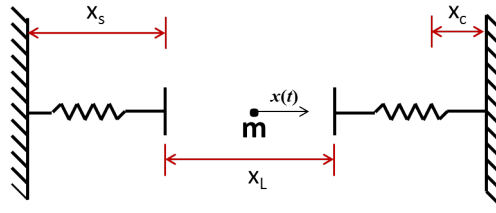
Figure 3.4: A schematic of the harvesting oscillator in the FDH

the tube. The motion of the ball $x(t)$ relative to the tube induces a voltage $V(t)$ across the coil terminals. A schematic of the harvesting oscillator appears is shown in figure 3.4, where the ball is modeled as a point mass. The origin of ball displacement x is taken at the track mid-point. The equation of motion of the ball describes the balance between the ball inertia and the forces applied to it:

$$m(\ddot{x} + \ddot{y}) + (c_m + c_e)\dot{x} - F_s(x) - F_m(x) = 0 \tag{3.1}$$

where m is the ball mass, c_m is a viscous damping coefficient representing all loss mechanisms acting on the ball, c_e is the electromagnetic damping coefficient, $F_s(x)$ is the mechanical restoring force due to the interaction of the ball and end-springs, and $F_m(x)$ is the magnetic restoring force resulting from interaction between the ball and top magnet. The free-travel distance of the ball is equal to the difference between the track length x_t and the sum of the ball diameter D_b and the unstretched length of the end-springs x_s:

$$x_L = x_t - D_b - 2x_s \tag{3.2}$$

We identify three interaction patterns of the end-springs with the ball:

- No interaction while the ball is traveling freely in the mid-section of the tube;

- Contact with the spring as it approaches either end; and
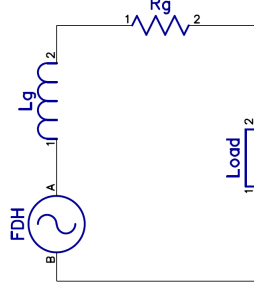
Figure 3.5: FDH Electric Model

- Contact with a fully-compressed spring during the terminal stage of large-sized oscillations.

Therefore, the end-springs force-displacement relationship can be written as:

$$F_s(x) = \begin{cases} 0 & \frac{1}{2}x_L \leq x \leq \frac{1}{2}x_L \\ k_1(\frac{1}{2}x_L - x) & \frac{1}{2}x_L \leq |x| \leq \frac{1}{2}x_L + x_s - x_c \\ k_1(\frac{1}{2}x_L - x) & \frac{1}{2}x_L + x_s - x_c \leq |x| \leq \frac{1}{2}x_L + x_s + k_2(\frac{1}{2}x_L + x_s - x_c - x) \end{cases} \tag{3.3}$$

where x_c is the fully compressed length of the springs, and k_1 and k_2 are the stiffness and the fully compressed stiffness of the springs, respectively. The magnitudes of the spring parameters were measured for the fabricated prototype and are listed in table 3.2.

Table 3.2: FDH mechanical and electrical specifications

Parameter	Value
Travel track total length (mm)	72
Unstretched end-spring length (mm)	14.5
Compressed end-spring length (mm)	13.5
End-spring inner diameter (mm)	8.9
End-spring outer diameter (mm)	10.75
Stainless steel ball diameter (mm)	13.05
Stainless steel ball mass (grams)	8.9
Proof-mass travel distance (mm)	30
Distance between top magnet and coil (mm)	14
Distance between side magnets (mm)	26.3
Coil inductance (μH)	3.4
Coil resistance (Ω)	10.6
Coil number of turns	970
Top magnet part number[80]	BY0X08DCS

3.3.1   FDH Electric Model

FDH electrical model and equivalent circuit shown in figure 3.5, adopts the same model of magnetic vibration energy harvesters[36] [37], where the FDH side is a voltage source in series with source
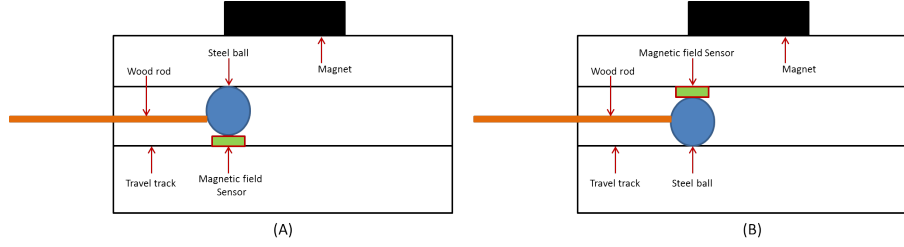
Figure 3.6: Magnetic field measurement setup, figure A: measuring magnetic field on the ball, figure B: measuring external magnetic field

inductance and resistance of the coil configuration. This model was validated by testing the impact of source inductance and resistance on output power, as changing the type of load used impacted the power delivered in terms of peak power. Experimental results and analysis are presented in next chapter.

3.3.2   Magnetic Restoring Force

The magnetic field distribution inside the harvester was investigated experimentally using hall effect sensor probe, shown in the setup in figure 3.6, to measure the magnetic flux density (B) on the ball, we mounted the steel ball on top of the probe and moved it along the travel track to get magnetic flux density versus displacement, following the same procedure, we measured the external magnetic flux density applied from the permanent magnet without the steel ball mounted, both magnetic field density applied externally and on the steel ball are shown in figure 3.7.

Figure 3.7 shows the distribution of the magnetic flux density in the absence of any ferromagnetic object in the vicinity of the magnet, the magnetic flux density is minimum at the mid-point of the track, then it increases gradually as the sensor probe moves away toward the ends, on the same figure, the magnetic field density on the steel ball, graphed in blue, shows an opposite behavior when the steel ball is inserted in the magnetic field as it tries to concentrate the magnetic field lines as it gets closer to mid-point of the track, which happens due to the magnetic properties of the stainless steel ball used in the harvester design [43]. Magnetic field inside a sphere made of linear isotropic material is [43] [59]:

$$\mathbf{H_{in}} = \mathbf{H_o} + \mathbf{H_d} = \mathbf{H_o} - \tfrac{1}{3}\mathbf{M} \tag{3.4}$$

where H_o is the external magnetic field, H_d is the demagnetization field inside the object and M is the magnetization of the sphere, recalling magnetization for soft magnetic materials:

$$\mathbf{M} = \chi_{\mathbf{m}}\mathbf{H_{in}} \tag{3.5}$$
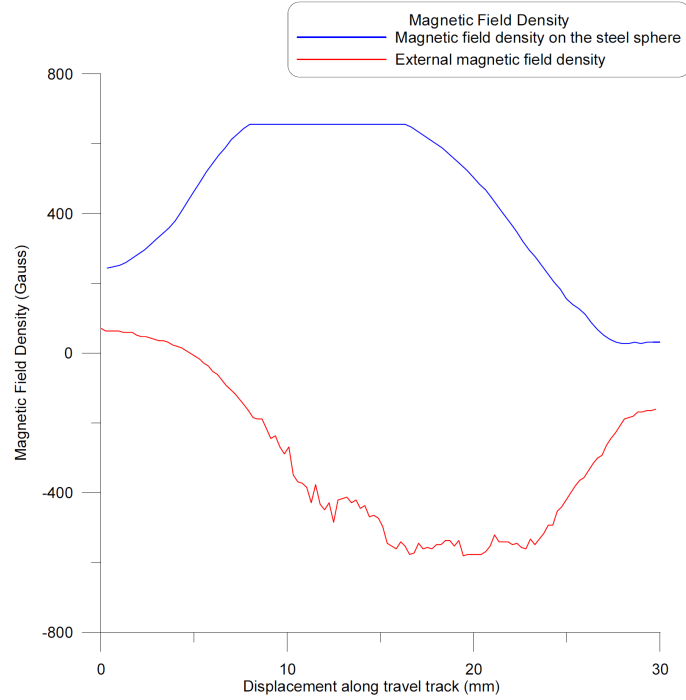
Figure 3.7: External magnetic field density by the magnet (bottom, in red) and magnetic field density on the steel ball (top, in blue)
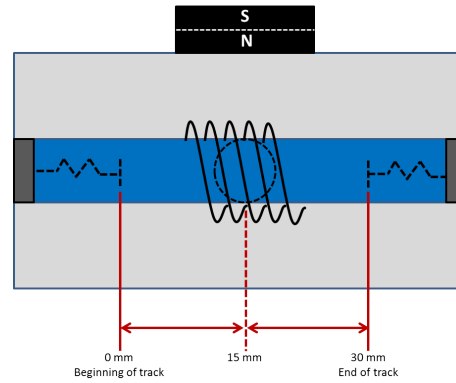
Figure 3.8: Explanatory figure of displacement along the travel track and direction of magnetization of the top magnet

where χ_m is the magnetic susceptibility of the ferromagnetic moving sphere. It is a measure of magnetization in response to applied magnetic field. For isotropic material (such as steel) χ_m isn't direction dependent, and the magnetization & field vectors are proportional and aligned [59], substituting equation 3.5 in 3.4:

$$\mathbf{H_{in}} = \frac{\mathbf{H_o}}{1 + \frac{\chi_m}{3}} \tag{3.6}$$

also, the magnetic susceptibility is a function of permeability:

$$\chi_m = \frac{\mu}{\mu_o} - 1 \tag{3.7}$$

where μ is the material specific permeability and $\mu_o = 4\pi \times 10^{-7} N/A^2$ is the free space permeability. The permeability of stainless steel ranges between 40 and 95 [79], we used $\mu = 95$. Substituting with equation (3.7) in equation (3.6) we get:

$$\mathbf{H_{in}} = \frac{3\mathbf{H_o}}{2 + \frac{\mu}{\mu_o}} \tag{3.8}$$

then we substitute with H_{in} in 3.5 we get:

$$\mathbf{M} = \frac{3(\mu - \mu_o)}{\mu + 2\mu_o} \mathbf{H_o} \tag{3.9}$$

Recalling the basic relationship between magnetic field intensity H and magnetic flux density B:

$$\mathbf{H} = \frac{\mathbf{B}}{\mu} \tag{3.10}$$

the magnetic flux density at a point x nearby an external source of magnetic field is governed by [43]:

$$\mathbf{B(x)} = \frac{\mu_o}{4\pi} \int \frac{\sigma_m(\mathbf{x'})(\mathbf{x} - \mathbf{x'})}{|\mathbf{x} - \mathbf{x'}|^3} \mathbf{ds'} \tag{3.11}$$

where σ_m is the magnetic surface charge of the magnet which is obtained from the permanent magnet datasheet, x' is the source point; the geometric center of the permanent magnet. The applied magnetic force on the moving steel ball is [43]:

$$\mathbf{F} = (\mathbf{M}.\nabla)\mathbf{B_{ext}} \tag{3.12}$$

where $\bar{F}$ is the magnetic force acting on the moving ferromagnetic object, $M.\nabla$ is the magnetization gradient and B_{ext} is the external magnetic flux density.

The magnetic restoring force on the steel ball is minimum and almost equals to zero as it crosses mid-point of the travel track, then it increases gradually to reach its maximum at the ends of the track due to reduction in magnetic flux density B, because of the presence of the steel ball.

3.3.3   Magnetic Field Simulation

The magnetic characteristics of the FDH, shown in figure 3.8, were simulated and analyzed using QuickField finite element analysis (FEA) software package, The goal of the siumlation is to
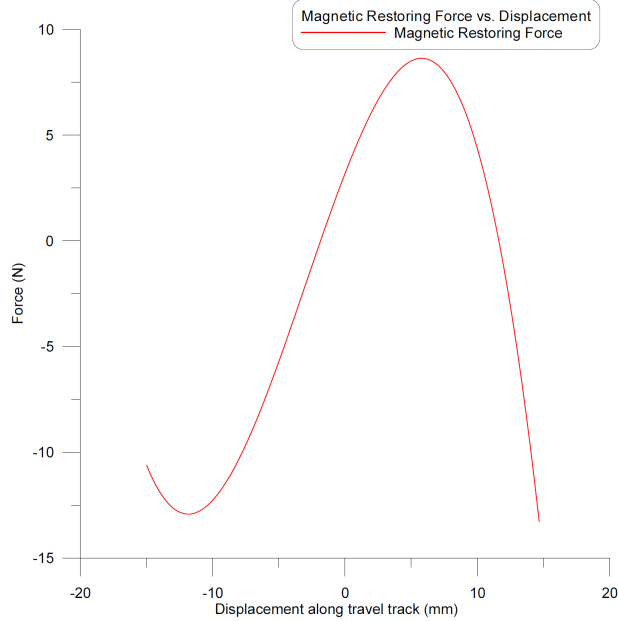
Figure 3.9: Magnetic force on exerted on the moving steel ball inside the FDH

validate and provide more insight for the magnetic field measurements presented in section 3.3.2. The magnetic restoring force applied on the moving ferromagnetic object, the steel ball, is a function of the euclidean distance between the steel ball and the permanent magnet. The simulations calculated the force exerted on the ball at different locations by the means of magnetic flux density B and magnetic field intensity H distributions in the vicinity of the source of magnetic field and the moving object. Multiple simulation runs were conducted after placing the moving object at different locations with respect to the permanent magnet to validate the simulation outcomes with the results of the experimental setup shown in figure 3.12. In the experiment shown in figure 3.12, shock and magnetic flux density sensors were implanted in the FDH hardware. A piezoelectric shock sensors replaced the end-springs to measure the force of the steel ball. A ratiometric hall-effect sensor was placed in the mid-point underneath the travel track at a close distance to measure the magnetic flux density B. This setup was excited with an $0.9g$ sine wave signal that swept from 5 to 25 Hz. The waveforms shown in figure 3.12 are measured output at resonance of the shock sensors, graphed in blue and purple, the FDH output voltage, graphed in green, and the magnetic flux density, graphed in yellow. As observed from the waveform, the FDH output voltage is almost zero when the ball is at impact with any of the shock sensors (maximum peak of the shock sensors output voltage), at the same moment the hall-effect sensor output is at its minimum, indicating no magnetic flux lines being cut at the moment of impact, which aligns with simulation results shown in figures 3.10 a and 3.10 e, where the magnetic field density is at it's lowest point when the ball is at the farthest distance from the permanent magnet (moment of impact). The FDH output voltage and the hall-effect sensor are at their peak at the
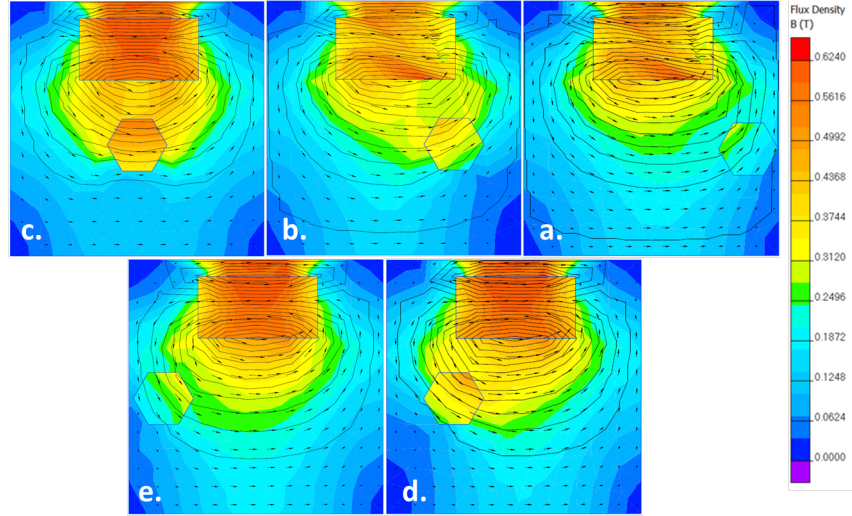
Figure 3.10: Magnetic flux density B distribution for different locations of the moving object

same moment, indicating the maximum magnetic flux lines being cut, generating the maximum voltage, which aligns with the magnetic flux density B simulations shown in figures 3.10b, 3.10c and 3.10d. The mechanical force exerted on the steel ball obtained from FEA simulations using QuickField, shown in table 3.3, aligns with the modeled magnetic restoring force shown in figure 3.9, where the highest value of the magnetic restoring force are at points b and d, and the lowest force exerted is at the farthest point for the steel ball from the permanent magnet. The mid-point of the travel track, which aligns with the center of permanent magnet is the equilibrium point of the restoring force. The interaction between of the permanent magnet with the moving steel ball exhibits the same behaviour as a mass-on-spring oscillator.

The magnetic restoring force at different positions might seem unusual at the first look, but lab measurements along with simulations confirmed the values, and it makes more sense knowing the permamnent magnet used has a pull-force of 74 lbs [80].

The presence of asymmetry in figure 3.9 should be acknowledged, as it may stem from measurement errors, such as the offset error of the hall effect sensor employed for magnetic flux density measurements. Furthermore, any misalignment in the permanent magnet or the sensor's orientation has the potential to introduce inaccuracies.

3.3.4   Permanent Magnet Geometry and Magnetic Resotoring Force

The strength of the demagnetization field in a permanent magnet depends on its geometry [97] [98]. This, in turn, affects the magnetic restoring force applied on the moving steel ball, altering the center frequency and harvesting bandwidth of the FDH. Therefore, it became necessary to investigate the influence of various magnet geometries to comprehend their impact.
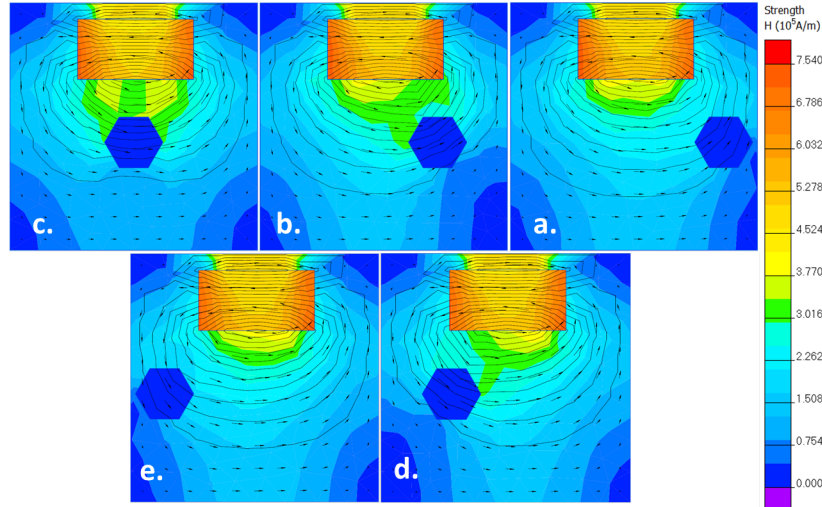
Figure 3.11: Magnetic field intensity H distribution for different locations of the moving object
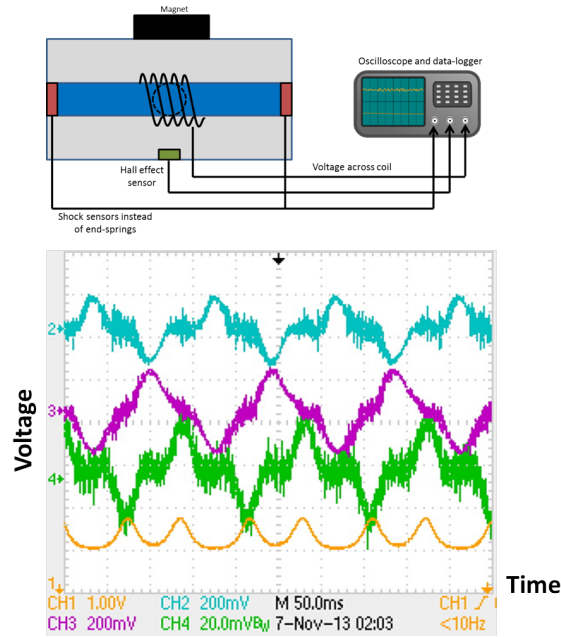
Figure 3.12: Impacts and magnetic field measurement, waveform in blue and purple are the shock sensors output, green waveform is the FDH output voltage, and the yellow waveform is the measured magnetic flux density at the travel track mid-point

The FDH prototype shown in Figure 3.1 underwent simulation using two permanent magnets of identical material and grade, namely, $NdFeB$ and N42, respectively. However, the magnets differed in size and are referred to as Magnet A and Magnet B respectively.

Magnet A was simulated to map the features of part number "BY0X04DCS" from K&J Magnetics [81], having dimensions of $2 \times 1 \times \frac{1}{4}$ inches. Magnet B was simulated to map the features of part number "BY084DCS" from K&J Magnetics [82], having dimensions of $2 \times \frac{1}{2} \times \frac{1}{4}$ inches.

Table 3.4 presents the mechanical force exerted on the steel ball at various positions, acquired

32

Table 3.3: Mechanical force applied on the steel ball for positions $a - e$ along the travel track axis shown in figure 3.10 from QuickField simulations

Object position	Force (N)
Position a	-7.93
Position b	-13.46
Position c	7.31
Position d	11.7
Position e	6.8

from QuickField simulations for prototypes utilizing magnets A and B. The table highlights how the magnet geometry and dimensions influence the magnetic restoring force applied to the moving steel ball. In section 3.8, an experimental demonstration illustrating the impact of different magnetic configurations on center frequency and output amplitude is discussed.

Additional simulations, revealed that augmenting the magnet dimensions leads to a heightened

Table 3.4: QuickField simulation results for mechanical force excerted on the moving ball using magnets of different sizes
(Please refer to figures 3.17 and 3.18)

Position	Force Excreted by Magnet A (N)	Force Excreted by Magnet B (N)
a	0.48	0.1
b	1.24	0.78
c	2.39	1.81
d	1.34	0.73
e	0.47	0.11

force applied to the steel ball in motion. As a consequence, this amplifies the magnetic restoring effect, thereby elevating the overall system stiffness (k_{total}) and causing a rise in the center frequency of the FDH. Determining the optimal magnet size hinges upon the vibrational characteristics of the operational surroundings where the FDH is intended for deployment. The outcomes derived from the simulation runs, encompassing the scope of dimensions and the corresponding applied force, are presented within tables 3.5, 3.6, and 3.7. The FDH prototype underwent simulation using QuickField, employing a cuboidal magnet with a matching B-H curve as the component labeled $BY0X08DCS$[80] from K&J Magnetics. The magnet's attributes, namely length, width, and thickness (referred to as height), were systematically altered in each simulation iteration utilizing the subsequent methodology:

- For the initial series of simulations, the width and thickness were held constant at 2 and 0.5 inches, respectively. The length dimension was then varied between 0.1 and 2.5 inches, incremented by 0.3 inches.
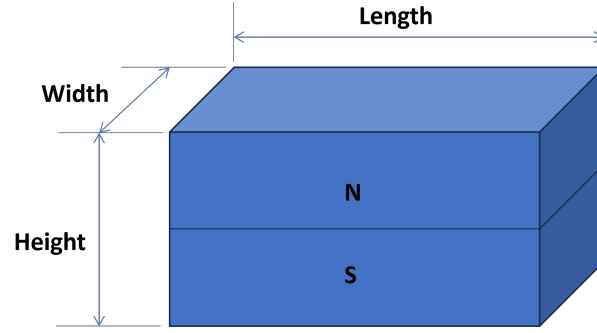
Figure 3.13: Illustration of the designated nomenclature for each facet of the magnet.

- In the subsequent sequence of simulation runs, the length and height were set at 1.2 and 0.5 inches, respectively. The width dimension was modified between 0.1 and 1 inch, with increments of 0.1 inch.

- For the final set of simulation trials, the magnet's length and width were established at 1 and 2 inches, respectively. The height was adjusted within the range of 0.1 to 0.8 inch, with increments of 0.1 inch.

The dimensions selected for the third set of simulations were influenced by identifying prominent peaks observed in the outcomes of the initial and second sets of simulations. It's important to observe that the connection between the dimensions of a cuboidal magnet (length, width, and height) and the force applied to a steel ball in motion is not always a straightforward linear one. When considering the magnet's length, there exists a specific length that yields the highest achievable force. On the other hand, the relationship involving the magnet's width is linear, while the connection between the magnet's height (or thickness) and the applied force follows a semi-exponential pattern.

3.3.5 FDH Equation of Motion

Applying the magnetic restoring force to the mathematical model of the FDH, the equation of motion will be:

$$
\ddot{x}(t) + \left(\frac{c_m + c_e}{m}\right)\dot{x}(t) + \left(\frac{c_3}{m}\right)x(t)^2\dot{x}(t) + \left(\frac{F}{m}\right)
$$
$$
+ \frac{1}{m}(-5.19x^3(t) - 23.05x^2(t) + 14.28x(t) + 2.92) = \ddot{y}(t) \quad (3.13)
$$

Where $\ddot{x}(t)$ is the moving acceleration, c_e and c_m are the electrical and mechanical damping respectively, m is the moving object mass, $\dot{x}(t)$ is the velocity of moving mass, c_3 is the cubic damping resulted from the motion on the track, F is the mechanical restoring force and the cubical term $\frac{1}{m}(-5.19x^3(t) - 23.05x^2(t) + 14.28x(t) + 2.92$ is the magnetic force exerted by the magnet on

Table 3.5: QuickField simulation results showing the exerted force
on the steel ball for different magnet lengths

L (in)	W (in)	H (in)	Force at Position C (N)
0.1	2	0.5	0.09
0.3	2	0.5	0.54
0.6	2	0.5	8.65
0.9	2	0.5	12.14
1	2	0.5	12.27
1.2	2	0.5	10.17
1.5	2	0.5	9.33
1.8	2	0.5	6.401
2	2	0.5	9.49
2.3	2	0.5	7.72
2.5	2	0.5	6.81
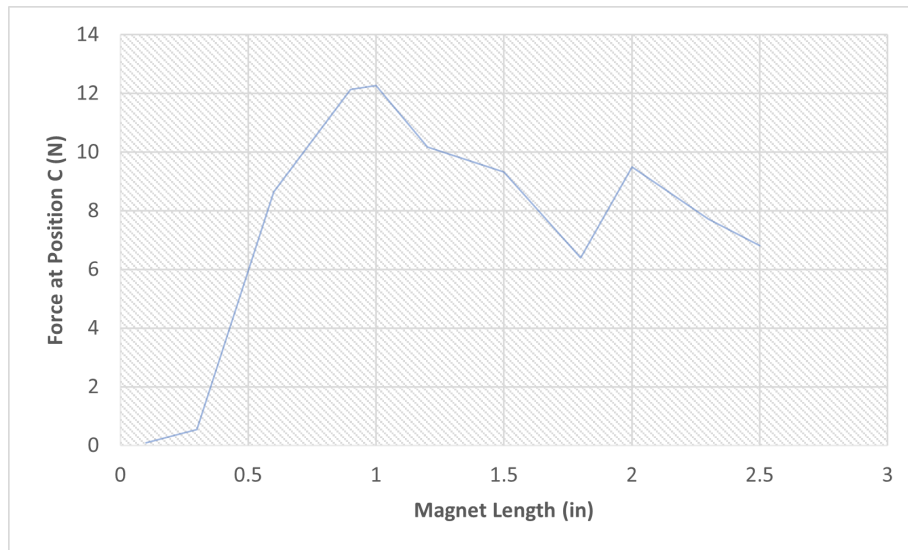
Figure 3.14: QucikField simulation for different magnet lengths versus exerted force on steel ball
at position "C" on the travel-track

the ferromagnetic moving object, a model validation for simulations versus experimental result is
shown in figure 3.19.

The derivation and curve fitting of the magnetic restoring force were carried out using MATLAB.
On the other hand, the simulation of the entire model, including the mechanical oscillator and
magnetic restoring force, was conducted using the Wolfram Mathematica software system, known
for its capabilities in technical computing.

The model shows that the FDH center frequency can be tuned non-mechanically using the mag-
netic restoring force, either by using single or multiple permanent magnet(s) of a different pulling

Table 3.6: QuickField simulation results showing the exerted force
on the steel ball for different magnet widths

W (in)	L (in)	H (in)	Force at Position C (N)
0.1	1.2	0.5	0.54
0.2	1.2	0.5	1.07
0.3	1.2	0.5	1.61
0.4	1.2	0.5	2.15
0.5	1.2	0.5	2.68
0.6	1.2	0.5	3.22
0.7	1.2	0.5	3.76
0.8	1.2	0.5	4.302
0.9	1.2	0.5	4.84
1	1.2	0.5	5.37
2	1.2	0.5	10.75
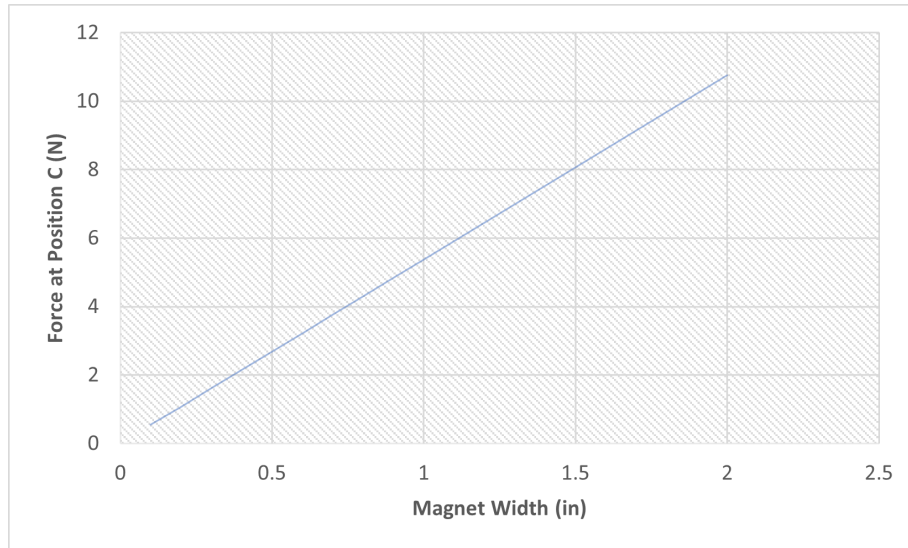
Figure 3.15: QucikField simulation for different magnet widths versus exerted force on steel ball
at position "C" on the travel-track

force, or varying the distance to the ferromagnetic ball motion under external excitation, which allows using small proof-mass and reducing the size of the mechanical oscillator. Model simulation results, shown in figure 3.19, for velocity-frequency shows the identicality in frequency response with the FDH experimental results for voltage-frequency, which validates the reliability of the mathematical model describing it. The oscillations appearing outside the harvesting bandwidth (above 11 Hz) in figure 3.19 are artifacts due design issues, which can result from oscillation of the stationary structures like travel-track (tube) or permanent magnet, this can be eliminated by proper mounting of the stationary components.

Table 3.7: QuickField simulation results showing the exerted force
on the steel ball for different magnet heights

H (in)	L (in)	W (in)	Force at Position C (N)
0.1	1	2	0.25
0.2	1	2	1.26
0.3	1	2	1.96
0.4	1	2	5.22
0.5	1	2	12.27
0.6	1	2	8.73
0.7	1	2	24.41
0.8	1	2	36.79
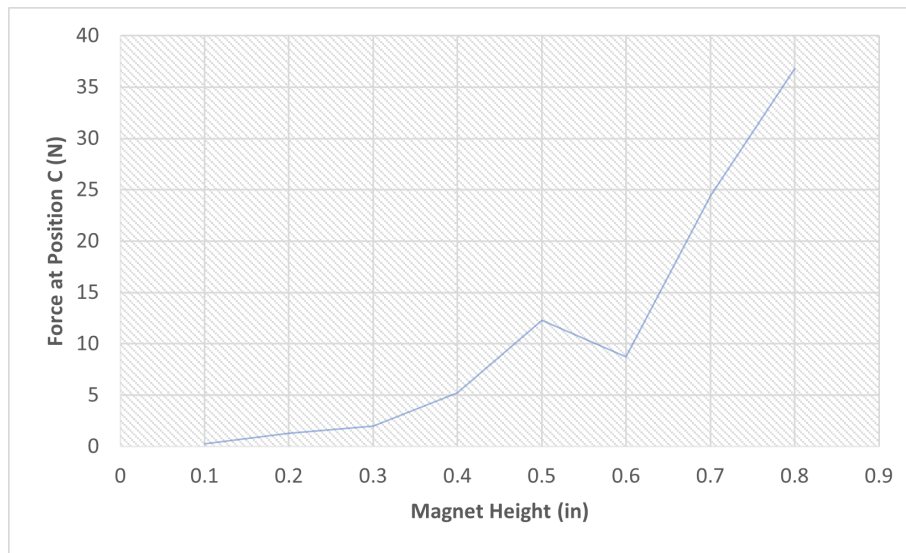
Figure 3.16: QucikField simulation for different magnet heights versus exerted force on steel ball
at position "C" on the travel-track

3.4   Comparison to Other Electromagnetic Energy Harvesters

The mechanical oscillator of the FDH, shown in figure 3.8, comprised of a moving steel ball, travelling along a Teflon-made track. Where the mechanical oscillator is coupled to the magnetic circuit comprised by the permanent magnet and the moving steel ball that resembles a virtual mass-on-spring structure, the magnetic restoring force with respect to distance of the moving steel ball is shown in figure 3.9.In order to compare the FDH to other harvesters from the literature, two main aspects were selected as basis for comparison:

- The harvester uses the same or similar magnetic structure as the FDH.

- The resemblance in mechanical design.
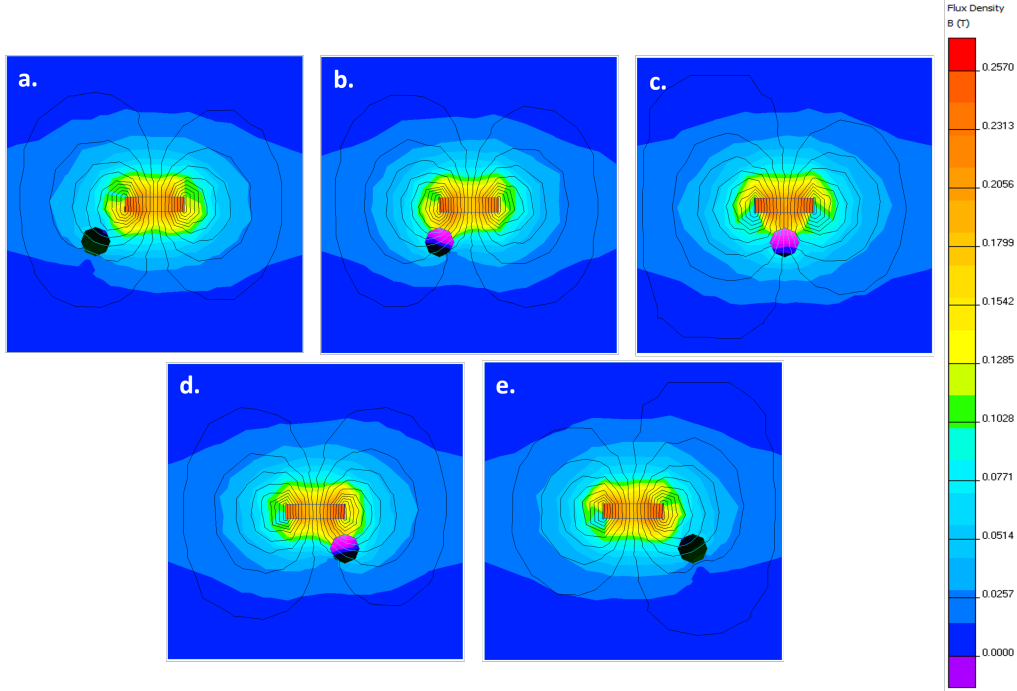
Figure 3.17: Simulated magnetic Flux Density B distribution for magnet A using QuickField

Dallago et. al.[54], Mann et. al.[4] and Haroun et. al.[49] have a similar mechanical structure as the FDH, comprising of a moving object travelling along an enclosed travel track made of plastic or Teflon. While Moss et. al. [64] designs have a similar magnetic induction mechanism using a moving ferromagnetic object to disrupt the magnetic field, using the flux concentration characteristic of steel to create a variable flux and thus inducing current in the nearby coil. In these energy harvesters, the magnetic restoring force is a main factor for magnetic induction and the tuning of harvester's operational parameters (center frequency and harvesting bandwidth). Moss et. al. [62] and Mann et. al. [4] uses the magnetic restoring force to control the velocity of the moving object, which is the main principle for the FDH. The FDH equation of motion is:

$$\ddot{x}(t) + \left(\frac{c_m + c_e}{m}\right)\dot{x}(t) + \left(\frac{c_3}{m}\right)x(t)^2\dot{x}(t) + \left(\frac{F}{m}\right)$$
$$+ \frac{1}{m}(-5.19x^3(t) - 23.05x^2(t) + 14.28x(t) + 2.92) = \ddot{y}(t) \quad (3.14)$$

Where $\ddot{x}(t)$ is the moving acceleration, c_e and c_m are the electrical and mechanical damping respectively, m is the moving object mass, $\dot{x}(t)$ is the velocity of moving mass, c_3 is the cubic damping resulted from the motion on the track, F is the mechanical restoring force and the cubical term $\frac{1}{m}(-5.19x^3(t) - 23.05x^2(t) + 14.28x(t) + 2.92$ is the magnetic force exerted by the magnet on the ferromagnetic moving object. The magnetic restoring force for Mann et. al., shown in figure 3.20 relies on the magnetic flux density, B, at the location of the moving object. The magnetic
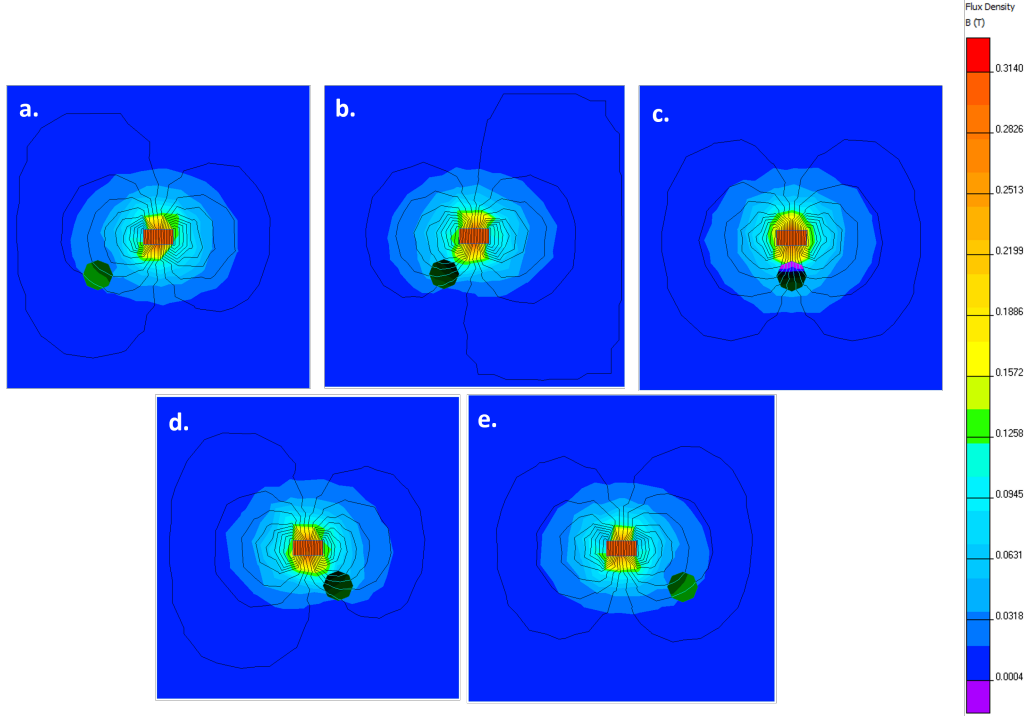
Figure 3.18: Simulated magnetic Flux Density B distribution for magnet B using QuickField

restoring form expression is:

$$F_m(y) = \frac{\mu_o M_c v_c}{2\pi}\left[v_t M_t\left(\frac{3}{(d-y)^4} - \frac{3}{(d-y)^4}\right) - \frac{M_o v_o N}{2}\left(\frac{5y}{(y^2+R_o^2)^{\frac{5}{2}}} - \frac{5y^3}{(y^2+R_o^2)^{\frac{7}{2}}}\right)\right] \quad (3.15)$$

Where μ_o is permeability of free space, v_c, v_t, and v_o are the volume of the center magnet, top & bottom magnets and outer magnets, respectively. M_c, M_t and M_o are the corresponding magnetization amplitudes, d is the half spacing between the top and bottom magnets, and y is the relative position of the center magnet with respect to the device housing. A point to bring to attention that six magnets are required to control the harvester's magnetic restoring force, and thus center frequency, which increases the reliability on the spacing between the magnets and the moving object, increasing the complexity of the design. Where for Moss et. al. harvester, figure 3.21[62], the magnetic restoring force acting on the moving object (steel ball), shown in figure 3.22, shows the magnetic restoring force as function of distance. I would like to bring to the reader's attention a critical design concern, if the excitation amplitude is high enough to overcome the magnetic restoring force, the moving object might fall of the Z-axis central line disrupting the harvesting process, which results in a poor performance under high amplitudes.

Energy harvester by Dallago et. al. [54], shown in figure 3.23, has a simpler design similar to Mann et. al. but without the center magnets used to control the magnetic restoring force. Where it uses the fixed magnets with the same polarity as the moving object at the end of the
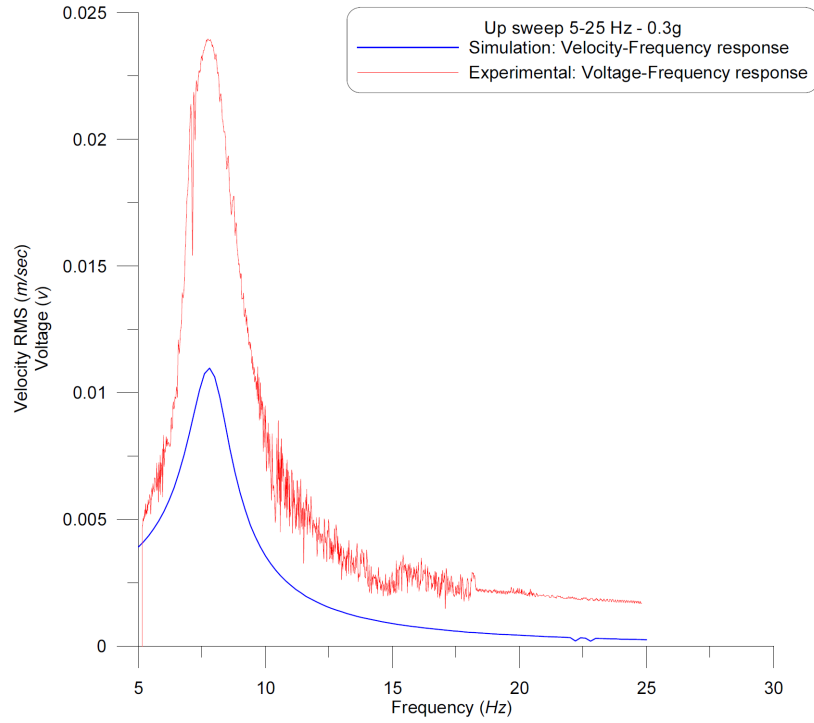
Figure 3.19: Model validation: simulated model velocity-frequency response vs. Experimental voltage frequency response for 5-25 Hz force sweep under excitation of 0.3g
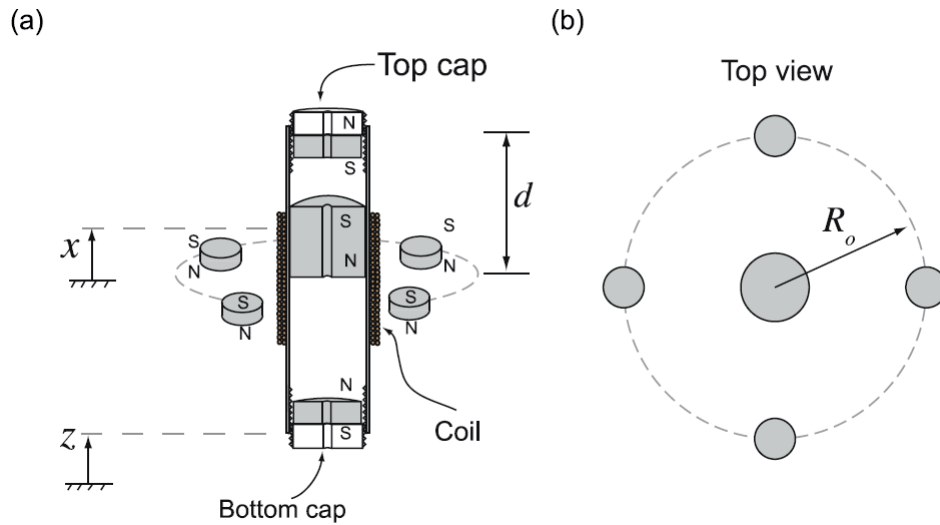
Figure 3.20: Mann et. al. [4] energy harvester with bi-stable potential well

travel track as a replacement for mechanical springs. The moving object, a permanent magnet, is levitating along the travel track between these two end magnets.

The center frequency can be tuned according to the relation:

$$\omega_c = \sqrt{\frac{k}{m}} \tag{3.16}$$
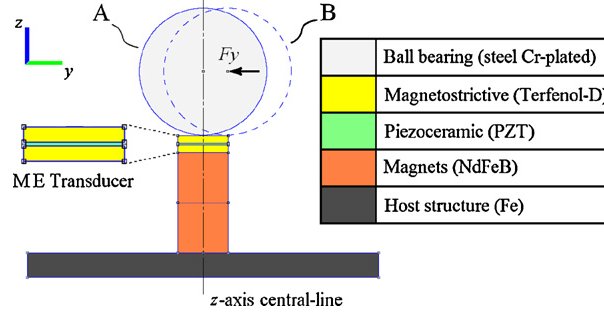
Figure 3.21: Schematic diagram of the bi-axial energy harvester, Moss et. al. [64]
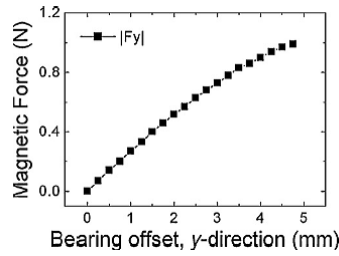
Figure 3.22: Magnetic Restoring Force for Moss et. al.[62] energy harvester acting on the moving object as a function of distance from the harvester's Z-axis central line
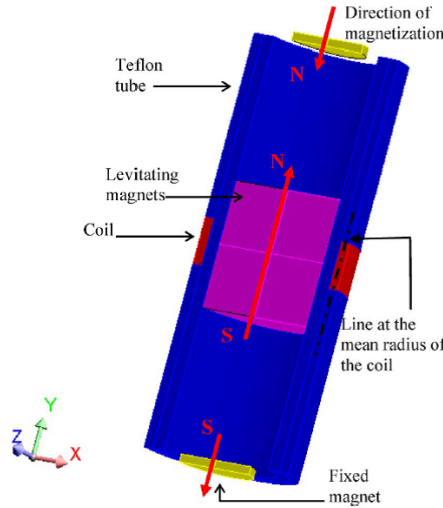
Figure 3.23: Dallago et. al. vibration energy harvester

Where the stiffness, k, is a function of the repulsion magnetic force between the fixed end magnets and the magnetic moving object, which is in turn is function of the position of the moving object and gravity. A simulation of the magnetic repulsion force is show in figure 3.24. The acceleration of the moving object is:

$$\ddot{x}(t) = \frac{F_{mag}(x)}{m} - \frac{b}{m}\dot{x}(t) - \ddot{u}(t) - g \tag{3.17}$$

Where $\ddot{x}$ is the acceleration of the moving object, F_{mag} is the magnetic repulsion force, m is
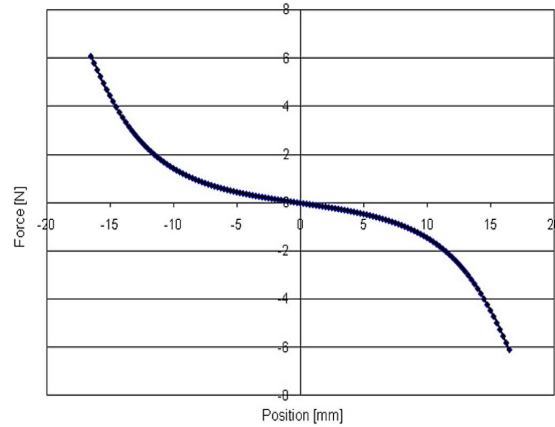
Figure 3.24: Magnetic repulsion force for Dallago et. al. energy harvester simulated in Flux2D

the mass of the moving object, $\ddot{u}$ is the base excitation, $\dot{x}$ is the moving object velocity, b is the damping factor, and g is the gravitational acceleration. A major concern that arises for Dallago et. al. design is the effect of impact on the fixed end magnets and the moving object at high amplitude base excitations, when the external forcing overcomes the repulsion force resulting in strong impacts that can break the magnets, since most of magnetic materials are brittle. Another concern that is less likely but probable is the "asymmetry", if the fixed end magnets aren't identical then the repulsion force will differ resulting in a bilinear oscillatory behavior, which affects the center frequency. Moss et. al. [62] and Haroun et. al. [49] energy harvesters, shown in figures 3.25 and 3.26, respectively, have similar oscillator design of a moving object traveling along a confined track, where the source of magnetic field is the mechanical oscillator itself. And hence the moving object is made of a magnetic material; it creates a counter magnetic field and an opposing force in the coil structure around the travel track. The magnetic restoring force for Haroun et. al. energy harvester is shown in figure 3.27. The center frequency of the two energy harvesters mostly is a function of the moving object mass, making it dependant on this mechanical design parameter.

3.5   Experimental Results

This chapter presents a thorough analysis of the experimental results for different coil and magnetic configurations is presented. A set of experiments were designed and conducted to investigate the system dynamics and the correlation between the different parameters governing the system. The experimental results were analyzed to characterize the system and create a descriptive model to be used for designing an energy harvester and optimize the design to maximize its energy efficiency and harvesting capability under different operating conditions.
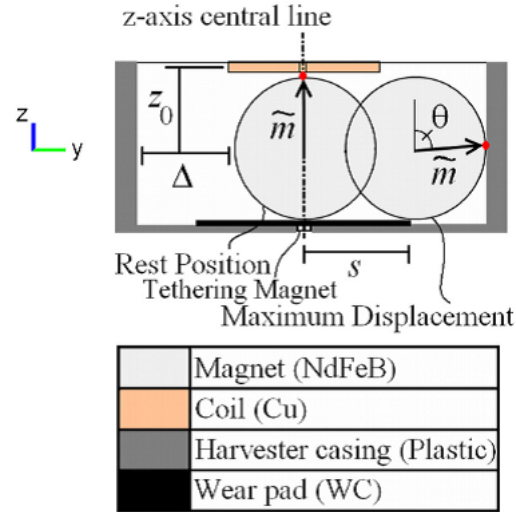
Figure 3.25: Schematic diagram of the hybrid rotary-translational vibration energy harvester by Moss et. al.[62]
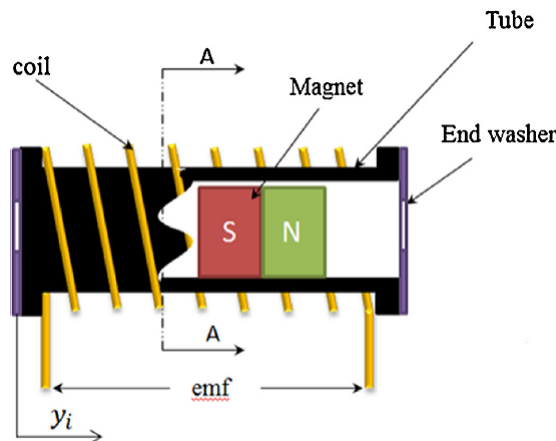
Figure 3.26: Schematic of micro-electromagnetic generator based on free/impact motion by Haroun et. al.[49]

3.6   Single Magnet - Centered Coil FDH

The basic FDH design, shown in figure 3.1, consist of four components. First, a travel track along which the moving components are displaced, the travel track is made of Teflon.

A free-moving ferromagnetic material ball is placed within the travel track. The ball materials used were steel and nickel coated steel. A coil is wound around the center of the travel track. Finally, a permanent magnet is placed at top of the travel track at a distance of 13.6 mm. Table 3.8 lists different parameters of the FDH. This prototype was built to study the harvester dynamics and identify all parameters that affect its behavior, with minimal influence from the counter magnetic field induced in the coil while operating, or complicated magnetic field structure
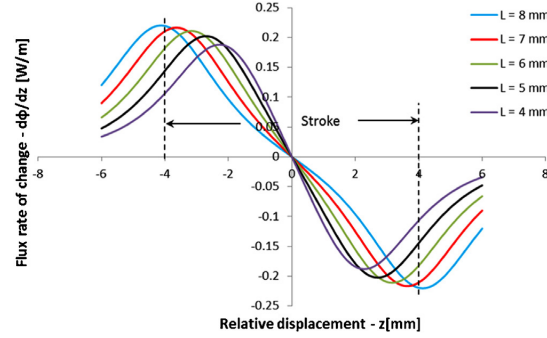
Figure 3.27: "Variation of the predicted flux rate of change with respect to the relativedisplacement $(d\phi/dz)$ with the magnet position within the coil (z) for different coillengths (coil length of 8 mm is used in the model prediction of the case study)", Haroun et. al. [49]
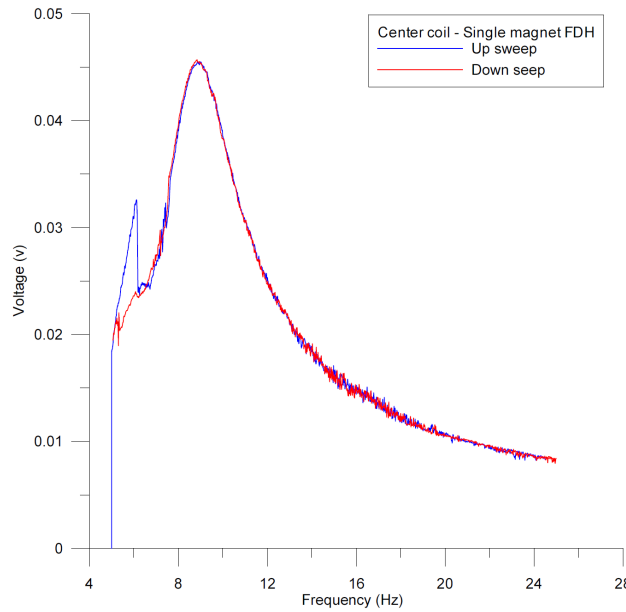
Figure 3.28: FDH Voltage-Frequency response under 0.9 g external excitation

when using multiple magnets.

The voltage-frequency response in figure 3.28 exhibits softening nonlinearity resulting from the impact of the steel ball with the mechanical end-springs, and magnetic restoring force introduced by the top magnet, where the steel ball and the top magnet assembly form a tension, magnetic mass-on-spring structure, adding more stiffness to the dynamics of the FDH.

It can be deduced from the experimental observations that the impact of the steel ball on the end-springs does not apply at all excitation frequencies. It is more likely to have significant occurrences at frequencies lower than the resonance frequency at 9.57 Hz. It decreases at resonance then disappears completely once the excitation frequency reaches the upper limit of the bandwidth. At this point the magnetic restoring force becomes higher in magnitude than the external excitation, which forces the steel ball to oscillate only in the middle section of the travel track, reducing the
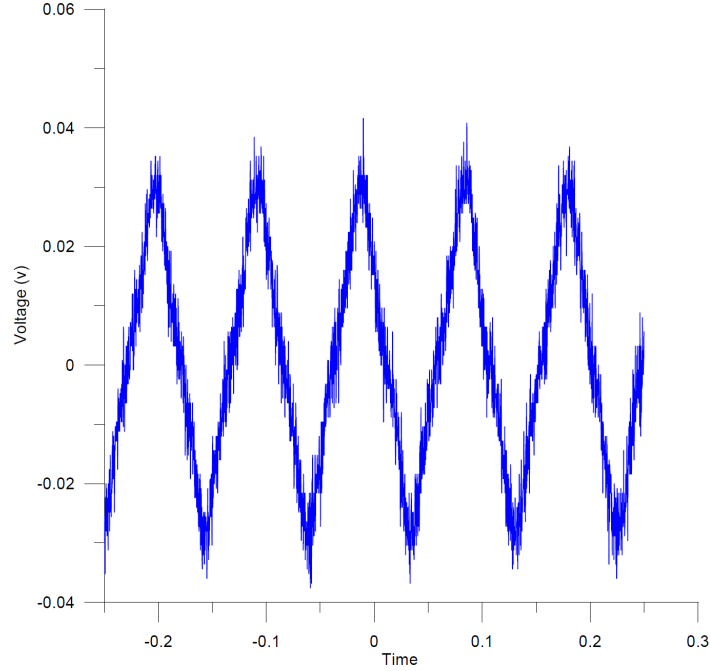
Figure 3.29: FDH Voltage-Frequency response under 0.9 g external excitation

Table 3.8: Centered Coil - Single Magnet FDH Parameters

Parameter	Value
End springs stiffness k [N/m]	2529.1
Residual flux density B_r [Gauss]	13200
Number of coil turns	711
Ball diameter: D_b [mm]	13.05
Ball mass: m [gr]	8.9
Top magnet type [80]	NdFeB, Grade N42
Top magnet dimensions [mm]	50.8 x 25.4 x 12.7

oscillation of the steel ball to the minimum. The sharp drop and rise in voltage observed between 6 and 9 Hz is a result of a "super-harmonic resonance".

Furthermore, to investigate the mechanical impact on the end-springs and its relationship to the output voltage, the end-springs were replaced with shock sensors to measure the impacts on the walls, a hall-effect sensor was placed below the middle section the travel track to measure magnetic field in real-time, and the experiment setup is shown in figure 3.12. A display of the steel ball motion interpreted from voltage versus impacts on both ends of the travel track is shown in figure 3.12.
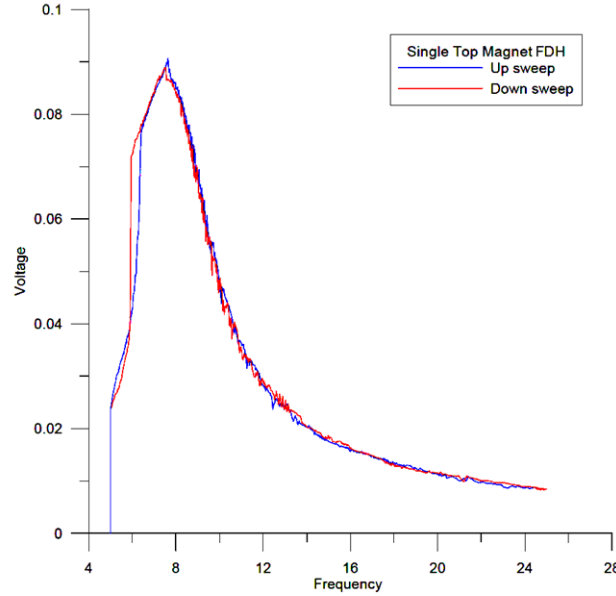
Figure 3.30: V-F response for 960 turns coil

3.7   Different Coil Configurations

Different coil structures induce different counter magnetic field distributions, and this can be used to increase the output power, as demonstrated in the prototypes covered in this section. A coil with 960 turns exhibited a drop in the center frequency down to 7.64 Hz indicating an increased stiffness, which results from the counter magnetic field generated in the coil. Similar response was observed using a coil with 2580 turns, where the center frequency dropped to 7.19 Hz. Moreover, both the stiffness parameters as well as the damping increased. The $3dB$ bandwidth kept increasing with the increase in number of coil turns, which confirms the change in dynamics due to the coil counter magnetic field, different coil configurations and results are listed in table 3.9. In one configuration, in which the Teflon travel track was replaced with copper and using a coil with 2580 turns, the center frequency increased to 8.04 Hz while the $3dB$ bandwidth decreased and bandwidth decreased to 3.03 Hz. These results indicate a decrease in the counter magnetic field. From table 3.9, the system dynamics don't depend solely on the mechanical design and

Table 3.9: Different Coil Configurations (all tests conducted under 0.9 g excitation)

Coil configuration	# of turns	Inductance (mH)	Center frequency (Hz)	3dB bandwidth (Hz)	Q-factor
Center coil (original design)	711	0.18	9.57	2.72	3.51
Fully covered track	960	3.4	7.64	2.89	2.64
Fully covered track	2580	21.18	7.19	3.32	2.16
Fully covered track, Copper track	2580	12.04	8.04	3.03	2.65

magnetic circuit of the oscillator, but the electromagnetic structure as well represented in the coil structure, which allows using the coil configuration as a tuning tool for the harvester's center
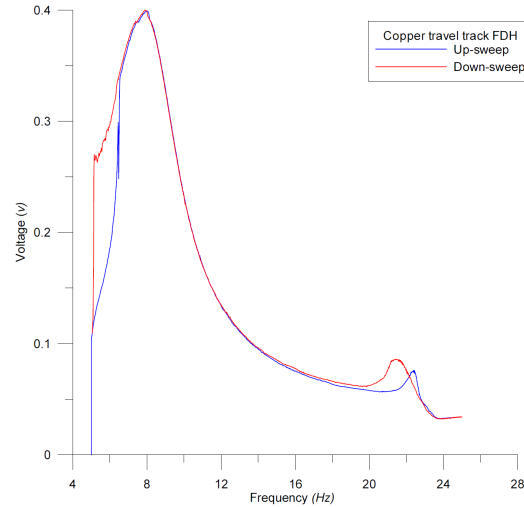
Figure 3.31: V-F response for 2580 turns coil with copper travel track

frequency and bandwidth to match operating environment spectrum.

3.8   Prototypes with Different Magnetic Configurations

The frequency response of an earlier version of the FDH [32] was compared to the modified prototype shown in figure **??**. The earlier FDH design has four magnets mounted on the sides of the housing around the track mid-section. It was obvious that the magnetic field configuration affects the system dynamics in terms stiffness, damping and nonlinearity. For a deeper insight, an expanded set of experiments on FDHs with the following magnetic configurations were conducted:

- Four small magnets opposing each other, figure 3.32 *i*.

- Top big magnet and two small side magnets, figure 3.32 *ii*).

- Single top magnet, figure 3.32 *iii*.

- Single top magnet with a steel rectangle on the bottom, figure 3.32 *iv*.

- Single top magnet with a U-shape steel cover, figure 3.32 *v*.

- Single top magnet with a reversed U-shape steel cover, figure 3.32 *vi*.

- Single top magnet with a U-shape steel cage, figure 3.32 *vii*.

- Four steel opposing magnets inside a steel cage, figure 3.32 *viii*.

- Four medium size magnets mounted on the top and bottom sides, figure 3.32 *ix*.

- Six medium size magnets mounted on the four sides, figure 3.32 *x*.

47
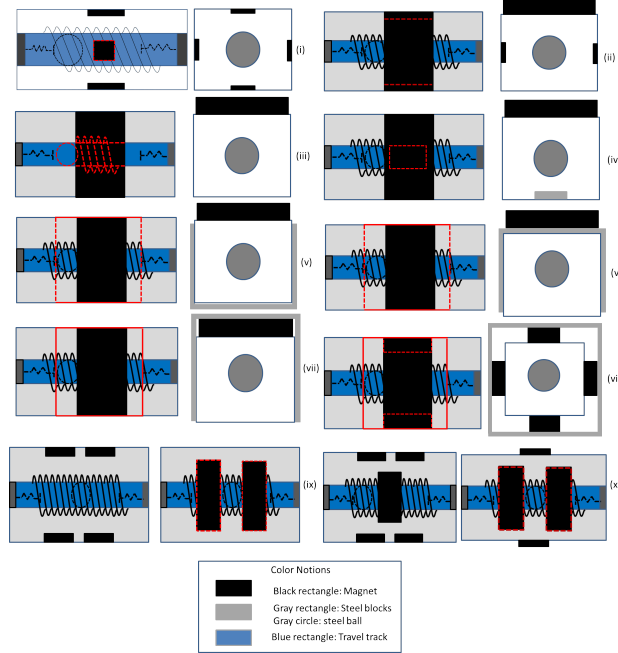
Figure 3.32: FDH prototypes with different magnetic configurations

Table 3.10: Results of Different Magnetic Configurations (refer to figure 3.32)

Magnetic Configuration	Center Frequency (Hz)	3dB Bandwidth (Hz)	Maximum voltage (mv)	Q-factor
Configuration i	11.95	5.8	26	2.06
Configuration ii	8.74	2.62	101	3.33
Configuration iii	9.57	2.72	28.2	3.51
Configuration iv	8.5	2.5	95	3.4
Configuration v	7.63	2.93	82.7	2.6
Configuration vi	6.54	1.92	60.4	3.4
Configuration vi	8.53	2.85	98.32	2.99
Configuration $viii$	6.72	1.32	24.37	5.09
Configuration ix	12.72	2.66	25.9	4.78
Configuration x	12.6	2.52	25.11	5
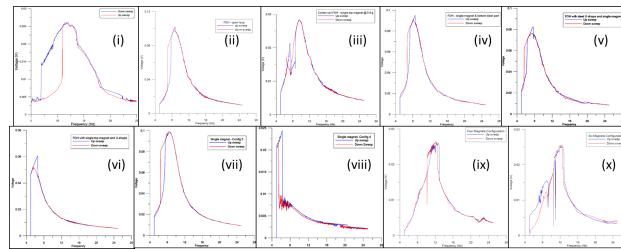
Figure 3.33: V-F response for different magnetic configurations

The voltage-frequency response for each configuration, shown in figure 3.33, confirmed that system dynamics -observed from the changes in center frequency and $3dB$ bandwidth- are function of the magnetic field configuration, however, the output power for some configurations is significantly low, but they are beneficial in the analysis and modeling of the magnetic restoring force, and the

Figure 3.34: Image depicting an upsized iteration of the FDH prototype (left) alongside the original model (right)

uses of FDH as a sensor and actuator.

3.9   Scaled-Up FDH Prototype

To assess whether there's a correlation between the size of the FDH and the generated power increase, a larger prototype was created and subjected to testing. The expanded prototype, shown in figures 3.34 and 3.35, boasts dimensions of $7.5 \times 4.3 \times 2.2$ inches, as well as a steel ball with a diameter of 1 inch (25.4 mm), having a weight of 66 grams, which exceeds more than twice the volume of the initial prototype introduced earlier in this chapter.

Regrettably, the test outcomes lacked decisiveness owing to the constraints of the electrodynamic shaker employed for testing, which could not produce vibrations below 4 Hz for this specific prototype. The highest point of the output voltage was noticed at 4 Hz, shown in figure 3.36, indicating the prototype's capacity to resonate at lower frequencies, rendering it suitable for the range of frequencies associated with human motion.
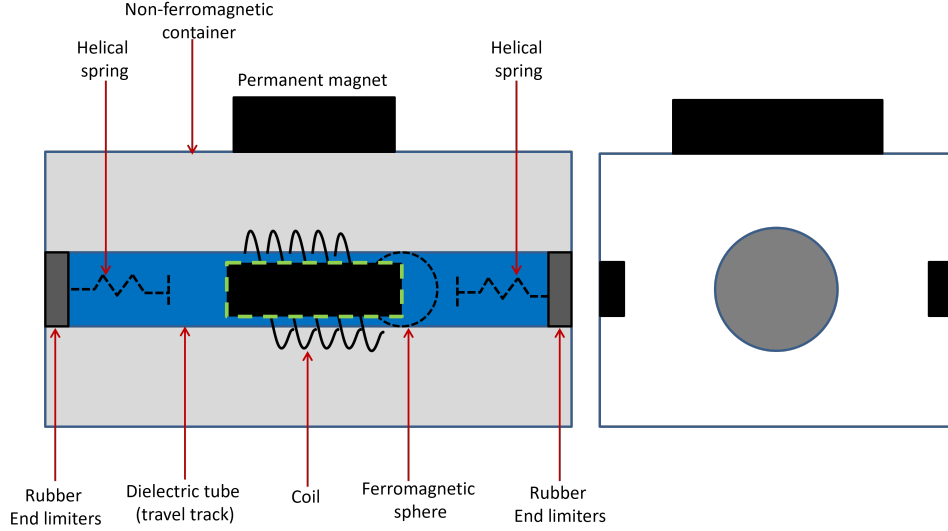
Figure 3.35: Schematic of up-scaled FDH rear view (right) and side view (left)

3.10   Output Power

The power generated in a magnetic-induction generator from a sinusoidal input displacement is governed by [65]:

$$P = \frac{m\eta_e A_o^2 \left(\frac{\omega}{\omega_n}\right)^3 \omega^3}{\left[1 - \left(\frac{\omega}{\omega_n}\right)^2\right]^2 + \left[2\eta\frac{\omega}{\omega_n}\right]^2} \tag{3.18}$$

Where m is the proof mass of the oscillator, A_o is the excitation amplitude, η and η_e are the total and electrical damping factors, respectively, ω and ω_n are the operating and natural frequencies, respectively. The maximum power transfer occur at resonance when the operating frequency ω equals to the VEH natural frequency ω_n, so maximum power will be [65]:

$$P_{max} = \frac{m\eta_e A_o^2 \omega_n^3}{4\eta^2} \tag{3.19}$$

The power generated by the FDH was measured across a set of resistive loads, though a resistive load increases the electric damping factor η_e, it doesn't affect the FDH dynamic response qualitatively in terms of nonlinearity, center frequency, and $3dB$ bandwidth as shown in figure 3.37, where a slight shift in the center frequency of the track-covered-by-coil FDH as load increases. As shown in table 3.14; where maximum power of 154.6 μW was generated through 5.6 Ω load resistance for a coil with 960 turns and 10.4 Ω resistance.
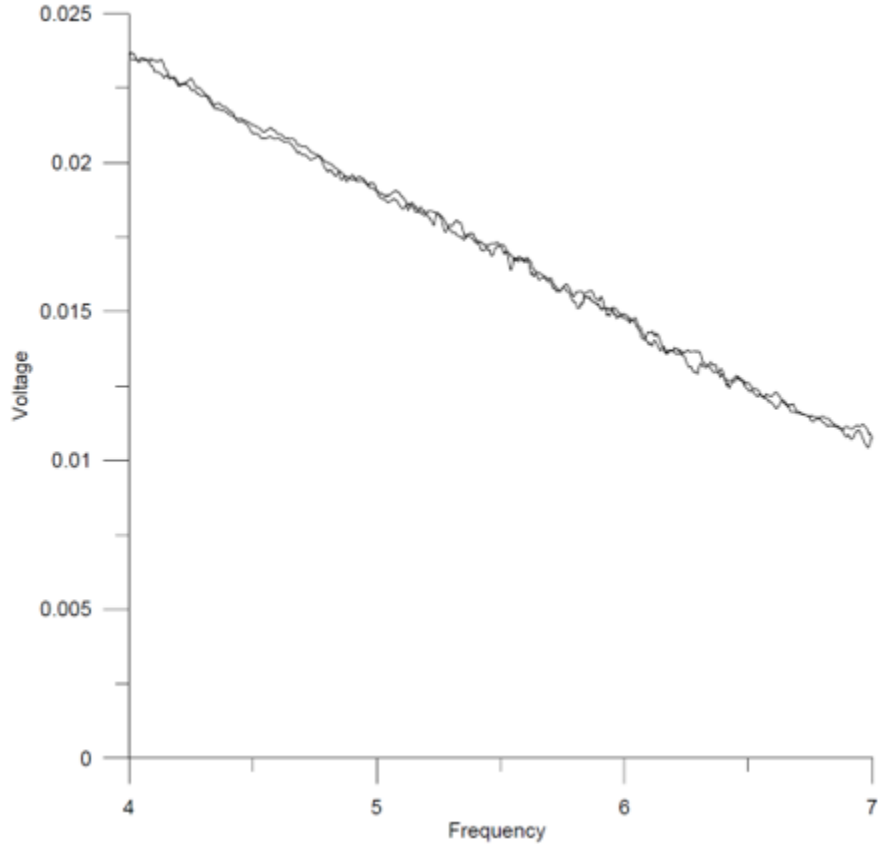
Figure 3.36: Voltage-Freuqneyc response for the upsized FDH prototype

Table 3.11: Measured Output Power for Different Resistive Loads
(the overall volume of the FDH is taken into consideration, and not just the proof-mass)

Resistance (Ω)	Voltage (mV)	Current (mA)	Generated Power (μW)	Power Density per entire volume ($\mu W/cm^3$)	Power Density per active volume($\mu W/cm^3$)
0	2.12	6.7	14.2	0.07	1.298
5.6	32.9	4.7	154.63	0.77	14.134
8.6	46.3	2.4	111.12	0.55	10.157
22.6	72.8	0.76	55.3	0.27	5.055
100	100.1	0.76	76.07	0.38	6.953
1000	114	0.086	9.8	0.048	0.896

3.10.1   Comparing the FDH Performance to other EVEHs

In this section, the performance of the FDH is compared with other electromagnetic vibration energy harvesters (EVEHs) from the literature from two aspects: power density and proof-mass. The FDH's power density at resonance for different resistive loads, reported previously in table 3.14, when be compared to other EVEHs of a similar mechanical design that use moving/stationary coil and permanent magnet structure, shown in table 3.12, shows that the FDH power density is not too high, yet, the comparison does not take into consideration:

- FDH prototypes with different magnetic configuration.
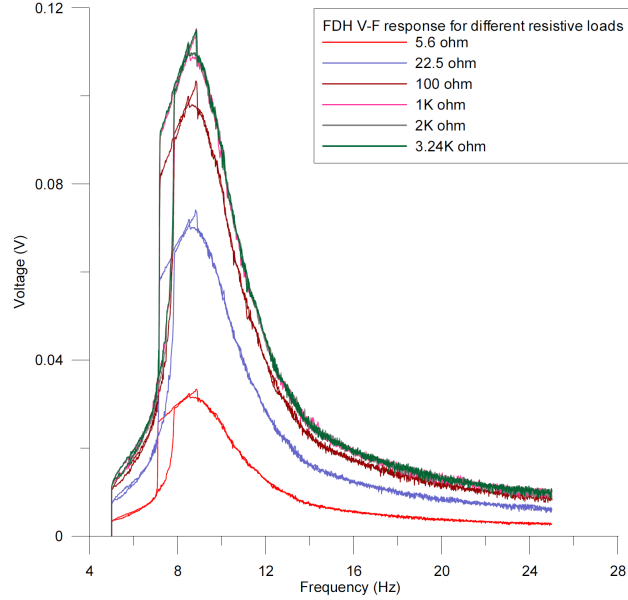
Figure 3.37: V-F response for different resistive loads

- FDH prototyoes with different coil turns.

- Harvesting at multiple frequencies using different types load, which is discussed further in the next section.

Table 3.12: List of power densities for different vibration energy harvesters with similar mechanical design to the FDH

Vibration Energy Harvester Design	Power Density	Unit
Halim et. al. [45]	15.4	$\mu W/cm^3$
Haroun et. al. [49]	179.82	$\mu W/cm^3$
Cao et. al. [56]	0.41	mW/cm^3
Choi et. al [48]	0.78	mW/cm^3
Fondevilla et. al. [60]	1.5	mW/cm^3
Moss et. al. [61]	3.4	mW/cm^3

As shown previously, the FDH is capable of effectively harvesting low frequency vibration using small proof-mass, only $9.8grams$ compared to other vibration energy harvesters of similar design. Table 3.13 compares the FDH's proof-mass to select electromagnetic vibration energy harvesters (EVEH) from the literature with similar design and operate in the same frequency band as the FDH.

Table 3.13: A comparison of proof-mass for different VEHs

Energy Harvester	Proof-mass ($grams$)
Moss et. al.[61]	64.3
Fan et. al.[68][69]	33
Lee et. al.[70]	30
Fu et. al.[71]	29.4
FDH [34]	9.8

3.11   The influence of the load type on center frequency tuning [35]

Experiments conducted on earlier prototypes of the FDH[32] with purely capacitive loads showed a significantly different voltage-frequency response in comparison with purely resistive loads and open-loop, in which no loads were connected to the output. The observed changes in the center frequency established grounds to test the FDH with an in-series resistor-capacitor complex load structure to study the effect of added stiffness and damping to the system due to the load resistance and capacitance, and how the load can be used to tune the center frequency without any mechanical or magnetic pre-tuning such as changing the proof-mass or the magnetic field intensity [30][31]. The experimental setup to test the FDH with in-series RC load is shown in figures 3.39 and 3.40. A basic demonstration setup, shown in Figure 3.41, was used to visually demonstrate the generated power using a low-power light emitting diode (LED) and a 1:10 step-up transformer. All experiments were conducted with a sinusoidal excitation in the frequency range of 5-25 Hz, with sweep rate of 5 Hz/min and amplitude of $0.9g$ ($1g = 9.81\ m/s^2$) to mimic the amplitude of human walking. All experiments were repeated multiple times to ensure the validity and reproducibility of the results.

Experimental results exhibited that using a load consisting of in-series resistor-capacitor pair with the output of the FDH, as shown in the schematic in figure 3.38, affects the center frequency, which is a result of increased stiffness introduced by the capacitance component of the load, to the FDH system. Figure 3.42 and table 3.15 demonstrate the measured voltage-frequency response and center frequency of the FDH for different in-series RC loads, respectively. The governing equation for the center frequency as a function of stiffness and damping for a mass-on-spring oscillator are [65]:

$$\omega_n = \sqrt{\frac{k}{m}} \tag{3.20}$$

And [65]:

$$\eta = \frac{B_m Z_L + (Bl)^2}{2Z_L \sqrt{mk}} = \frac{B_m}{2\omega_n m} + \frac{Bl^2/Z_L}{2\omega_n m} = \eta_m + \eta_e \tag{3.21}$$
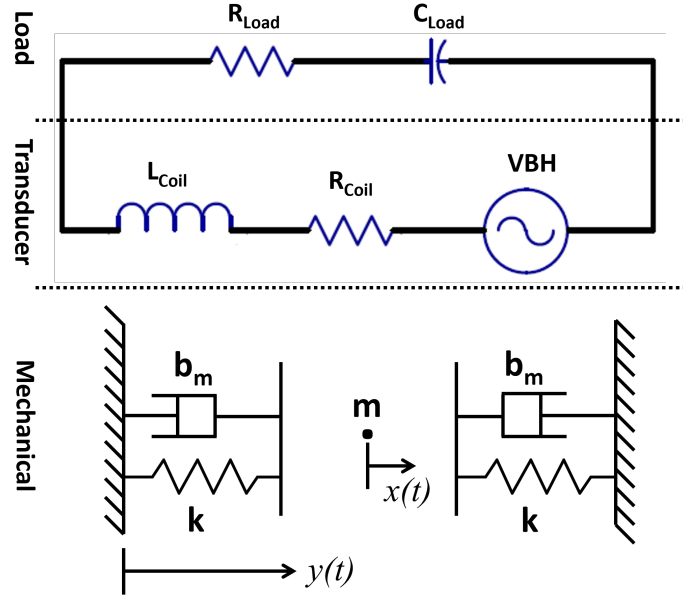
Figure 3.38: Representation of the FDH, with complex RC load impedance, where L_{coil}, R_{coil}, R_{Load}, C_{Load}, m, k, and b_m are the harvester's coil inductance, coil resistance, load resistance, load capacitance, moving proof-mass, mechanical stiffness, and mechanical damping, respectively

where ω_n is the natural frequency, k is the total stiffness of the oscillator, and m is the proof-mass of the moving object. η, η_m, and η_e are the total, mechanical and electrical damping factors, respectively. B_m is the energy extraction damping factor, B is the magnetic flux density, l is the coil length, and $|Z_L|$ is the magnitude of load impedance. For a complex RC load the magnitude is:

$$|Z_L| = \sqrt{R_L^2 + |X_c|^2} \tag{3.22}$$

where R_L is the resistive component and $|X_c|$ is the magnitude of the capacitive reactance component of the load impedance. Where the capacitive reactance is a function of capacitance and generated EMF frequency:

$$X_c = \frac{1}{\omega_c C} = \frac{1}{2\pi f_c C} \tag{3.23}$$

where ω is the center angular frequency of the voltage across the capacitor, which can be substituted with the term $2\pi f_c$, where f_c is the center frequency in $Hertz$, and C is the capacitance in $Farad$. Experiments conducted with purely resistive and complex RC loads (as listed in Tables 3.14 and 3.15) demonstrated that the center frequency changed, indicating a change in system stiffness k. The proof mass was kept constant across all experiments to emphasize that the change in center frequency was due solely to the change in the system's stiffness. To further validate this observation, the FDH was tested with complex loads of different capacitance values, while keeping the value of the resistive component unchanged. Results showed a variation in the center

frequency of 0.33 Hz for capacitance values between 10 and 25100 μF. Furthermore, comparing test results conducted with purely resistive load with tests conducted with in-series RC load that uses the same resistance value; the center frequency has dropped by 0.4-0.65Hz when capacitance is added, indicating a reduction in system stiffness k. Experimental results for RC load and purely resistive load versus center frequency are shown in tables 3.15 and 3.14, respectively. [ht]   To
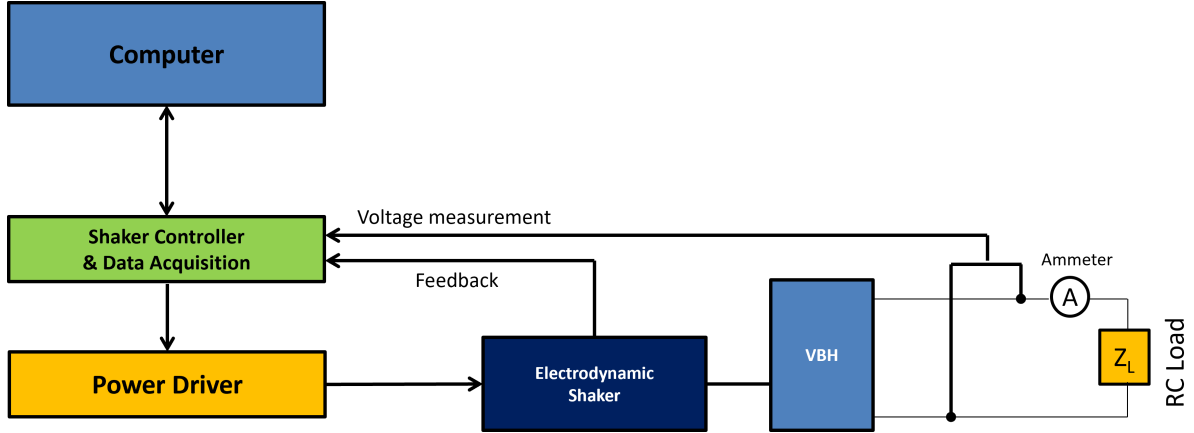
Figure 3.39: A schematic of the experimental setup of the FDH with in-series RC load

Table 3.14: FDH center frequency for purely resistance loads

Resistance (Ω)	Center frequency (Hz)
0	8.75
5	8.84
8.6	8.86
22.6	8.81
100	8.83
1000	8.84
2000	8.79
3240	8.84
9000	8.66
Open loop (no load)	8.18

test the FDH in a real-world scenario where DC output power, and not AC, is required to power up different electronic devices, The FDH output was connected to a step-up transformer with primary-to-secondary coil turns ratio of 1:10, followed by a Schottky-based full-wave rectifier and ripple filtering capacitor to provide a complete power unit design. This power unit design is meant to resolve two main challenges:

- Output voltage amplitude is too low for most electronic devices to operate on.

- Generic silicon diode-based full-wave rectifiers cannot rectify AC signals smaller than 700-
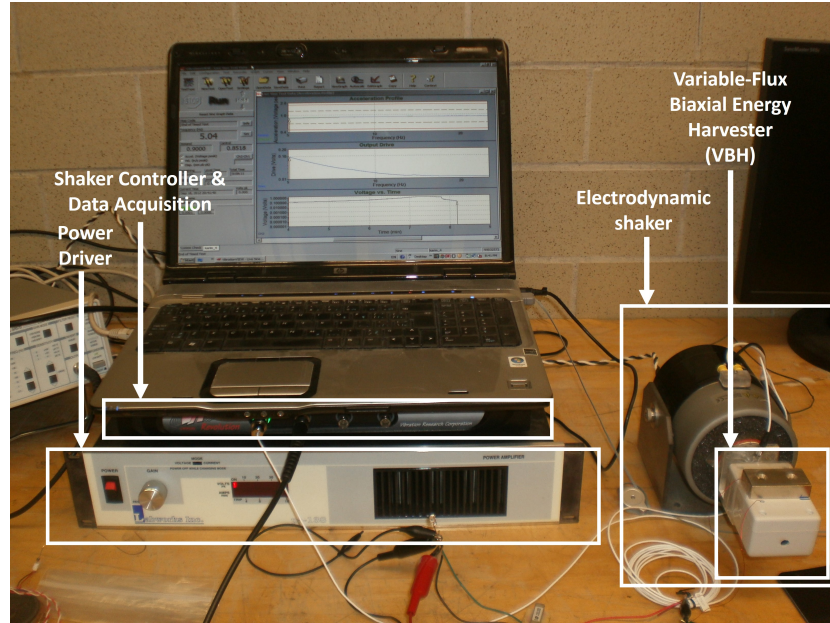
Figure 3.40: A Picture of the experimental setup of the FDH
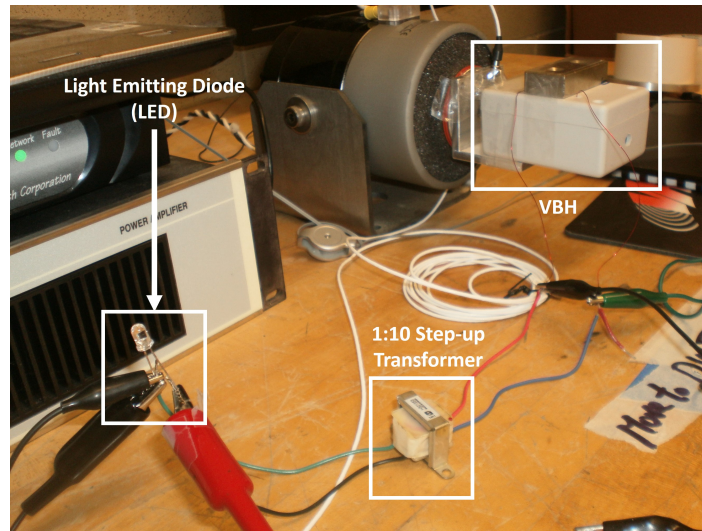
Figure 3.41: A Picture of a simple demonstrator using the FDH with a step-up transformer and Light Emitting Diode (LED)

$800 \ mV$.

A Schottky diode-based full-wave rectifier was used for its low forward-voltage (150-450 mV) compared to generic silicon diode rectifiers, and the ripple filter capacitor at the output stage is added to smooth the output signal and eliminate ripples. A schematic of the power unit is shown in figure 3.43. Experiments showed that the filter capacitor adds extra stiffness to the system resulting in a higher center frequency f_c with the increase of the capacitance value. This confirms the previously discussed conclusion of the directly proportional effect of output capacitance on

Table 3.15: FDH center frequency for different RC network loads

Resistance (Ω)	Capacitance (μF)	Center Frequency (Hz)	Maximum Voltage (mV)	RMS Current (mA)	Reactive Power $(S = I^2 X_c)$ μVA	Real Power $(P = I^2 R)$ μW	Bandwidth (Hz)	Total Stiffness $(k = \omega^2 m)$	Power Density per entire volume $(\mu W/cm^3)$
5	10	8.2	104.3	0.18	62.86	0.16	2.62	23.644	0.00081
5	100	8.22	102.8	0.627	76.09	1.97	2.72	23.760	0.009828225
5	670	8.2	88.2	2.5	180.98	31.25	2.55	23.644	0.15625
5	820	8.45	84.7	3.1	220.65	48.05	2.51	25.108	0.24025
5	1000	8.23	79.8	3	173.98	45.00	2.52	23.818	0.225
5	1200	8.15	73.7	3.2	166.57	51.20	2.54	23.357	0.256
5	7700	8.45	34.39	4.6	51.74	105.80	2.65	25.108	0.529
5	25100	8.11	29.8	4	12.50	80.00	2.67	23.128	0.4
8.4	1000	8.44	81.1	2.8	147.78	65.86	2.52	25.049	0.32928
11	200	8.2	101.24	1	97.01	11.00	2.66	23.644	0.055
11	470	8.23	91.96	1.8	133.26	35.64	2.57	23.818	0.1782
11	680	8.23	84.41	2.3	150.38	58.19	2.57	23.818	0.29095
11	820	8.47	81.42	2.6	154.84	74.36	2.51	25.227	0.3718
11	1000	8.2	77.57	2.6	131.15	74.36	2.51	23.644	0.3718
11	2200	8.4	60.89	3.2	88.15	112.64	2.53	24.812	0.5632
11	3100	8.4	55.84	3.3	66.53	119.79	2.54	24.812	0.59895
11	4400	8.64	52.5	3.4	48.38	127.16	2.646	26.250	0.6358
11	5400	8.46	52.09	3.4	40.26	127.16	2.61	25.167	0.6358
11	22000	8.72	50	3.4	9.59	127.16	2.59	26.738	0.6358
15	100	8.15	86.79	0.37	26.72	2.05	2.57	23.357	0.0102675
16	2200	8.54	60.69	2.7	61.73	116.64	2.6	25.646	0.5832
16	4400	8.52	62.29	2.8	33.27	125.44	2.55	25.526	0.6272
16	22000	8.54	60.69	2.8	6.64	125.44	2.59	25.646	0.6272
22.5	0.1	8.23	102.41	0.0022	0.94	0.00	2.69	23.818	5.445E-07
22.5	10	8.18	103.36	0.071	9.80	0.11	2.66	23.529	0.000567113
22.5	100	8.21	85.59	0.355	24.42	2.84	2.57	23.702	0.014177813
22.5	1000	8.25	23.07	0.564	6.13	7.16	2.55	23.934	0.0357858
100	10	8.23	101.8	0.065	8.17	0.42	2.66	23.818	0.0021125
100	1000	8.07	48.7	0.365	2.63	13.32	2.66	22.901	0.0666125
1000	10	8.14	100.7	0.04	3.13	1.60	2.67	23.300	0.008
1000	1000	8.25	93.5	0.07	0.09	4.90	2.62	23.934	0.0245

the FDH's total stiffness. Figures 3.44 and 3.45 show the V-F response of the power unit for a frequency sweep 5-25 Hz at 0.9 g excitation, a comparison of different filter capacitor values versus center frequency is shown in table 3.16. The hysteresis in $V - F$ response might catch the attention of the reader, early conclusion explains such hysteresis is due to additional nonlinear components to the output load network represented by the step-up transformer and Schottky diode full-wave rectifier, however, it is not the scope of interest of this dissertation.

Table 3.16: A center frequency (f_c) comparison for the PSU up- and down-sweeps using 10, 100 and 1000 μF filter capacitors for 100 Ω resistive load

Filter capacitor value (μF)	f_c (up-sweep) (Hz)	f_c (down -sweep) (Hz)	Max. voltage in up-sweep cycle (mV)	Max. voltage in down-sweep cycle (mV)
10	8.52	8.37	907	894
100	8.72	8.17	991	969
1000	9.2	7.83	661	712
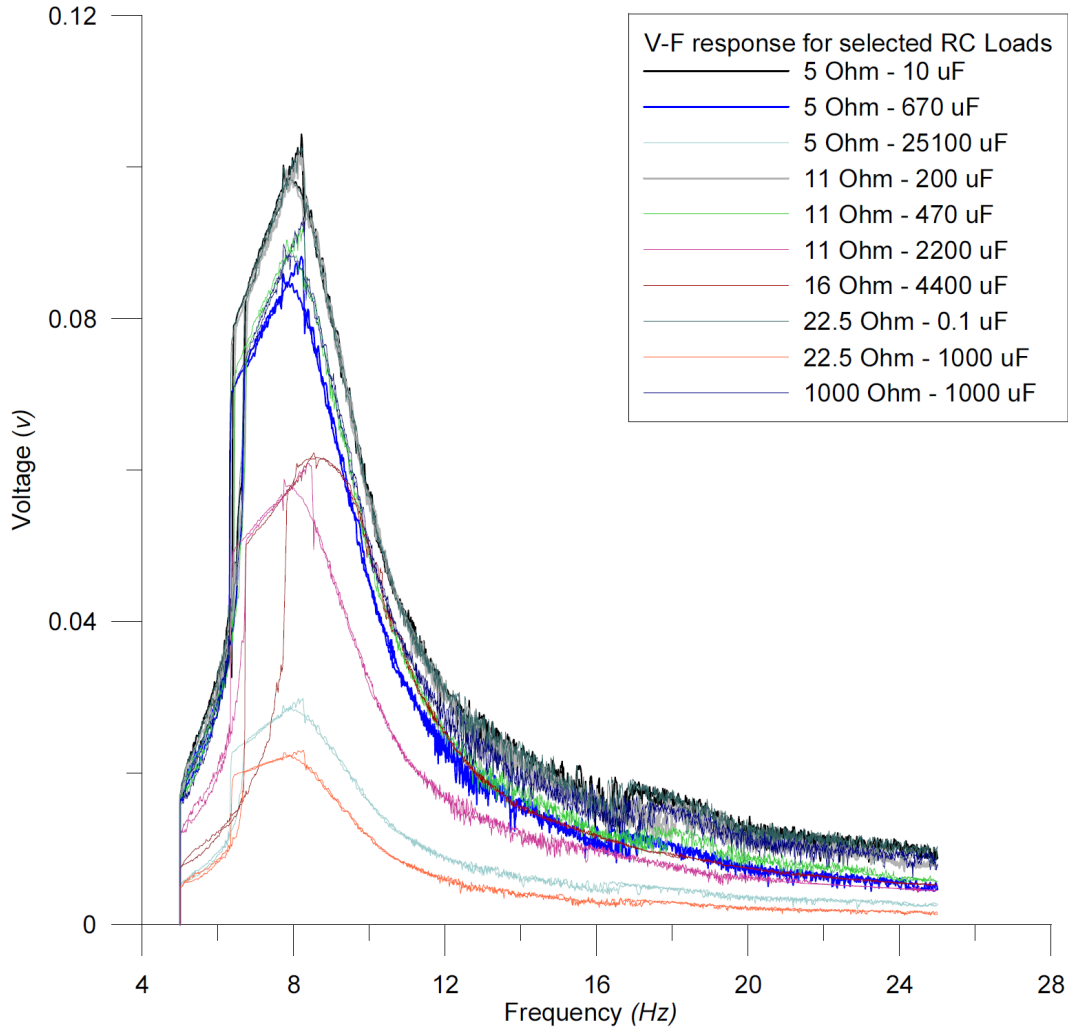
Figure 3.42: Measured voltage-frequency response for selected RC load values at an excitation of $A_o = 0.9g$

3.11.1   Discussion

The complex RC load adds extra damping and stiffness to the system; however, the added damping and stiffness are not of the same magnitude. Experimental results in table 3.15 show that the added damping due to the resistive component of the load, represented by $3dB$ bandwidth as a measure, is qualitatively small, ranging only between 2.51 and 2.72 Hz for tested values included in the experimental results. Even when the resistive component is multiple folds of the FDH parasitic resistance, R_{coil}. The capacitive component of the complex load increases the compliance of the system (compliance is the reciprocal of stiffness), resulting in a change in the FDH total stiffness that ranged between 23.128 and 26.25 for the different complex load values included in the experimental data, which consequently resulted in a change in center frequency, f_c, between 8.07 Hz and 8.64 Hz which is close to 7% when compared to the open-loop center
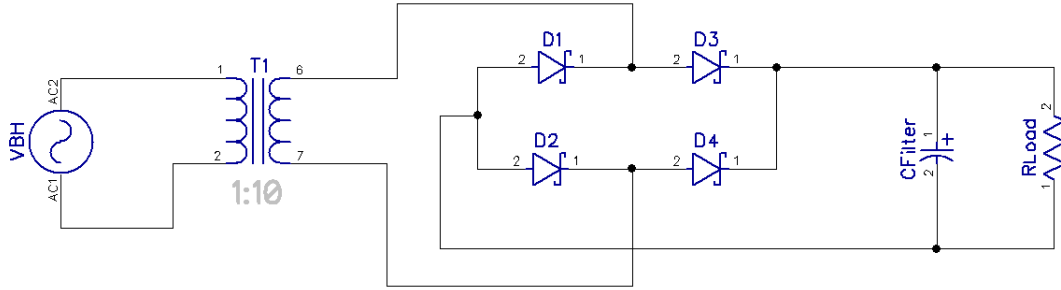
Figure 3.43: Schematic of a power supply unit using the FDH as a power source
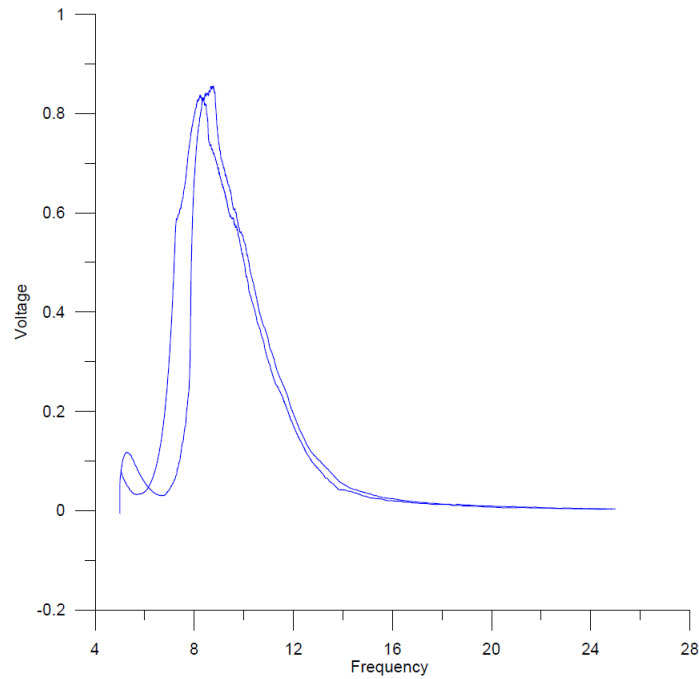
Figure 3.44: Voltage vs. Frequency response of the power supply unit at $100K\Omega$ resistive load and $100\mu F$ filter capacitor

frequency. In conclusion, the complex load RC components can be selected to tune the center frequency to a selected value or range to maximize energy harvesting and power transfer without a significant impact on the harvesting bandwidth.

The output power generated by the FDH at resonance can range from 0.11 to 127.16 μW, depending on the values of the attached RC load. This is sufficient to power low-power microcontrollers such as the nanoWatt XLP eXtreme Low Power PIC microcontrollers family from Microchip Technology [94–96], the STM8L/STM8AL [92] and STM32L [93] microcontroller families from STMicroelectronics. While the amount of power generated by the VBH may be considered low, it is sufficient to power ultra-low-power wireless communication modules and protocols such as EnOcean STM300 [91], SX1262, RFM95, inAir9 [89], Zigbee, and Thread [90], which only require a few tens of microWatts.
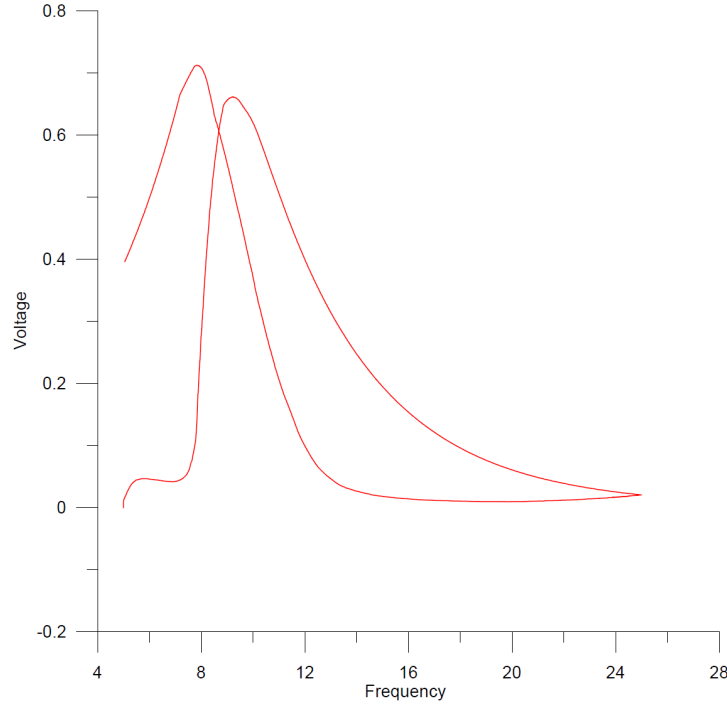
Figure 3.45: Voltage vs. Frequency response of the power supply unit at 100KΩ resistive load and $1000\mu F$ filter capacitor

It is worth noting that the purely resistive or complex RC load is not meant to serve as the primary load for the FDH. Instead, it is designed to be a component of an "Impedance Matching" circuitry alongside the externally selected load by the user, with the goal of achieving maximum power transfer. The role of the RC load network is to aid in frequency selection, thereby enhancing power generation by attaining resonance at the desired frequency or multiple frequencies, which can be adjusted through the RC load values. The subject of impedance matching is expansive and falls beyond the scope of this dissertation, thus it is not covered in the present discussion.

3.11.2   Power Analysis for RC Load

The power generated in magnetic-induction generator through sinusoidal excitation is given by[65]:

$$P = \frac{m\eta_e A_o^2 \left(\frac{\omega}{\omega_n}\right)^3 \omega^3}{\left[1 - \left(\frac{\omega}{\omega_n}\right)^2\right]^2 + \left[2\eta\frac{\omega}{\omega_n}\right]^2} \tag{3.24}$$

Where m is the proof mass of the moving object, A_o^2 is the amplitude of the excitation signal, η and η_e are the total and electrical damping factors, ω, and ω_n are the operating and natural frequencies, respectively. The maximum power is generated when the operating frequency ω is
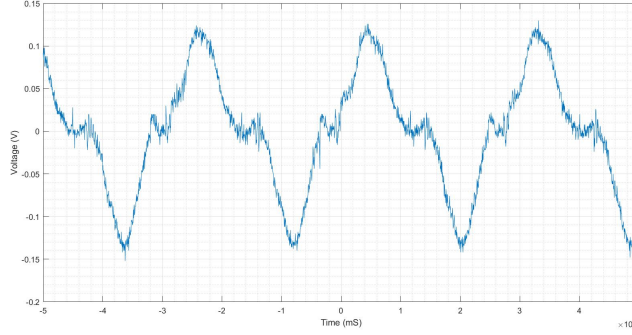
Figure 3.46: FDH output voltage waveform

equals to the natural frequency ω_n, the maximum power will reduce to[65]:

$$P_{max} = \frac{m\eta_e A_o^2 \omega_n^3}{4\eta^2} \tag{3.25}$$

For FDH, the power generated across an RC load cannot be calculated directly. Real power (for resistive loads) and reactive power (for capacitive loads) must be calculated separately, then combined to calculate the apparent power S. The generated power formula in 4.3.1 was cross-validated against experimentally measurements listed in table 3.15, measured power was calculated using the formula:

$$P = I_{rms}^2 Z \tag{3.26}$$

where I_{rms} is the measured RMS current in Ampere, and Z is the resistance or capacitive reactance.

The electrical damping factor (η_e) from[65] is modified to calculate the reactive power (for a capacitive load):

$$\eta_e = \frac{Bl^2/X_c}{2\omega_n m} \tag{3.27}$$

and for real power (for a resistive load), η_e is modified as well to become:

$$\eta_e = \frac{Bl^2/R_L}{2\omega_n m} \tag{3.28}$$

and apparent power, S, is given by:

$$|S| = \sqrt{P^2 + Q^2} \tag{3.29}$$

where P is the real power, and Q is the reactive power.

3.12   Parametric Design for Field Disruption Energy Harvester

The FDH design can be modified for the purposes of tuning the center frequency, the harvesting bandwidth, or both. There are three approaches to achieve these purposes:

- Mechanical Design Approach:

  The proof-mass of the moving object (the ferromagnetic ball) is inversely proportional to the center frequency of the harvester according to the relationship:

$$\omega_c = \sqrt{\frac{k}{m}} \tag{3.30}$$

  Where ω_c is the center frequency in radians, k is the harvester total stiffness, and m is the proof-mass of the moving object. Changing the length of the travel track is another mechanical parameter that affects the harvester center frequency since the magnetic restoring force is function of the distance between the permanent magnet and the moving object according to the harvester's model discussed in chapter 3 of the dissertation. The last mechanical parameter that affects harvesting bandwidth is the friction coefficient of the travel track. Where friction is directly proportional to harvester's total damping, and according to simulations the harvesting bandwidth is directly proportional to damping.

- Magnetic Circuit Approach:

  The FDH [32, 34] principle of operation relies on the magnetic design, where the magnetic restoring force, the main restoring force component in the oscillator, is function of the source of magnetic field characteristics, in the FDH's case it is a permanent magnet residual flux density and demagnetization force, and the Euclidean distance between the source of magnetic field and the moving object, the ferromagnetic steel ball. The mathematical model in section 3.3.2 of the dissertation describes the relation between the magnetic flux density, magnetic restoring force and distance to the ferromagnetic object. Simulations results, table 1 and figures 3.48 to 3.51, shows a noticable difference in the FDH center frequency and harvesting bandwidth if any component of the magnetic restoring force changes. Furthermore, to show how the magnetic restoring force impacts the FDH center frequency and harvesting bandwidth, table 3.17 and figure 3.47 show experimental results for different magnetic configurations for the same FDH mechanical design.

  To test the impact of the magnetic restroing force on the moving object, and consequently impacting the FDH's center frequency and bandwidth, different prototypes were developed with a selection of permanent magnets of different pulling force, mounted in different configurations along the travel track with respect to the steel ball.
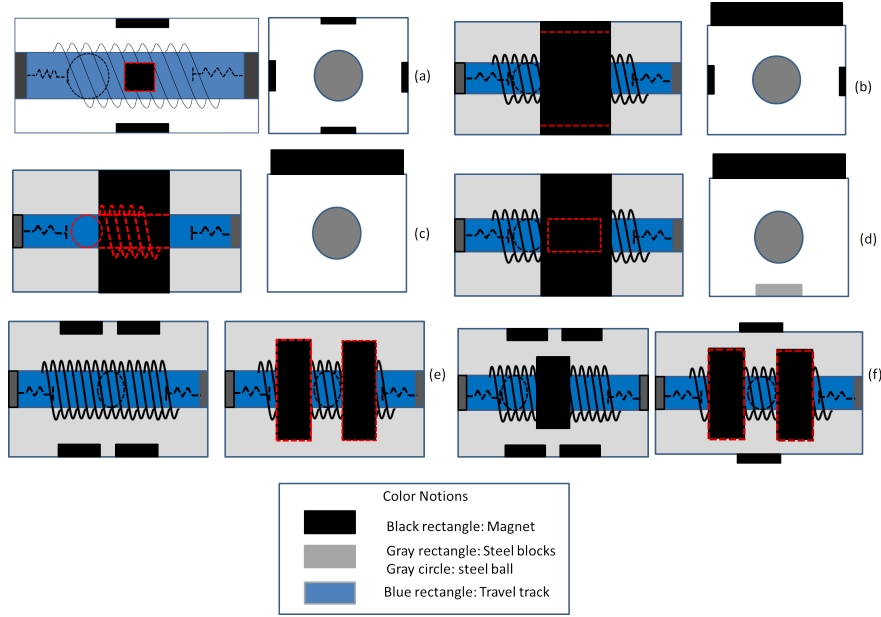
Figure 3.47: Different Magnetic Configurations for the FDH

Table 3.17: Center frequency and bandwidth for configurations listed in figure 3.47

Configuration	Center Frequency (Hz)	Harvesting Bandwidth(Hz)	Maximum Voltage (mV)
a	11.95	5.8	26
b	8.74	2.62	101
c	8.61	3.2	26.3
d	8.5	2.5	95
e	12.72	2.66	25.9
f	12.6	2.52	25.1

Figure 3.47 shows the different FDH prototypes developed for the testing. In configuration "a", four permanent magnets, where each has pull force of 2.57 *Ibs*, are used (part number B331), resulting in a weaker magnetic restoring force than configuration "b", which has two magnets having a pull force of 2.57 *Ibs* plus a strong magnet that has 130.4 *Ibs* pull force (part number BY0X08DCS [80]). In configuration "c" the magnetic restoring force didn't change significantly after removing the side magnets in configuration "b", resulting in a center frequency close the one for configuration "b". In configuration "d" a think rectangular block of steel was mounted on the floor of the FDH container, acting as a flux concentrator, changing the magnetic restoring force and reducing the system total stiffness, resulting in lower center frequency. Configurations "e" and "f" used permanent magnets bigger than the ones used in configuration "a" with pull force of 32.45 *Ibs* (part number BX082CS-N), but still significantly smaller in strength than the magnet used for configurations "b" and "c", resulting in increasing the total stiffness and thus the center frequency, also these configura-
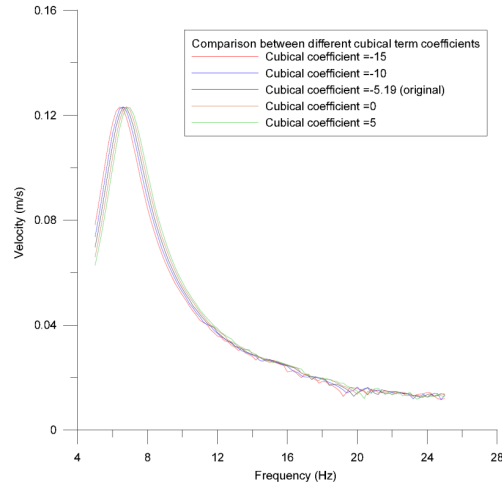
Figure 3.48: Simulated frequency response for different values for the magnetic restoring force cubical term
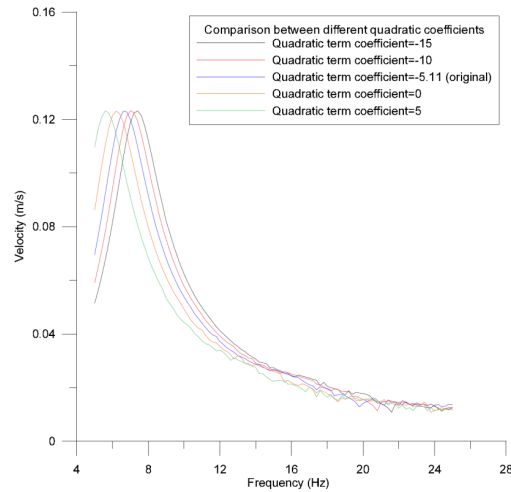
Figure 3.49: Simulated frequency response for different values for the magnetic restoring force quadratic term

tions have less harvesting bandwidth than "b" and "c", which means reduction in damping compared to configurations "b" and "c".

- Electrical Design Approach:

  Experimental results had shown a relationship between the FDH operational parameters (center frequency and harvesting bandwidth) and the type of electrical load connected to the harvester. In the FDH, the electric load can be integrated in the harvester design and used as a tuning utility for different operational parameters. Experimental results showed that the type of the electric load connected to the FDH can affect the harvester's center frequency and $3dB$ bandwidth. Table 3.15 shows the results of FDH testing with a combination of resistor-capacitor (RC) loads and the respective measured center frequency,
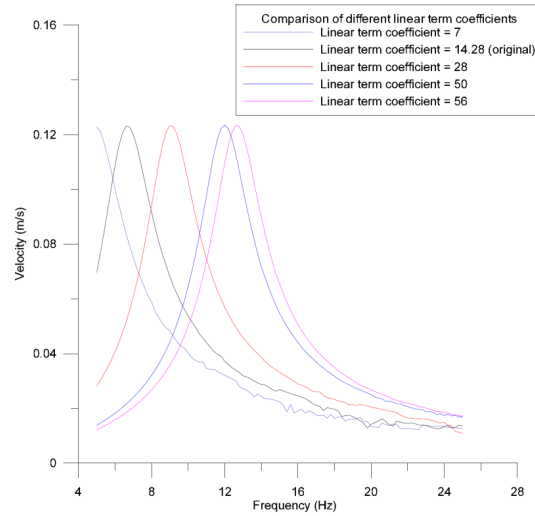
Figure 3.50: Simulated frequency response for different values for the magnetic restoring force linear term
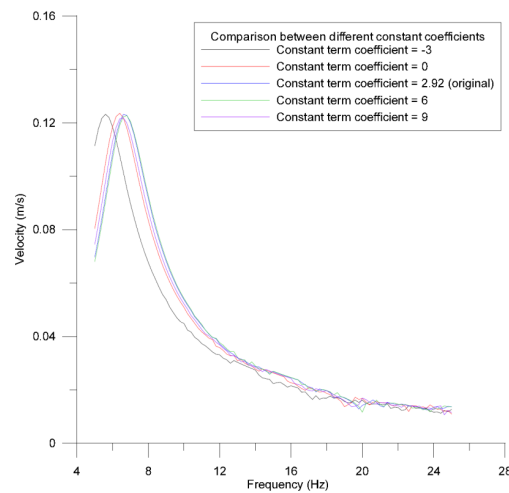
Figure 3.51: Simulated frequency response for different values for the magnetic restoring force constant term

$3dB$ harvesting bandwidth, real power and quality factor. These results led to the conclusion that an external RC electric load circuit can be used as a tunning element for the harvester's center frequency and 3dB harvesting bandwidth to match the operating conditions of the desired environment for maximum power generation and improved efficiency, which is a novel approach to use passive electronic components to assist tunning.

3.13 Summary of Experimental Results

In section 3.7, the he experimental results of different coil configurations impact on the FDH response were presented. The center frequency was modulated by changing the number of coil turns and the material of the travel-track. Increasing the coil turns and replacing the dielectric track material with conductors (e.g. copper) lowered the center frequency. On the other hand, the $3dB$ bandwidth increased, indicating a reduction in total damping due to increased counter magnetic field generated within the coil. In the case of FDH with copper travel-track, the magnetized steel ball moving across the track induces current in the copper tube according to Lenz's law [73], creating a counter magnetic field that resists the motion of moving object. The counter magnetic field contributes to the total damping along with magnets and coil magnetic fields.

Section 3.8 presented analysis for the impact increasing the magnetic field strength by either using multiple, stronger magnets, or a combination of both, which increased the system overall damping. This enabled harvesting energy at lower frequencies below $10\ Hz$ without the need to modify the mechanical design, and this allowed the harvester to be "magnetically tunable", and this is considered a major design advantage.

The discussion in section 3.10 demonstrated that maximum power transfer occurs at 5.6Ω resistive load for the full-covered track, with 960 number of turns coil FDH configuration 3.9, generating $154\mu W$ at resonance, which is sufficient to power low-power microcontrollers and wireless communication systems such as LoRaWAN and SigFox.

After analyzing the experimental results for different FDH physical structures, it is concluded that coil structure and magnetic configuration can be used to tune the FDH center frequency. This introduces flexibility of operation under different excitation frequencies, harvesting more energy than fixed center frequency VEH. This feature is used in the next chapter to design an intelligent frequency tuner to control the FDH center frequency.

Chapter 4

FDH Parameter Design using Machine Learning

4.1 Introduction

Artificial intelligence algorithms may be employed in the design workflow of the energy harvesters. A model would be created and fed previously collected training data, then extract patterns and extract unique features and correlations between system variables, then identify the optimal system configurations to enhance the performance.

The concept of energy harvesting has the potential to unleash unprecedented applications. However, the application of energy harvesters is limited by intermittent power and efficiency. The application of machine learning techniques in the design and operation of energy harvesters can improve the harvesters' efficiency by addressing the previously mentioned limitations. These improvements may allow the utilization of harvesters in wide range of new applications.

This chapter introduces two novel machine learning algorithms that were employed in the design of biaxial variable-flux energy harvesters (FDH)[32] [34]. The results exhibit the capability of the algorithms to realize harvester designs capable of achieving the desired center frequency and harvesting bandwidth to maximize power generation. This chaper also provides comparative analysis for the performance of the two algorithms. The first algorithm is the Fuzzy C-means clustering (FCM) combined with a fuzzy inference system to estimate the magnetic restoring force for a desired center frequency. This was achieved by generating fuzzy inference rules from fuzzy C-means clustering and a create a model that uses the magnetic restoring force (F_m) values generated from the FDH model[34]. Finally, the fuzzy inference rules predicted the required magnetic restoring force for a specific frequency with an accuracy of 98%. The second algorithm employs Artificial Neural Network (ANN) to predict the optimum load required to tune the FDH center frequency.

The end goal is to estimate the FDH load based on the operating frequency at any moment, waiving the need to recalibrate the harvester in case the external excitation frequency changes. The dataset used was generated from experimental tests conducted by manually changing the values of the complex load components attached to the FDH output and measure the center frequency and bandwidth of the output, the experimental results are listed in table 3.15. Where the vital

Table 4.1: FDH vital parameters

Symbol	Parameter	Type
A_o	Excitation amplitude	System input
f_o	Excitation frequency	System input
F_m	Magnetic restoring force	Design specific
C_m	Mechanical damping	Design parameter
L	Coil inductance	Design parameter
Z_L	Load impedance	Design parameter
V_o	Output voltage	System output
P	Output power	System output
f_r	Center frequency	System output
Δf	3dB harvesting bandwidth	System output
Q	Quality factor	System output

system variables listed in table 4.1 can be categorized into:

- System input variables: these system variables exist in the operating environment of the harvester and we have no control over them.

- Design specific variables: these are the system variables related to the harvester design, any change in these with respect to the system input parameter reflects on the system outputs.

- System output variables: the harvester output that reflects, quantitatively, the harvested energy.

Previous experiments in chapter 3.5 showed that any change in the system input or design specific variables (including magnetic field configuration, output load, or coil design) directly affects the harvester's output and changing the amount of generated power. We propose using these parameters to our advantage to tune the harvester to the external excitation frequency for maximum power transfer.

4.2   Center frequency estimation using FCM

As a refresher on the FDH principle of operation, the FDH consists of an impact oscillator coupled to an inductive circuit as shown in figure 3.3. A simple oscillator is made up of is made up of a steel sphere and mechanical end-springs, while the inductive circuit comprises of a top magnet, a coil, and a moving steel ball. The top magnet is the source of the magnetic force. A schematic

of the FDH is demonstrated in figures 3.4 and 3.1; A copper coil is wound around a dielectric tube and a single magnet is placed on top of the coil-tube assembly. A ferromagnetic sphere may move freely along a track inside the tube. Two springs are attached at the end caps of the tube to tune the FDH peak frequency. The FDH is mounted onto an electrically non-conductive material, such that the center lines of the magnet and coil are aligned with the track mid-section as shown in figure 3.2. Tables 3.1 and 3.2 list the system design parameters including distance measured between the top magnet and the coil d, coil resistance R_c, and the magnetic flux density at the center of the tube B_o in the absence of the sphere. The describing equation-of-motion is:

$$\ddot{x} + \left(\frac{c_m + c_e}{m}\right)\dot{x} + \left(\frac{c_3}{m}\right)x^2\dot{x} + \left(\frac{F_s}{m}\right) + \frac{1}{m}(-5.19x^3 - 23.05x^2 + 14.28x + 2.92) = \ddot{y}(t) \quad (4.1)$$

where $\ddot{x}$ and $\dot{x}$ are the acceleration and velocity of the proof-mass, respectively, c_m and c_e are the mechanical and electrical damping coefficients, respectively, c_3 is the cubic damping coefficient resulting from impact losses, m is the mass of the moving object (metallic ball), F_s is the mechanical springs restoring force, and $\ddot{y}(t)$ is the external excitation. The expression $\frac{1}{m}(-5.19x^3 - 23.05x^2 + 14.28x + 2.92)$ represents the magnetic force exerted by the magnet on the moving object. Coefficients of the magnetic restoring force Fm were experimentally derived by measuring the exerted force -resulting from a magnetic field source (permanent magnets)- on the moving steel ball as a function of distance between the steel ball and source of magnetic field. Experiments and simulations showed that the FDH center frequency and $3dB$ harvesting bandwidth are function of the magnetic restoring force applied on the moving sphere. Changing the magnetic restoring force applied on the moving ferromagnetic ball by applying the different magnetic configurations shown in figure 3.47, resulted in different center frequencies and bandwidths. Results listed in in table 1 exhibits a change in the total stiffness of the system according to the governing equation of a mechanical oscillator frequency:

$$f_o = \frac{1}{2\pi}\sqrt{\frac{k}{m}} \quad (4.2)$$

where f_o is the center frequency, k is the total stiffness of the oscillator, and m is the proof-mass of the moving object.

4.2.1 About Fuzzy C-Means Clustering Algorithm

Cluster analysis, or commonly known as clustering, is the process of grouping a set of data objects with similar attributes in clusters for further analysis and characterization. Where each data object may belong to one or more data clusters depending on the clustering algorithm used whether it's hard or soft clustering. In soft clustering, data objects can belong to multiple clusters,
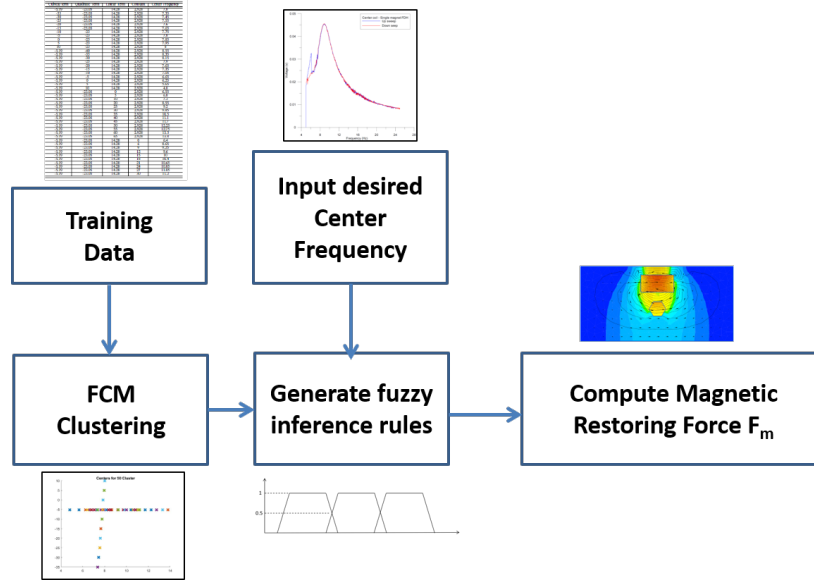
Figure 4.1: FCM algorithm flow diagram for magnetic restoring force selection

where the level of "belongness" to each cluster is called "Degree of Membership", such as in FCM[74][75], while in hard clustering, each data object belongs only to one single cluster. Fuzzy C-Means (FCM) clustering, is a soft clustering algorithm where each data points can belong to more than cluster [74] [75] [76]. The relationship between a data point and the associated cluster(s) is defined by the "degree of membership" (DoM) to each cluster based on the distance and connectivity to the center of the cluster. A DoM takes a value between 0 and 1, where 0 indicates that the data point does not to the cluster of interest and 1 is the highest grade of belonging to that cluster. FCM can be used to infer fuzzy rules that define the relationship between data points and clusters. The objective function of the Fuzzy C-Means is minimized to:

$$J_m = \sum_{i=1}^{N} \sum_{j=1}^{C} u_{ij}^m \parallel x_i - c_j \parallel^2, 1 \leq m < \infty \tag{4.3}$$

where m is a real number greater than 1, u_{ij} is the degree of membership of a data point x_i in cluster j, x_i is the ith of d-dimension data point, and c_j is the d-dimension center of cluster, and $\parallel x_i - c_j \parallel$ is the Euclidean distance between the ith data point and j^{th} cluster center [83]. Using iterative optimization of the objective function, for each step of the iteration, cluster centers vector is computed as:

$$c_j = \frac{\sum_{N}^{i=1} u_{ij}^m \cdot x_i}{\sum_{j=1}^{N} u_{ij}^m} \tag{4.4}$$

then update the membership function:

$$u_{ij} = \frac{1}{\sum_{k-1}^{C} \left(\frac{\|x_i - c_j\|}{\|x_i - c_k\|} \right)^{\frac{2}{m-1}}} \tag{4.5}$$

The objective function J_m is iteratively calculated from the updated clusters centers vector membership functions until minimum J_m is achieved. FCM algorithm is efficient in separating data points with a degree of similarity to each other, such as the FDH's magnetic restoring force F_m versus center frequency f_c. The data points (F_m, f_c) can be very close to each other, leading to an increase in uncertainty. FCM resolves the issue by assigning each (F_m, f_c) data point to multiple classes and defines the degree of membership in each class. The fuzzy rules generated from the FCM are used in a consequent stage to facilitate the selection of nearest class to the desired center frequency.

4.2.2   Algorithm flow and simulation results

Data for magnetic restoring force coefficients and corresponding center frequencies were generated first from the FDH equation of motion 3.14. This dataset is fed to a Fuzzy C-means engine as training data to generate clusters that correlate the magnetic restoring force coefficient terms from equation (cubical, quadratic, linear & constant terms) and center frequency. A Mamdani's fuzzy inference method [77] is applied to the clustered data to extract a set of IF-THEN fuzzy rules to compute the magnetic restoring force coefficients for a user-input desired center frequency. A high-level overview of the frequency estimation FCM-based algorithm is shown in figure 4.1.

The calculated coefficients can be utilized in conjunction with a magnetic field finite element analysis (FEA) solver, such as COMSOL, Ansys, or QuickField, to design the magnetic configuration of the FDH. This configuration aims to achieve resonance at the specific center frequency as desired by the user, and/or assist in designing the permanent magnet employed in the FDH. Figure 4.2 demonstrates the application of the FCM tuner, aided by FEA, to design the magnetic field configuration of the FDH. The algorithm and simulations were created and tested using MATLAB Fuzzy Logic Toolbox. The fuzzy membership rules were generated using "Mamdani inferencing system". Simulation results showed that the algorithm accuracy to compute the desired magnetic restoring force (F_m) for a given center frequency (f_c) increases as the number of clusters and associated fuzzy rules increase to 44 clusters. This is followed by convergence and the accuracy of magnetic restoring force coefficients dooes not change much after that. Figures 5 and 4 show the fuzzy membership functions generated from 10 clusters and 44 clusters. The granularity of the membership functions increases as the number of clusters increases, and this increases the accuracy of the desired center frequency. The F_m coefficients are embedded in the FDH model
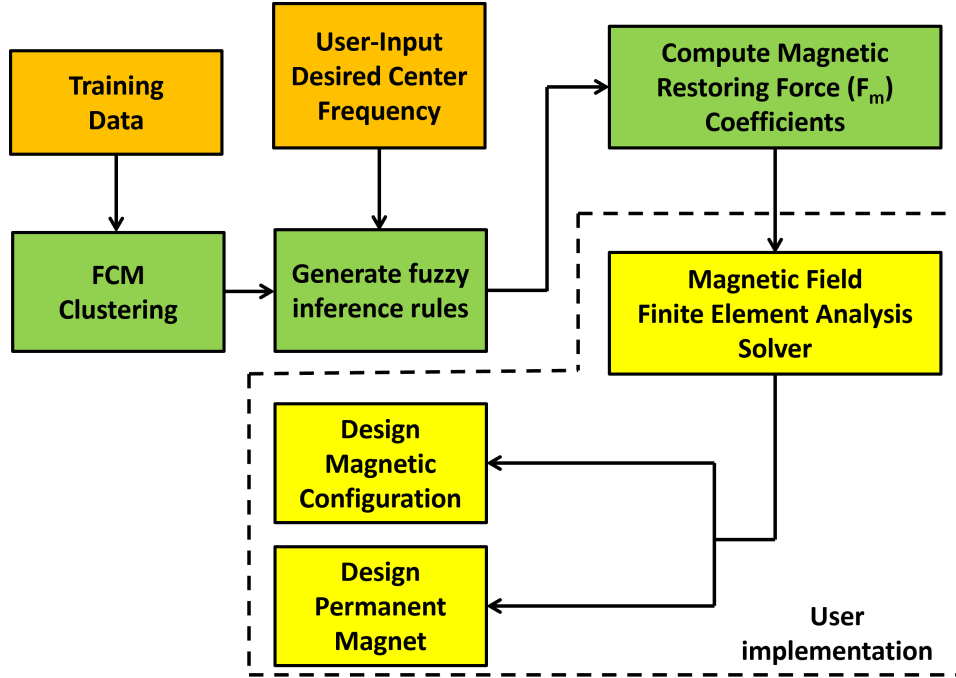
Figure 4.2: Usage of the FCM tuner with the aid of FEA for magnetic design configuration
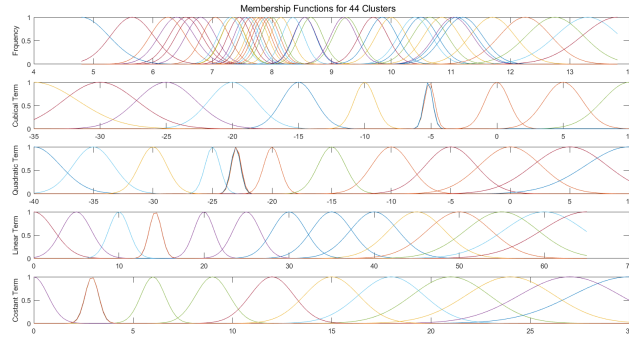
Figure 4.3: Membership functions for center frequency f_c and magnetic restoring force F_m coefficients generated from 44 clusters

shown in equation 4.1. FCM inference algorithm with 44 clusters produced the cubical, quadratic, linear and constant terms. Finally, the magnetic restoring force (F_m) coefficients for the different terms were computed for specific input center frequencies, the results are listed in Table 4.2. The resulting center frequency from model simulations (f_c) always fall within the $3dB$ harvesting bandwidth [34], hence, maximizing the generated power even if the harvester center frequency was not completely matching the desired input frequency fed to the FCM engine.
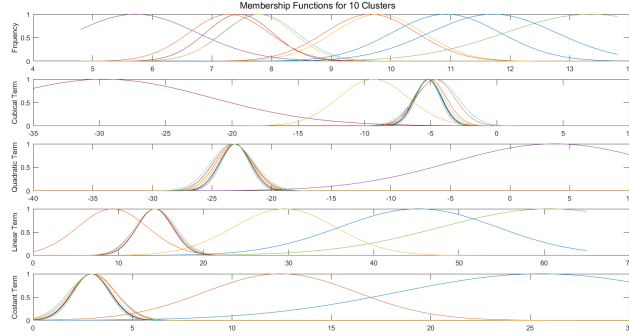
Figure 4.4: Membership functions for center frequency f_c and magnetic restoring force F_m coefficients generated from 10 clusters

Table 4.2: Simulation results for selected magnetic restoring force coeffecients vs. center frequency generated by the FCM algorithm

Cubical coeff.	Quadratic coeff.	Linear coeff.	Constant coeff.	FCM input f_c (Hz)	f_c from simulations (Hz)
-10.4717	-23.1140	13.5631	2.9286	7.8	7.65
-17.0956	-19.8342	12.4671	2.9264	7.65	7.2
-5.1937	-23.0501	51.2302	4.5389	12.25	12.55
-5.1935	-23.0497	33.0495	20.7413	10.65	12.15
-5.9098	-5.6582	6.0663	1.7173	6.65	4.75
-5.1935	-23.0498	38.0516	23.1029	11.2	12.7
-5.0493	-34.0432	18.1704	5.0806	8.65	9.45

4.3   Center frequency estimation using ANN

Refering to section 3.11, that the center frequency is affected by the type of the load connected to the FDH output. Experimental results from chapter 3.5 [35] showed that an in-series RC load can be used to tune the center frequency, f_c, electronically without any change to the mechanical or magnetic configuration of the FDH.

To automate the selection process, a regression solver using multi-layer feed-forward Artificial Neural Network (ANN) is used for computing the RC network values for any desired frequency. The training dataset for the ANN is obtained from experimental results listed in table 3.15.

The regression solver is developed with "Fast Artificial Neural Network library" (FANN)[84], open source multi-layer ANN developed in C programming language that uses back-propagation learning algorithm. The library implementation in C makes it fast, dynamic, and cross-platform (i.e. compatible with different operating systems). It can operate on different CPU architectures including general purpose microprocessors and bare-metal embedded processors (e.g., ARM Cortex-M architecture)[87].
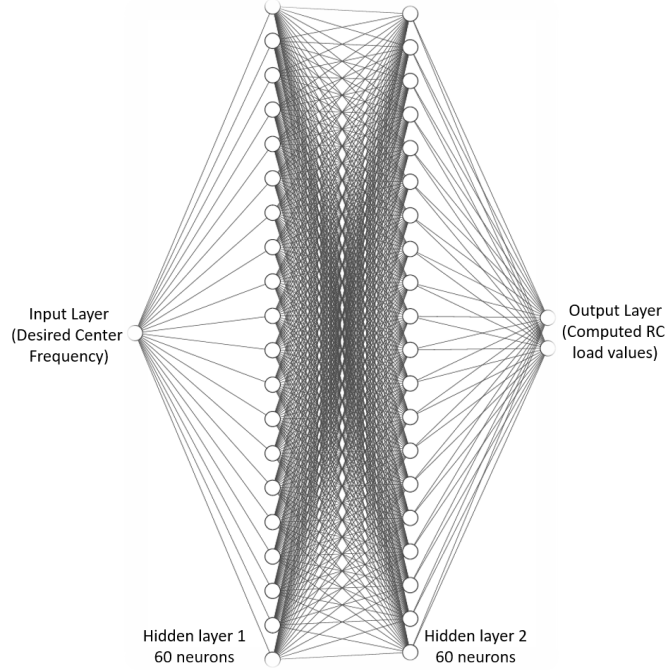
Figure 4.5: ANN architecture for computing RC load values

The RC load selection algorithm can be operated in real-time. The designed ANN takes a single input to specify the "desired center frequency", and produces the resistance and capacitance values of the RC load network. The ANN has two hidden layers, each has 60 neurons. The network architecture is shown in figure 4.5 and the implementation parameters are listed table 4.3. It uses linear activation function for the output layer described by equations 4.6 and 4.7[84], and sigmoid-like fast activation function for the hidden layers, described by equations 4.8 and 4.9 [85][84]. Two different types of activation functions were used due to the nonlinear behavior of the FDH when connected to RC load network. A linear activation function cannot converge correctly and would produce incorrect results.

$$y = x.s, \qquad -\infty < y < \infty \tag{4.6}$$

$$d = s \tag{4.7}$$

$$y = ((x.s)/2)/(1 + |x.s|) + 0.5, \qquad 0 < y < 1 \tag{4.8}$$

$$d = s/(2(1 + |x.s|)(1 + |x.s|)) \tag{4.9}$$

where x is the input of the activation function, y is the output of the activation function, s is the activation function steepness and d is the derivation[84]. The ANN predicted the RC values with a margin of error averaging around 6% for resistance, and 7% for capacitance values. These
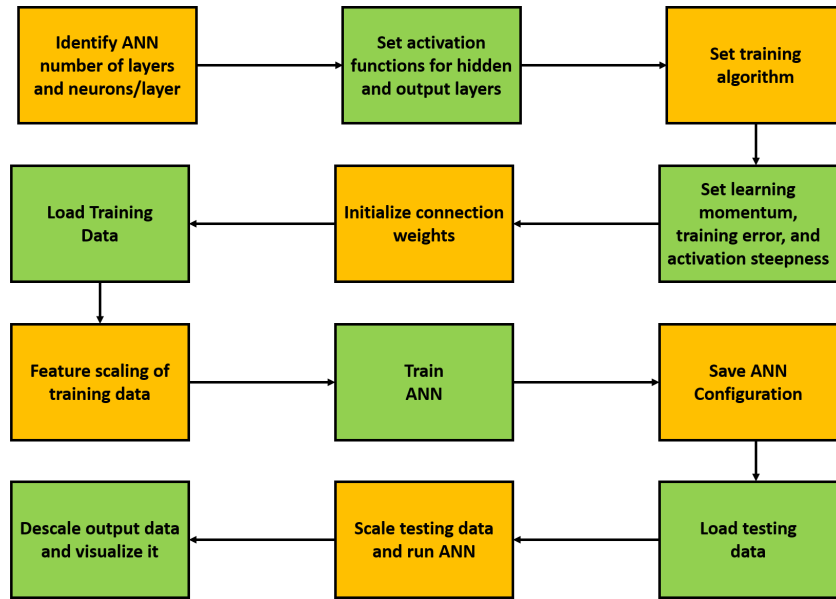
Figure 4.6: Algorithm flow for RC load values estimation using ANN

results indicate that the FDH actual center frequency will not match the desired center frequency, however, it will fall within the $3dB$ harvesting bandwidth, thus maximizing the generated power.

4.3.1   Algorithm flow and simulation results

The ANN uses regression algorithm to estimate the values of in-series RC components which are required to set the FDH center frequency to match a desired frequency. Optimally, the desired frequency will match the resonance frequency, thus maximize the generated power according to equations and . The ANN engine follows these steps to create the network, train it, and estimate the loads:

1. Define the number of layers for the input, hidden and output layers.

2. Set the activation function for the hidden and output layers. The hidden layer uses a sigmoid-like fast activation function, while the output layer uses a linear activation function.

3. Set the learning momentum and the training algorithm of the ANN. The RPROP algorithm is used for training the ANN.

4. Initialize ANN weights for all connections. The FANN library automates the weight initialization and configuration.

5. The training data is subject to "feature scaling" prior to being loaded to the ANN. This preprocessing measure is essential to ensure a faster convergence of the gradient descent.

Table 4.3: ANN Parameters for RC Network Selection

Parameter	Value
Number of inputs	1
Number of Outputs	2
Number of layers	4
Number of hidden neurons	60
Maximum number of epochs	100000
Hidden layer activation function	Sigmoid-like fast activation function developed by D. Elliot [85]
Output layer activation function	Linear
Learning momentum	0.5
Training algorithm	RPROP [86]
Error function training algorithm	Standard linear error function
Hidden layers steepness activation	0.5
Output layer steepness activation	0.1
Training data scaled	yes

6. The ANN is trained with data obtained from previously conducted experiments results, the data is listed in table 3.15.

7. Once training is completed, the ANN configuration is saved in a ".net" format. The ".net" file format is used by FANN [84] to save the configuration and network model for future use.

8. Testing data is scaled, then loaded to the ANN and the output is descaled prior to visualization.

For real-time applications, the ANN can run on an embedded system (e.g., microcontroller or SoC) to estimate the RC load values and control the center frequency to maximize power generation. Fewer steps can execute on the embedded CPU to reduce computation overhead and speed up processing. ANN configuration and training data (steps 1 to 6) can be created on a PC in a format that is compatible with the embedded CPU [87], and only steps 7 and 8 can run on the embedded system CPU.

The algorithm for RC load network selection utilizes Fast Artificial Neural Network library (FANN)[84], an open source multi-layer ANN developed in C programming language that uses back-propagation learning algorithm. The library implementation in "C" makes it fast, dynamic, and cross-platform. It can execute on different CPU architectures including general purpose

Table 4.4: Results of the ANN used to select RC network values

Computed Resistance	Computed Capacitance	Original Resistance	Original Capacitance	Error for Resistance	Error for Capacitance	Error % for Resistance	Error % for Capacitance
5.43	1214.75	5	1200	0.43	14.75	8.53	1.22
4.58	659.77	5	670	0.42	10.23	8.31	1.52
5.18	100.64	5	100	0.18	0.64	3.68	0.63
5.35	997.68	5	1000	0.35	2.32	7.09	0.23
5.14	7699.73	5	7700	0.14	0.27	2.73	0.003
8.16	999.17	8.4	1000	0.24	0.83	2.88	0.083
10.88	2198.18	11	2200	0.12	1.82	1.071	0.082
9.92	5406.73	11	5400	1.08	6.73	9.82	0.124
11.15	843.54	11	820	0.15	23.54	1.32	2.87
10.86	4381.49	11	4400	0.14	18.51	1.25	0.42
20.23	4304.57	16	4400	4.23	95.43	26.40	2.16
12.82	2344.5	16	2200	3.18	144.5	19.89	6.56
22.07	106.83	22.5	100	0.43	6.83	1.92	6.83
100.5	992.64	100	1000	0.5	7.36	0.5	0.73
1000.11	998.95	1000	1000	0.11	1.05	0.011	0.104
998.95	1.07	1000	10	1.05	8.93	0.105	89.26

microprocessors and bare-metal embedded processors such as ARM Cortex-M architecture[87]. Real-time implementation was achieved by running the designed ANN algorithm for RC load selection on a Texas Instruments TM4C1294 ARM Cortex-M4F microcontroller [88].

4.4   Summary of Results

This chapter presented methodology to estimate center frequency using two different machine learning algorithms, the first uses Fuzzy C-Means (FCM) clustering, end the second uses Artificial Neural Network (ANN) algorithms to estimate the center frequency (f_c) of the field disruption energy harvester (FDH) by computing the corresponding magnetic restoring force (F_m) coefficients or the RC load values. This has been achieved by utilizing existing experimental results and simulations as the training data for both algorithms. The existing simulation data for the magnetic restoring force ((F_m) fed to FCM algorithm is capable of computing Fm for a desired frequency with deviation less than 13%; which allows the output frequency to consistently fall within the 3dB harvesting bandwidth.

The ANN algorithm to estimate the RC load values for desired center frequencies with error less than 10% in most of the use cases. The results allow the FDH center frequency to be always tuned within the $3dB$ harvesting bandwidth, thus maximizing the generated power. This approach allows the FDH to operate at any external excitation frequency without the need to match it to a preset center frequency.

Chapter 5

Summary & Future Work

5.1 Field Disruption Energy Harvester: What's New?

This thesis presented a new architecture and design for mass-on-spring electromagnetic-based vibration energy harvester with a novel transduction mechanism. The theory of operation of the proposed design employs disrupting a stationary magnetic field created by one or more permanent magnet and a moving ferromagnetic object. The moving ferromagnetic object can be part of the VEH hardware or external to the VEH design, roaming in the vicinity of the magnetic field. The magnetic reluctance of the ferromagnetic object will vary due to this motion resulting in an induced current in the stationary coil wound. Chapters 1 and 2 demonstrated the shortage in existing VEH research and vibration energy harvesters with emphasis on harvesting relatively high powers at low frequencies (below 10 Hz), which established the motivation to pursue this novel design and expanded analysis.

Chapter 3 introduced the basic FDH design, theory of operation and analysis of the harvester's dynamics, supported with mathematical derivation of the equation of motion, simulation and comparison to experimental results.

The research outcomes and analyses concluded the correlation between the magnetic charactertistics and the performance metrics of the Field Disruption Harvester, FDH. Chapter 3.5 investigated different experimental aspects of the FDH such as the magnetic configuration, coil design and the role of external circuitry in the system dynamics. The experiments conducted on the FDH showed new non-mechanical techniques to tune the center frequency and $3dB$ harvesting bandwidth using three different ways:

- Tuning the magnetic field configuration by allocating permanent magnets in different orientations, or using magnets with different magnetic properties, as presented in section 3.8.

- Coil design, whether it is centered to the travel-track or covering all of it, and how the

coil design can be combined with the travel track material to change the coil inductance as presented in section 3.7.

- Output load circuit by using a complex RC load instead of a simple purely resistive load as presented in section 3.11.

5.2   Intelligent Energy Harvesting: New Horizons

The three methods listed in section 5.1, alongside with mechanical techniques such as changing proof-mass of the moving object or stiffness of end-springs, makes the FDH tuning more flexible and fit for a wider range of applications.

The presented designs for an intelligent energy harvesting that uses two machine learning algorithms: Fuzzy C-Means Clustering (FCM) and Artificial Neural Network (ANN), increases the flexibility and suitability of the FDH in environments where the excitation frequency varies stochastically or unknown to the end-user.

The Fuzzy C-Means Clustering(FCM) algorithm was capable of estimating the magnetic restoring force four coefficients with a small dataset (less than 50 data points) with an accuracy of 98%, reducing the complexity of calculating the coefficients using traditional ways such as simulations and mathematical derivation, also offers the option for real-time estimation if the computing power is accessible.

The Artificial Neural Network (ANN) was acapable of estimating the RC load values for any desired excitation frequency, with an accuracy close to 6% and 7% for the resistance and capacitance, respectively. This method is more promising than the magnetic restoring force tuning using FCM for two main reasons:

- The tuning of the resistive and capacitive components can be done in a real-time fashion using inexpensive electronic components such as a digitial potentiometer and a digitally-tuned capacitor.

- The ANN algorithm can run standalone on a TM4C1294[88] low-power ARM Cortex-M4F microcontroller from Texas Instruments.

All results for the FDH design and the three tuning techniques were heavily validated and analyzed via hundreds of lab experiments and simulation runs in a sincere effort to cover all possible angels for future researchers.

5.3   Future Work

In this thesis, the primary focus was on a significant challenge faced by vibration energy harvesting, which is the ability to harvest energy from vibrations at low frequencies, specifically those below 10 Hz. As we move into the third decade of the 2000s, a multitude of challenges emerge for vibration energy harvesting, encompassing not just one, but several factors, including:

- Generated output power is still too low for many electronic systems, especially devices with high-speed data conncetivity.

- The electromagnetic VEH is not compact enough to be embedded on-chip or within a device battery.

- The significant improvement in battery and energy storage technologies, which was not paralleled in the field of vibration energy harvesting, that lead to less interest in energy harvesting in general.

- Configurability of a vibration energy harvester, especially in unpredictable environments.

In order to overcome the limitations of the FDH and enhance its functionality, two recommended directions should be pursued to achieve improved performance and operability. The initial strategy involves enhancing the performance of the center frequency selection tools mentioned in the preceding chapter.

- Improving algorithms performance by creating a more dense training dataset that cover a wider frequency range. Such datasets will increase the accuracy and reliability of the FDH to operate at different excitations.

- Hardware implementation of a real-time online-based learning system using a real-time controller (MCU, MPU, or SoC), where dataset is acquired and processed in real time. A proposed hardware implementation for a frequency tuning real-time controller is shown in figure 5.1.

The second strategy involves exploring hardware modifications that aim to enhance performance and boost the generated output power. Some of these changes include:

- Change the proof-mass material (steel) to a different one with higher permeability such as Nickel and pure steel with little or without any carbon content in its alloy.

- Improve the coil structure by using different wire gaugaes with less resistance to reduce losses.

- Lamination of the moving proof-mass to reduce eddy current losses.
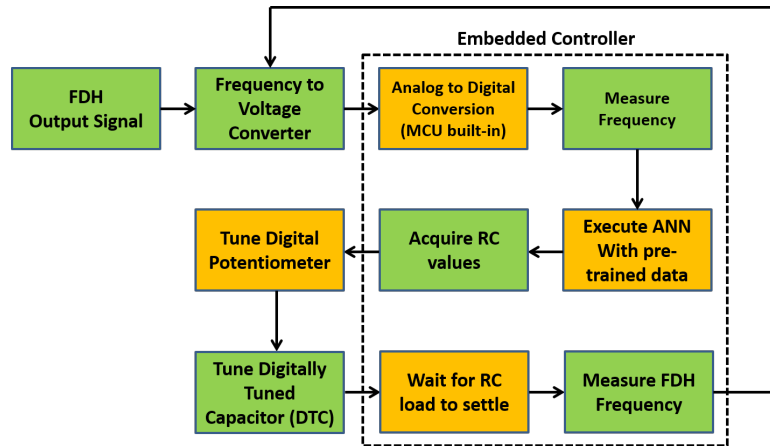
Figure 5.1: Proposed hardware implementation for a real-time center frequency tuner using ANN running on an embedded system

- Replace the travel track material to a ferromagnetic one such as copper to increase magnetic induction.

- Evaluate the performance of the FDH by subjecting it to various excitation waveforms beyond sinusoidal, including stochastic, step, square, and triangular waveforms.

References

[1] "Tessa Henderson, Energy harvesting roads in Israel",
`http://www.energyharvestingjournal.com/articles/1589/`
`energy-harvesting-roads-in-israel`.
Online, date accessed: April, 2023.

[2] P.D. Mitcheson, E.M. Yeatman, G.K. Rao, A.S. Holmes, and T.C. Green, "Energy Harvesting From Human and Machine Motion for Wireless Electronic Devices", *Proceedings of the IEEE*, Volume 96, no. 9, pp. 1457-1486, 2008.

[3] S. P. Beeby, M. J. Tudor, and N. M. White, "Energy harvesting vibration sources for microsystems applications", *Measurement Science and Technology*, Volume 17, no. 12, 2006.

[4] B.P. Mann, B.A. Owens, "Investigations of a nonlinear energy harvester with a bistable potential well", *Journal of Sound and Vibration*, Volume 329, Issue 9, pp. 1215-1226, 2010.

[5] R. Amirtharajah, A.P. Chandrakasan, "Self-powered signal processing using vibration-based power generation", *IEEE Journal of Solid-State Circuits*, Volume 33, no.5, pp.687-695, 1998.

[6] S. P. Beeby, R. N. Torah, M. J. Tudor, P. Glynne-Jones, T. O'Donnell, C. R. Saha, and S. Roy, "A micro electromagnetic generator for vibration energy harvesting", *Journal of Micromechanics and Microengineering*, Volume 17, no. 7, pp. 1257-1265, 2007.

[7] Ibrahim Sari, Tuna Balkan, Haluk Kulah, "An electromagnetic micro power generator for wideband environmental vibrations", *Sensors and Actuators A: Physical*, Volumes 145-146, pp. 405-413, 2008.

[8] Pei-Hong Wang, Xu-Han Dai, Dong-Ming Fang, Xiao-Lin Zhao, "Design, fabrication and performance of a new vibration-based electromagnetic micro power generator", *Microelectronics Journal*, Volume 38, no. 12, pp. 1175-1180, 2007.

[9] M. A. E. Mahmoud, E. M. Abdel-Rahman, R. R. Mansour, and E. F. El-Saadany, "Springless Vibration Energy Harvesters", *ASME IDETC 2010*, Montreal, Canada, August 2010, DETC2010-29046.

[10] M. S. M. Soliman, E. M. Abdel-Rahman, E. F. El-Saadany, and R. R. Mansour, "A wideband vibration-based energy harvester", *Journal of Micromechanics and Microengineering* Volume 18, pp. 115021, 2008.

[11] Xu, Z.; Shan, X.; Chen, D.; Xie, T., "A Novel Tunable Multi-Frequency Hybrid Vibration Energy Harvester Using Piezoelectric and Electromagnetic Conversion Mechanisms", *Applied Sciences* Volume 6(1), 2016.

[12] Qiu, Jing ; Chen, Hengjia; Wen, Yumei; Li , Ping; "Magnetoelectric and electromagnetic composite vibration energy harvester for wireless sensor networks", *Journal of Applied Physics* Volume 117, pp. 17A331(1-4), 2015.

[13] I. Khodadad, L. Ball, R. Baghat, I. Shafieloo, E. M. Abdel-Rahman, E. F. El-Saadany, and R. R. Mansour, A. Hajian, "Optimization of a Micro Power Uni", *ASME IDETC 2011*, Washington, DC, September 2011, DECT2011-48687.

[14] M. Bendame, K. Elrayes, E. M. Abdel-Rahman, M. A. E. Mahmoud, R. R. Mansour, and E. F. El-Saadany, "Vertically-Aligned Springless Energy Harvester", *ASME IDETC 2011*, Washington, DC, September 2011, DECT2011-48371.

[15] M. Bendame, K. Elrayes, E. M. Abdel-Rahman, M. A. E. Mahmoud, R. R. Mansour, and E. F. El-Saadany, "Horizontally-Aligned Springless Energy Harvester", *International Conference on Applied Mathematics, Modeling Computational Science*, Waterloo, Canada, July 2011.

[16] R. Keith Mobley, *Root cause failure analysis*, Butterworth-Heinemann, Oxford, UK, 1999.

[17] M. Raju, *Energy Harvesting, ULP meets energy harvesting: A game-changing combination for design engineers*, white paper, Texas Instruments, November 2008.

[18] Bryan Steven Joyce, "Development of an Electromagnetic Energy Harvester for Monitoring Wind Turbine Blades", *Dissertation, Virginia Polytechnic Institute and State University, Blacksburg*, Virginia, December 2011.

[19] Greg Solberg, "The Magic of Tesla Roadster Regenerative Braking", `http://www.teslamotors.com/blog/magic-tesla-roadster-regenerative-braking` *Online, date accessed: October, 2013.*

[20] P. Patel, M.B. Khamesse, "Electromagnetic micro energy harvester for human locomotion", *Microsystem Technologies Journal*, Volume 19, no. 9-10, pp. 1357-1363, 2013.

[21] N. Lamberti, A. Iula, R. Carotenuto, G. Caliano and M. Pappalardo, "The Electromechanical Coupling Factor for Longitudinal and Transverse Propagation Modes", *REVISTA DE ACUSTICA*, Vol. XXXIII., pp. 8-13, 2002.

[22] E. Bouendeu, A. Greiner, P. J. Smith, and J. G. Korvink, "An efficient low cost electromagnetic vibration harvester", *Proceeding of PowerMEMS*, Washington, DC, December 2009, pp. 320-323.

[23] "Relation between Q-factor and bandwidth",
`http://www.sengpielaudio.com/calculator-bandwidth.htm`
Online, date accessed: August, 2015.

[24] C. Cepnik, O. Radler, S. Rosenbaum, T. Strohla, U. Wallrabe, "Effective optimization of electromagnetic energy harvesters through direct computation of the electromagnetic coupling", *Sensors and Actuators A: Physical Journal*, Volume 167, Issue 2, pp. 416-421, 2011.

[25] Piersol AG, Paez TL, and Harris CM, *Harris' Shock and Vibration Handbook. 6th ed.*, McGraw-Hill; 2010.

[26] A.H. Nayfah and D. T. Mook, *Nonlinear Oscillators*, John Wiley, 1979.

[27] Charles A. Holt, *Introduction to Electromagnetic Fields and Waves*, John Willy and Sons, 1967.

[28] B.P. Mann and N.D. Sims, "Energy harvesting from the nonlinear oscillations of magnetic levitation", *Journal of Sound and Vibration*, Volume 319, Issues 1-2, pp. 515-530, 2009.

[29] V. Challa, M. Prasad, Y. Shi and F. T Fisher, "A vibration energy harvesting device with bidirectional resonance frequency tunability," *Journal of Smart Materials and Structures*, vol. 17, 015035, 2008.

[30] Bowden, James A. and Burrow, Stephen G. and Cammarano, Andrea and Clare, Lindsay R. and Mitcheson, Paul D., "Switched-Mode Load Impedance Synthesis to Parametrically Tune Electromagnetic Vibration Energy Harvesters", *IEEE/ASME Transactions on Mechatronics*, Volume 20, no. 22, pp. 603-610, 2015.

[31] Bowden, James A. and Burrow, Stephen G. and Clare, Lindsay R., "Switched-mode impedance synthesis for electrical tuning of a vibration energy harvester", *Journal of Physics: Conference Series, The 13th International Conference on Micro and Nanotechnology for Power Generation and Energy Conversion Applications (PowerMEMS 2013)*, Volume 476, pp. 012082, London, UK, December 2013.

[32] K. El-Rayes, A. Abdel-Aziz, E.Abdel-Rahman, R. Mansour and E. El-Saadany, "Prototypes of a Field Disruption Energy Harvester", *ASME IDETC 2012*, Chicago, IL, USA, August 2012, DETC2012-71440.

[33] El-Rayes, K. (2011), "Low-Frequency Electromagnetic Energy Harvesting" (Master dissertation). Retrieved from UWSpace, University of Waterloo's institutional repository.

[34] K. El-Rayes, S. Gabran, E. Abdel-Rahman, and W. Melek, "Variable-Flux Biaxial Vibration Energy Harvester", *IEEE Sensors Journal*, volume 18, no. 8, pp. 3218-3227, 2018.

[35] El-Rayes, Karim; Gabran, Sala; Melek, William; "The Influence of the Load Type on the Center Frequency Tuning of the Variable-Flux Biaxial Energy Harvester", *Shock and Vibration*, volume 2023, Article ID 5795266, February, 2023.

[36] Shuo Cheng, Naigang Wang, and David P. Arnold, "Modeling of magnetic vibrational energy harvesters using equivalent circuit representations", *Journal of Micromechanics and Microengineering*, Volume 17, no. 11, pp. 2328-2335, 2007.

[37] Xiaobiao Shan, Zhenlong Xu, Rujun Song, and Tao Xie, "A New Mathematical Model for a Piezoelectric-Electromagnetic Hybrid Energy Harvester", *Ferroelectrics*, Volume 450, no. 1, pp. 57-65, 2013.

[38] S.G. Burrow, L.R. Clare, "A Resonant Generator with Non-Linear Compliance for Energy Harvesting in High Vibrational Environments", *IEEE International Electric Machines & Drives Conference IEMDC 2007*, Antalya, Turkey, May 2007, Vol. 1, pp. 715 - 720.

[39] "Ground vibrations"
http://en.wikipedia.org/wiki/Ground_vibrations
Online, date accessed: March, 2016

[40] J. Granlund, "Vehicle and driver vibrations", Vectura consulting AB, Sweden, June 2010.
Online, date accessed: March, 2016

[41] A. Godfrey, R. Conway, D. Meagher, G. OLaighin, "Direct measurement of human movement by accelerometry", *Medical Engineering & Physics* Volume 30, Issue 10, pp. 1364-1386, December 2008.

[42] P. Barralon, N. Noury, N. Vuillerme, "Classification of daily physical activities from a single kinematic sensor", *Proceedings of the IEEE Engineering in Medicine and Biology 27th Annual Conference* Shanghai, China, September 2005, pp. 2447-50.

[43] E. P. Furlani *Permanent Magnet and Electromechanical Devices: Materials, Analysis, and Applications*, Elsevier BV, 2001.

[44] Aktakka, E.E.; Najafi, K., "A Micro Inertial Energy Harvesting Platform With Self-Supplied Power Management Circuit for Autonomous Wireless Sensor Nodes", *IEEE Journal of Solid State Circuits*, vol.49, no.9, pp.2017-2029, September 2014.

[45] Halim, Miah A. and Park, Jae Y., "A non-resonant, frequency up-converted electromagnetic energy harvester from human-body-induced vibration for hand-held smart system applications", *Journal of Applied Physics*, 115, pp. 094901, March 2014.

[46] Kai Tao, Shuwei Liu, Sun Woh Lye, Jianmin Miao and Xiao Hu, "A three-dimensional electret-based micro power generator for low-level ambient vibrational energy harvesting", *Journal of Micromechanics and Microengineering*, vol.24, no.6, pp. 065022, May 2014.

[47] Mengdi Han, Zhongliang Li, Xuming Sun, Haixia Zhang, "Analysis of an in-plane electromagnetic energy harvester with integrated magnet array", *Sensors and Actuators A: Physical*, vol.219, pp. 38-46, November 2014.

[48] Y. Choi, S. Ju, S. H. Chae, S. Jun, S. M. Park, S. Lee, H. W. Lee and Chang-Hyeon Ji, "Low Frequency Vibration Energy Harvester Using Spherical Permanent Magnet with Non-uniform Mass Distribution", *Journal of Physics: Conference Series*, vol.476, no.1, pp. 012123, 2013.

[49] Ahmed Haroun, Ichiro Yamada and Shin'ichi Warisawa, "Micro electromagnetic vibration energy harvester based on free/impact motion for low frequency-large amplitude operation", *Sensors and Actuators A: Physical*, vol.224, , pp.87-98, April 2015.

[50] Han, Dongjae and Yun, Kwang-Seok, "Piezoelectric energy harvester using mechanical frequency up conversion for operation at low-level accelerations and low-frequency vibration", *Microsystem Technologies*, vol.21, no.8, pp.1669-1676, July 2014.

[51] Kai Tao, Jianmin Miao, Sun Woh Lye and Xiao Hu, "Sandwich-structured two-dimensional MEMS electret power generator for low-level ambient vibrational energy harvesting", *Sensors and Actuators A: Physical*, vol.228, pp.95-103, June 2015.

[52] Mitcheson, P.D.; Green, T.C.; Yeatman, E.M.; Holmes, A.S., "Architectures for vibration-driven micropower generators", *Journal of Microelectromechanical Systems*, vol.13, no.3, pp.429-440, June 2004.

[53] Vinod R. Challa, M. G. Prasad and Frank T. Fisher, "A coupled piezoelectric-electromagnetic energy harvesting technique for achieving increased power output through damping matching", *Journal of Smart Materials and Structures*, vol.18, no.9, pp.095029, August 2009.

[54] Dallago, E.; Marchesi, M.; Venchi, G., "Analytical Model of a Vibrating Electromagnetic Harvester Considering Nonlinear Effects", *IEEE Transactions on Power Electronics*, vol.25, no.8, pp.1989-1997, August 2010.

[55] Minami, Y.; Nakamachi, E., "Development of enhanced piezoelectric energy harvester induced by human motion", *Annual International Conference of the IEEE in Engineering, Medicine and Biology Society (EMBC), 2012*, San Diego, CA, USA, August 28-September 1, 2012, vol., no., pp.1627-1630.

[56] Xinping Cao; Chiang, Wen-Jen; Ya-Chin King; Yi-Kuen Lee, "Electromagnetic Energy Harvesting Circuit With Feedforward and Feedback DC-DC PWM Boost Converter for Vibration Power Generator System", *IEEE Transactions on Power Electronics*, vol.22, no.2, pp.679-685, March 2007.

[57] Anders Lei and Erik V. Thomsen, "Wideband Piezomagnetoelastic Vibration Energy Harvesting", *Journal of Physics: Conference Series*, Hyogo, Japan, vol.557, no.1, pp.012121, November 18-21, 2014.

[58] Mohammed F. Daqaq, Ravindra Masana, Alper Erturk, D. Dane Quinn, "On the Role of Nonlinearities in Vibratory Energy Harvesting: A Critical Review and Discussion", *Applied Mechanics Reviews*, vol.66, no.4, pp.040801.1-040801.21, May 2015.

[59] Steven A . Macintyre, *The Measurement, Instrumentation and Sensors Handbook*, CRC Press, 1999.

[60] Fondevilla, N.; Serre, C.; Perez-Rodriguez, A.; Acero, M.C.; Cabruja, E.; Campanella, H.; Esteve, J.,"Electromagnetic harvester device for scavenging ambient mechanical energy with slow, variable, and randomness nature", *International Conference on Power Engineering, Energy and Electrical Drives (POWERENG), 2011* , pp.1-5, 11-13 May, 2011.

[61] Scott D. Moss; Genevieve A. Hart; Stephen K. Burke; Steve C. Galea; Gregory P. Carman; "Vibration energy harvesting using a spherical permanent magnet", *Proc. SPIE 9057, Active and Passive Smart Structures and Integrated Systems 2014*, vol. 9057, pp. 90570S-12, April, 2014.

[62] Scott D. Moss; Genevieve A. Hart; Stephen K. Burke and Gregory P. Carman, "Hybrid rotary-translational vibration energy harvester using cycloidal motion as a mechanical amplifier", *Applied Physics Letters*, vol. 104, no. 3, pp. 033506.1-033506.5, December, 2014.

[63] Jing Qiu; Hengjia Chen; Yumei Wen and Ping Li, "Magnetoelectric and electromagnetic composite vibration energy harvester for wireless sensor networks", *Journal of Applied Physics*, vol. 117, no. 17, pp. 17A331.1-17A331.4 , December, 2014.

[64] Scott D. Moss, Joshua E. McLeod, Ian G. Powlesland, Steve C. Galea, "A bi-axial magnetoelectric vibration energy harvester", *Sensors and Actuators A: Physical*, vol. 175, pp. 165-168, March, 2012.

[65] L. Mateu and F. Moll, "Review of energy harvesting techniques and applications for micro-electronics", *Proc. SPIE 5837, VLSI Circuits and Systems II*, vol. 5837, pp. 5837-5837-15, Sevilla, Spain, June 2005.

[66] J. Joos and O. Paul, "Spherical magnetic energy harvester with three orthogonal coils," *2015 IEEE SENSORS, 2015*, pp. 1-4.

[67] Bendame, M. (2015), "Springless Electromagnetic Vibration Energy Harvesters" *Doctorate dissertation*, Retrieved from UWSpace, University of Waterloo's institutional repository.

[68] Yimin Fan, Mergen H. Ghayesh, Tien-Fu Lu, "Enhanced nonlinear energy harvesting using combined primary and parametric resonances: Experiments with theoretical verifications", *Energy Conversion and Management*, volume 221, issue 0196-8904, pp. 113061, 2020.

[69] Yimin Fan, Mergen H. Ghayesh, Tien-Fu Lu, "A broadband magnetically coupled bistable energy harvester via parametric excitation", *Energy Conversion and Management*, volume 244, issue 0196-8904, pp. 114505, 2021.

[70] Lee, Byung-Chul and Chung, Gwiy-Sang, "Design and Fabrication of Low Frequency Driven Energy Harvester Using Electromagnetic Conversion", *Transactions on Electrical and Electronic Materials*, vol. 14, no. 3, pp. 143-147, Jun. 2013.

[71] Fu, H.; Theodossiades, S.; Gunn, B.; Abdallah, I.; Chatzi, E., "Ultra-low frequency energy harvesting using bi-stability and rotary-translational motion in a magnet-tethered oscillator". *Nonlinear Dynamics*, vol.101, pp. 2131-2143, 2020.

[72] "Analogous Electrical and Mechanical Systems",
https://lpsa.swarthmore.edu/Analogs/ElectricalMechanicalAnalogs.html
Online, date accessed: July, 2019..

[73] A. Jassal and H. Polinder and J. A. Ferreira, "Literature survey of eddy-current loss analysis in rotating electrical machines", *IET Electric Power Applications*, vol. 6, no. 9, pp. 743-752, 2012.

[74] J.C. Dunn, "A Fuzzy Relative of the ISODATA Process and Its Use in Detecting Compact Well-Separated Clusters", *Journal of Cybernetics*, vol. 3, pp. 32-57, 1973.

[75] James C. Bezdek, *Pattern Recognition with Fuzzy Objective Function Algorithms*, Springer, 1981.

[76] James C. Bezdek, Robert Ehrlich and William Full, "FCM: The fuzzy c-means clustering algorithm", *Computers & Geosciences*, vol. 10, no. 2, pp. 191-203, 1984.

[77] E.H. Mamdani and S. Assilian, "An experiment in linguistic synthesis with a fuzzy logic controller", *International Journal of Man-Machine Studies*, vol. 7, no. 1, pp. 1-13, 1975.

[78] K. Michels, F. Klawonn, R. Kruse and A. Nürnberger, *Fuzzy Control: Fundamentals, Stability and Design of Fuzzy Controllers*, Springer-Verlag Berlin Heidelberg, 2006.

[79] "Magnetic Properties of Stainless Steels",
`http://www.cartech.com/techarticles.aspx?id=1476`
Online, date accessed: August, 2017.

[80] Neodymium block magnet type "BY0X08DCS",
`https://www.kjmagnetics.com/proddetail.asp?prod=BY0X08DCS`
Online, date accessed: April, 2023.

[81] Neodymium block magnet type "BY0X04DCS",
`https://www.kjmagnetics.com/proddetail.asp?prod=BY0X04DCS`
Online, date accessed: July, 2023.

[82] Neodymium block magnet type "BY084DCS",
`https://www.kjmagnetics.com/proddetail.asp?prod=BY084DCS`
Online, date accessed: July, 2023.

[83] "A Tutorial on Clustering Algorithms - Fuzzy C-Means Clustering"
`https://home.deib.polimi.it/matteucc/Clustering/tutorial_html/cmeans.html#bezdek`
Online, date accessed: January, 2018.

[84] S. Nissen. (2003), "Implementation of a Fast Artificial Neural NetworkLibrary (FANN)", Dept. Comput. Sci., Univ. Copenhagen, Denmark. [On-line]. Software Available:
`http://leenissen.dk/fann`
Online, date accessed: August, 2019.

[85] David L. Elliott, "A better Activation Function for Artificial Neural Networks", *ISR Technical Report TR 93-8*, 1993.

[86] M. Riedmiller and H. Braun, "A direct adaptive method for faster backpropagation learning: the RPROP algorithm", *IEEE International Conference on Neural Networks*, San Francisco, CA, USA, 1993, vol. 1, pp. 586-591.

[87] M. Magno, L. Cavigelli, P. Mayer, F. v. Hagen and L. Benini, "FANNCortexM: An Open Source Toolkit for Deployment of Multi-layer Neural Networks on ARM Cortex-M Family Microcontrollers : Performance Analysis with Stress Detection", *IEEE 5th World Forum on Internet of Things (WF-IoT)*, Limerick, Ireland, 2019, pp. 793-798.

[88] "TM4C1294 IoT enabled High performance 32-bit ARMÂ® CortexÂ®-M4F based MCU, device datasheet",
`https://www.ti.com/lit/gpn/tm4c1294ncpdt`
Online, date accessed: December, 2020.

[89] E BÃ¤umker and A Miguel Garcia and P Woias, "Minimizing power consumption of LoRa and LoRaWAN for low-power wireless sensor nodes", *Journal of Physics: Conference Series*, vol. 1407, no. 1, pp. 012092, November 2019.

[90] Moreno-Cruz, Fernando and Toral-Lopez, Victor and Escobar-Molero, Antonio and Ruiz, Victor U. and Rivadeneyra, Almudena and Morales, Diego P., "treNch: Ultra-Low Power Wireless Communication Protocol for IoT and Energy Harvesting", *Sensors*, vol. 20, no. 21, article no. 6156, October 2020.

[91] Christian Bach, "STM 300 THERMO OR BATTERY POWERED - Power Supply Alternatives to Solar Panel", 2020, Retrieved from EnOcean GmbH website:
`https://www.enocean.com/wp-content/uploads/application-notes/AN209_STM_`
`Thermo_or_Battery_Powered_Option_2020.pdf`,
Online, date accessed: August, 2022.

[92] "AN3147: Power management in STM8L and STM8AL", 2013, Retrieved from STMicroelectronics N.V. website:
`https://www.st.com/content/ccc/resource/technical/document/application_`
`note/a2/f6/c5/cf/e0/58/42/e5/CD00263631.pdf/files/CD00263631.pdf/jcr:`
`content/translations/en.CD00263631.pdf`, August 2013.
Online, date accessed: August, 2022.

[93] "TA0340 Technical Article STM32L Cortex-M3 microcontroller for usage in low-power healthcare applications", 2011, Retrieved from STMicroelectronics N.V. website:
`https://www.st.com/content/ccc/resource/technical/document/technical_`
`article/ad/e1/5a/79/66/6d/41/c7/CD00297944.pdf/files/CD00297944.pdf/jcr:`
`content/translations/en.CD00297944.pdf`. *Online, date accessed: August, 2022.*

[94] Mark Hofmann, "Technical Review: Practical Applications of Low-Power Design with nanoWatt XLP", Retrieved from Microchip Technology Inc. website:
`http://ww1.microchip.com/downloads/en/devicedoc/future%20xlp%20article.pdf`,
Online, date accessed: July 2022.

[95] "nanoWatt XLP eXtreme Low Power PICÂ® MCUs", Retrieved from Microchip Technology Inc. website:

`http://ww1.microchip.com/downloads/en/devicedoc/39941d.pdf`,
Online, date accessed: July, 2022.

[96] "PIC12F1822/16F182X 8/14/20-Pin 8-Bit Flash Microcontroller Product Datasheet", Retrieved from Microchip Technology Inc. website:
`https://ww1.microchip.com/downloads/aemDocuments/documents/OTH/`
`ProductDocuments/DataSheets/41406B.pdf`,
Online, date accessed: July, 2022.

[97] "Permanent Magnet Guidelines", Retrieved from Magnetic materials producers association website:
`https://www.automate.org/userAssets/a3/a3Uploads/pdf/`
`permanent-magnet-guideline.pdf`,
Online, date accessed: July, 2023.

[98] Gerhard Martinek, Sami Ruoho, Urs Wyss, "Magnetic Properties of Permanent Magnets & Measuring Techniques", Retrieved from Arnold Magnetic Technologies Inc. website:
`https://www.arnoldmagnetics.com/wp-content/uploads/2021/11/`
`White-Paper-Measurement-07.23.2021MS2a4.pdf`,
Online, date accessed: July, 2023.

Appendix A

Table 1: Magnetic restoring force coefficients versus center frequency

Cubical term	Quadratic Term	Linear Term	Constant	Center Frequency
-5.19	-23.05	14.28	2.928	7.8
-35	-23.05	14.28	2.928	7.35
-30	-23.05	14.28	2.928	7.45
-25	-23.05	14.28	2.928	7.55
-20	-23.05	14.28	2.928	7.6
-15	-23.05	14.28	2.928	7.65
-10	-23	14.28	2.928	7.75
-5	-23	14.28	2.928	7.8
0	-23	14.28	2.928	7.85
5	-23	14.28	2.928	7.95
10	-23	14.28	2.928	8
-5.19	-40	14.28	2.928	8.55
-5.19	-35	14.28	2.928	8.35
-5.19	-30	14.28	2.928	8.15
-5.19	-25	14.28	2.928	7.9
-5.19	-20	14.28	2.928	7.65
-5.19	-15	14.28	2.928	7.35
-5.19	-10	14.28	2.928	7.05
-5.19	-5	14.28	2.928	6.65
-5.19	0	14.28	2.928	6.25
-5.19	5	14.28	2.928	5.65
-5.19	10	14.28	2.928	4.8
-5.19	-23.05	0	2.928	6.55
-5.19	-23.05	5	2.928	6.8
-5.19	-23.05	10	2.928	7.3
-5.19	-23.05	20	2.928	8.55
-5.19	-23.05	25	2.928	9.2
-5.19	-23.05	30	2.928	9.85
-5.19	-23.05	35	2.928	10.5
-5.19	-23.05	40	2.928	11.1
-5.19	-23.05	45	2.928	11.7
-5.19	-23.05	50	2.928	12.25
-5.19	-23.05	55	2.928	12.75
-5.19	-23.05	60	2.928	13.3
-5.19	-23.05	65	2.928	13.8
-5.19	-23.05	14.28	0	6.4
-5.19	-23.05	14.28	6	8.65
-5.19	-23.05	14.28	9	9.25
-5.19	-23.05	14.28	12	9.6
-5.19	-23.05	14.28	15	10
-5.19	-23.05	14.28	18	10.4
-5.19	-23.05	14.28	21	10.65
-5.19	-23.05	14.28	24	10.85
-5.19	-23.05	14.28	27	11.05
-5.19	-23.05	14.28	30	11.2

Appendix B

Fuzzy C-Means Clustering Algorithm

Fuzzy C-Means (FCM), is a soft clustering algorithm where each data points can belong to more than cluster [74] [75] [76]. The relationship between a data point and associated cluster(s) is defined by the "degree of membership" (DoM) to each cluster based on the distance and connectivity to the center of the cluster. A DoM takes the value between 0 and 1, where 0 indicates that the data point doesn't relate to the cluster of interest and 1 is the highest grade of belonging to it. FCM can be used to infer fuzzy rules that defines the relationship between. The objective function of the Fuzzy C-Means is minimized to:

$$J_m = \sum_{i=1}^{N} \sum_{j=1}^{C} u_{ij}^m \parallel x_i - c_j \parallel^2, 1 \leq m < \infty \tag{1}$$

where m is a real number greater than 1, u_{ij} is the degree of membership of a data point x_i in cluster j, x_i is the ith of d-dimension data point, and c_j is the d-dimension center of cluster, and $\parallel x_i - c_j \parallel$ is the Euclidean distance between the ith data point and j^{th} cluster center [83]. Using iterative optimization of the objective function, for each step of the iteration, cluster centers vector is computed as:

$$c_j = \frac{\sum_{N}^{i=1} u_{ij}^m \cdot x_i}{\sum_{j=1}^{N} u_{ij}^m} \tag{2}$$

then update the membership function:

$$u_{ij} = \frac{1}{\sum_{k-1}^{C} \left(\frac{\parallel x_i - c_j \parallel}{\parallel x_i - c_k \parallel} \right)^{\frac{2}{m-1}}} \tag{3}$$

The objective function J_m is re-calculated from the updated clusters centers vector membership functions till minimum J_m is achieved.

Appendix C

Mamdani Fuzzy Inferencing

The Mamdani fuzzy inferencing method wa first developed by E.H. Mamdani in 1975 [77], it is based on fuzzification of antecedents and consequents by assigning a degree of membership between them, the degree of membership ranges between 0 and 1, then generate finite set of if-then rules between them, then compute the output for each rule, and finally aggregate all the outputs together to compute a crisp value for the output or "defuzzification" of the computed output value. The relation between the antecedents and consequents are expressed in terms of a value ranging between 0 and 1 of the antecedent (input) in the consequent (output) through a membership function. For multiple inputs system, the multiple membership functions expressing the relationships between antecedents and consequents are aggregated together to compute the output. There are different aggregation methods that are used for each type of fuzzy inference mechanisms. The Mamdani fuzzy inference system uses conjunctive relationship can be expressed by the operator "min()" or the boolean operator AND to compute the output for each rule, then all outputs are aggregated to compute the defuzzified output value. An example for Mamdani fuzzy inferencing for a two rule, two input-single output system is shown in figure 2 below. In
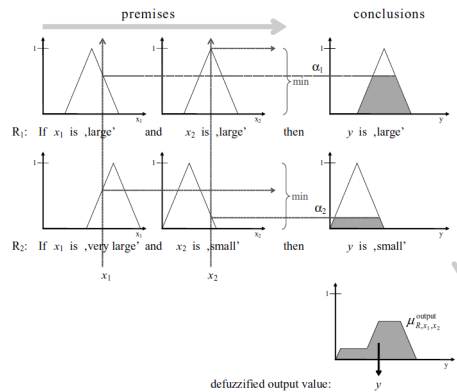

Figure 2: Example of a Mamdani computation scheme for 2-input, 1-output system [78]

this example, the inference system created two rules for inputs x_1 and x_2 and output y, for all rules, the minimum value is chosen, then outputs for each rule are aggregated and defuzzified to compute the output value using "Center of Area" method:

$$COA(\mu_{R,a_1,...a_n}^{output}) = \frac{\int_y \mu_{R,a_1,...a_n}^{output} \cdot y dy}{\int_y \mu_{R,a_1,...a_n}^{output} dy} \qquad (4)$$

where $\mu_{R,a_1,...a_n}^{output}$ is the degree of membership of input $a_1, a_2.....a_n$ in output y.

Fuzzy rules extracted from FCM engine

The Mamdani IF-THEN fuzzy rules extracted from 10 clusters FCM engine are:

1. If (Frequency is in1cluster1) then (Cubical is out1cluster1)(Quadratic is out2cluster1)(Linear is out3cluster1)(Constant is out4cluster1)

2. If (Frequency is in1cluster2) then (Cubical is out1cluster2)(Quadratic is out2cluster2)(Linear is out3cluster2)(Constant is out4cluster2)

3. If (Frequency is in1cluster3) then (Cubical is out1cluster3)(Quadratic is out2cluster3)(Linear is out3cluster3)(Constant is out4cluster3)

4. If (Frequency is in1cluster4) then (Cubical is out1cluster4)(Quadratic is out2cluster4)(Linear is out3cluster4)(Constant is out4cluster4)

5. If (Frequency is in1cluster5) then (Cubical is out1cluster5)(Quadratic is out2cluster5)(Linear is out3cluster5)(Constant is out4cluster5)

6. If (Frequency is in1cluster6) then (Cubical is out1cluster6)(Quadratic is out2cluster6)(Linear is out3cluster6)(Constant is out4cluster6)

7. If (Frequency is in1cluster7) then (Cubical is out1cluster7)(Quadratic is out2cluster7)(Linear is out3cluster7)(Constant is out4cluster7)

8. If (Frequency is in1cluster8) then (Cubical is out1cluster8)(Quadratic is out2cluster8)(Linear is out3cluster8)(Constant is out4cluster8)

9. If (Frequency is in1cluster9) then (Cubical is out1cluster9)(Quadratic is out2cluster9)(Linear is out3cluster9)(Constant is out4cluster9)

10. If (Frequency is in1cluster10) then (Cubical is out1cluster10)(Quadratic is out2cluster10)(Linear is out3cluster10)(Constant is out4cluster10)
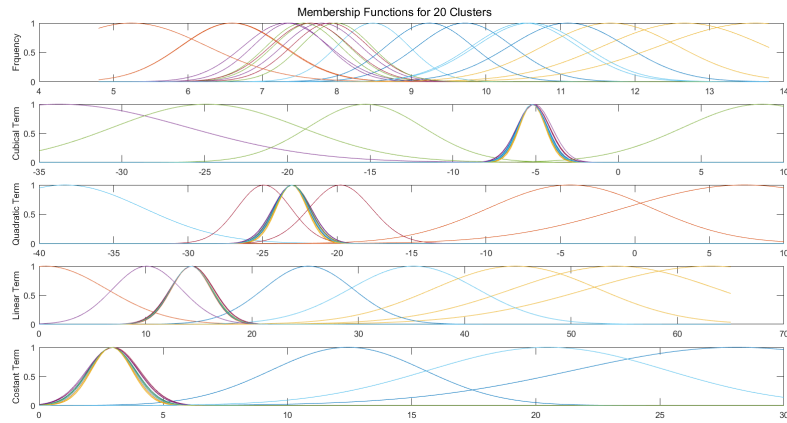
Figure 3: Membership functions for f_c and F_m coefficients generated from 20 clusters
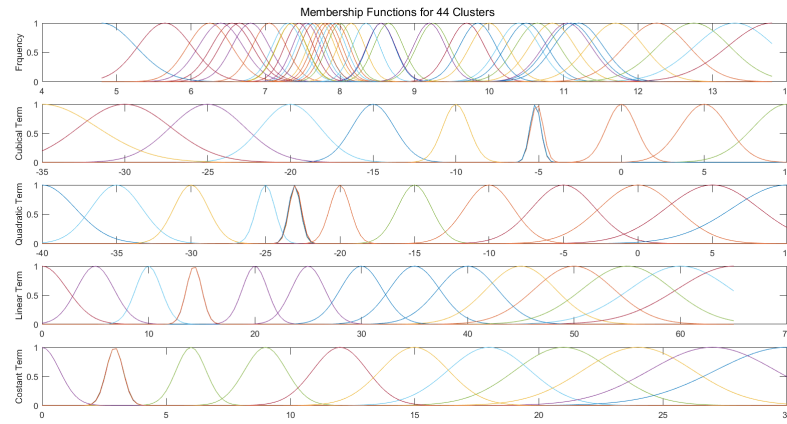

Figure 4: Membership functions for f_c and F_m coefficients generated from 44 clusters
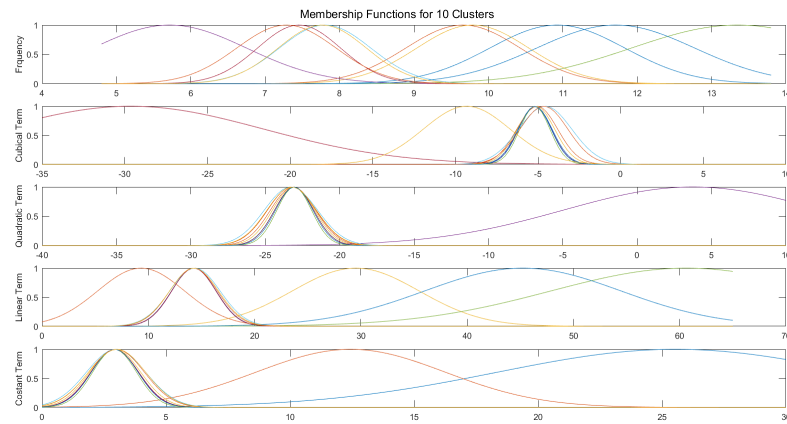

Figure 5: Membership functions for f_c and F_m coefficients generated from 10 clusters